UNIVERSIDAD CARLOS III DE MADRID

ESCUELA POLITÉCNICA SUPERIOR DE INGENIERÍA INDUSTRIAL

Departamento de Ingeniería Térmica y de Fluidos

Unidad Asociada de Ingeniería de Sistemas Energéticos UC3M-CSIC

DOCTORAL THESIS

Novel single–double-effect $LiBr/H_2O$ absorption prototype with a highly efficient direct air-cooled adiabatic absorber

Characterization, simulation and experimental results

Author: Arturo González Gil

Supervisor: Dr. Marcelo Izquierdo Millán

Leganés (Madrid), 2011

TESIS DOCTORAL

Nuevo prototipo de máquina frigorífica de absorción de LiBr/H_2O de simple y doble efecto con absorbedor adiabático refrigerado por aire de alta eficiencia

Descripción, simulación y resultados experimentales

Autor: Arturo González Gil

Director/es: Marcelo Izquierdo Millán

Firma del Tribunal Calificador:

Firma

Presidente: Dr. Francisco Javier Rey Martínez

Vocal: Dr. Robert Ghirlando

Vocal: Dr. José Daniel Marcos del Cano

Vocal: Dr. Néstor García Hernando

Secretario: Dra. Mercedes de Vega Blázquez

Calificación:

Leganés, 23 de Noviembre de 2011

To my family

To Alicia

"Live as if you were to die tomorrow. Learn as if you were to live forever"

(Mahatma Gandhi)

Abstract

Due to unsustainable growth of air conditioning market, a great interest in solar cooling technologies has emerged. The coincidence between availability of solar irradiation and peaks of cooling demand makes solar cooling a very attractive option to replace conventional refrigeration machines based on electricity. What is more, solar cooling systems normally use natural refrigerants that are not harmful to the environment. However, an improvement of the current technology is needed for solar cooling systems to compete with electricity-powered air conditioning systems.

In this work, a novel air-cooled single–double-effect $LiBr/H_2O$ absorption prototype is proposed as a solution to improve the viability of solar cooling systems. This prototype presents the following distinguishing features: firstly, it is directly air-cooled, which means that no cooling tower is needed; secondly, it is made up by compact heat exchangers, which allows for a reduced size of about 1 m^3; thirdly, it incorporates an adiabatic absorber operating with flat-fan solution sheets, which permits the working solution not to crystallize at high ambient temperatures; lastly, it can be powered by solar heat in its single-effect mode (4.5 kW), or by an alternative source such as fuel or waste heat in its double-effect stage (7 kW). In this way, 100% of the cooling demand may be supplied by a single absorption machine using solar energy as far as possible or, when it is not available, efficiently utilizing a fuel or even waste heat, for instance in a trigeneration system.

This thesis includes a detailed description of that single–double-effect absorption prototype as well as the fundamentals for its numerical simulation. Likewise, experimental results from a testing campaign carried out in Madrid during 2010 are presented and discussed. A solar facility with evacuated flat-plate collectors was used to test the single-effect operation mode of the prototype. In turn, the double-effect stage was fired by a

thermal oil facility with electrical resistances. As relevant results of the whole experimental campaign it is worth mentioning that the single-effect stage was able to work with COP values around 0.6, whereas the double-effect mode permitted to achieve values of about 1.0. The chilled water temperatures mostly ranged between 14°C and 16°C in single-effect operation mode, while they were around 12°C for the double-effect stage. Besides, it is highly noteworthy that after some 125 hours of operation under a wide range of conditions (outdoor temperatures up to 39.5°C), no solution crystallization was noticed.

On the other hand, this work includes an in-depth description of the absorber assembled in the single–double-effect prototype. Furthermore, a mathematical model is developed for simulation of air-cooled flat-fan sheets adiabatic absorbers. As far as we know, there is not any numerical modeling for this kind of absorbers in the literature. Based on that model, which was as well experimentally validated in this study, the capacity of the prototype absorber is optimized as a function of the energy consumption of its ancillary equipment (solution pump and fan).

Finally, the positive results derived from this work may be regarded as an important contribution to the development of air-cooled LiBr/H_2O absorption technology. Even though a few improvements in the prototype are still required, it seems that the proposed system represents a feasible alternative to overcome some of the major obstacles concerning solar air conditioning.

Resumen

La actual situación de insostenibilidad en el mercado de la climatización ha motivado un gran interés por la refrigeración solar como alternativa al uso de máquinas eléctricas. El hecho de que las horas de máxima radiación solar coincidan con los momentos de mayor demanda de frío en los edificios, hace que estos sistemas sean especialmente indicados para sustituir a los equipos convencionales de aire acondicionado. Además, hay que añadir que esta tecnología normalmente utiliza refrigerantes naturales que no son dañinos para el medio ambiente. Sin embargo, los sistemas actuales de refrigeración solar necesitan una mejora sustancial para poder competir directamente con los aparatos tradicionales de climatización.

Como una posible solución para mejorar la viabilidad de los sistemas de refrigeración solar, en este trabajo se presenta un nuevo prototipo de máquina de absorción de $LiBr/H_2O$ que integra los ciclos de simple y doble efecto en una misma unidad. Las principales características que hacen de este prototipo una novedad tecnológica son las siguientes: en primer lugar, se trata de una máquina directamente condensada por aire, eliminando así la necesidad de instalar torres de refrigeración; en segundo lugar, el prototipo está básicamente formado por intercambiadores de calor compactos, con lo que se alcanza un tamaño final de máquina muy reducido, aproximadamente 1 m^3; en tercer lugar, el prototipo incorpora un absorbedor adiabático con láminas planas que evita que la disolución cristalice a altas temperaturas ; por último, la máquina puede funcionar como una unidad de simple efecto (4.5 kW), alimentada en este caso por energía solar, o como una unidad de doble efecto (7 kW), quemando combustibles o utilizando calor residual. De este modo, se podría llegar cubrir el 100% de la demanda de refrigeración con una sola unidad que saca el máximo partido a la energía solar y, cuando ésta no es suficiente, utiliza eficiente-

mente combustibles o incluso el calor residual procedente de otros procesos, por ejemplo en una planta de trigeneración.

En esta tesis doctoral se incluye una descripción detallada del prototipo de simple y doble efecto así como los fundamentos teóricos para su simulación numérica. Asimismo, se presentan y discuten los resultados experimentales obtenidos durante una campaña de ensayos llevada a cabo en Madrid durante el año 2010. Para probar el funcionamiento del prototipo como máquina de absorción de simple efecto se ha utilizado una instalación solar con colectores planos de vacío. En cambio, para ensayar el prototipo como máquina de doble efecto se ha utilizado un aceite térmico como fuente de energía. Como resultados destacados de la campaña de experimentación cabe mencionar que los valores del COP se movieron entorno a 0.6 en simple efecto y alrededor de 1.0 en doble efecto. A su vez, se alcanzaron temperaturas de agua fría entre 14°C y 16°C para el simple efecto y de aproximadamente 12°C para el doble efecto. Además, es de gran relevancia el hecho de que, después de unas 125 horas de funcionamiento bajo condiciones de trabajo muy diferentes (hasta 39.5°C de temperatura exterior), la disolución de $LiBr/H_2O$ no se haya cristalizado en ningún momento.

Por otra parte, este trabajo incluye una descripción detallada del absorbedor instalado en el prototipo. Asimismo, se ha desarrollado un modelo matemático para simular absorbedores adiabáticos de láminas directamente refrigerados por aire. Por lo que sabemos, hasta el momento no se ha publicado ninguna modelización numérica para este tipo de absorbedores. Tomando como referencia el modelo propuesto, que también ha sido validado experimentalmente en este estudio, se ha realizado una optimización de la capacidad del absorbedor del prototipo en función del consumo energético de sus equipos auxiliares (bomba de disolución y ventilador).

Por último, los buenos resultados obtenidos con este prototipo nos hacen pensar que este trabajo representa una contribución importante al desarrollo de las máquinas de absorción de $LiBr/H_2O$ refrigeradas por aire. A pesar de que el prototipo todavía no está totalmente optimizado, con él se ha demostrado que la tecnología propuesta en esta tesis doctoral constituye una alternativa viable para superar algunos de los principales problemas relacionados con la refrigeración solar.

Agradecimientos/Acknowledgements

Al finalizar un trabajo como éste, me doy cuenta que el esfuerzo realizado durante los últimos cuatro años habría sido inútil sin el imprescindible apoyo institucional y la ayuda de muchas personas que han estado a mi lado durante todo este tiempo.

En primer lugar, tengo que agradecer al Consejo Superior de Investigaciones Científicas el haber financiado mis estudios de doctorado con la concesión de una beca JAE-Predoc. Del mismo modo agradezco a la Universidad de Vigo y a la Universidad Carlos III de Madrid el haberme aceptado en sus programas de doctorado. Asimismo, agradezco al Ministerio de Ciencia e Innovación el apoyo económico a los proyectos en los que se engloba la realización de esta tesis doctoral. Especialmente doy gracias a la Unidad Asociada de Sistemas Energéticos CSIC-UC3M por su apoyo en la realización de este trabajo.

En particular, quiero agradecer al Instituto de Ciencias de la Construcción Eduardo Torroja (IETcc) toda la ayuda que me ha ofrecido tanto en lo personal como en lo profesional, siendo como mi segunda casa desde que he llegado a Madrid.

Mi más sincero y profundo agradecimiento para mi director de tesis, Marcelo Izquierdo, por su incansable y entusiástica dedicación a este trabajo de investigación. Sus palabras de motivación y esperanza, además de la gran confianza que siempre ha tenido en mí, han convertido los momentos más complicados en verdaderas lecciones de superación personal. Indudablemente, su apoyo y dirección han sido clave en la realización de esta tesis doctoral.

Mil gracias a Emilio Martín, gran apasionado y conocedor de las máquinas de absorción y de todo lo que tiene que ver con el trabajo experimental. Sin duda, un excelente profesional y una extraordinaria persona con la que he compartido momentos inolvidables,

tanto en el laboratorio como en las pistas de tenis. Ni el prototipo ni yo mismo hubiésemos funcionado de la misma forma sin la ayuda de Emilio.

También quiero expresar mi agradecimiento a mis compañeros en el grupo de investigación "Ahorro de Energía y Reducción de Emisiones en Edificios", quienes con su enorme valía han ayudado a que este y otros muchos trabajos hayan salido adelante. Gracias Esther, Raquel, David, Amancio y Dani por vuestro compañerismo.

Por supuesto, no puedo olvidarme de mis compañeros y amigos del IETcc, con los que he vivido experiencias verdaderamente inolvidables durante estos cuatro años. Son muchas las personas a las que debo agradecer su afecto, simpatía y sobre todo su amistad, pero entre ellas destaco a Cris, Vane, Virtu, Belén, Alberto, Alfredo y Yago, porque desde el principio me han hecho sentir como en casa.

A mis padres y a mi hermana Lorena les estaré eternamente agradecido por haberme apoyado en todas las decisiones que he tomado. Su cariño y comprensión han sido fundamentales para que esta última "aventura" en la que me he embarcado haya llegado a buen puerto.

A Alicia le agradezco profundamente la paciencia, el apoyo y el cariño que me ha mostrado desde siempre, pero sobre todo durante estos cuatro años en Madrid. Muchísimas gracias por estar a mi lado y por transmitirme cada día tu energía positiva.

Finally, I am very grateful to Prof. J.R. Thome for inviting me to stay at the Heat and Mass Transfer Laboratory (LTCM) for three fantastic months. Furthermore, I would like to thank my colleagues at LTCM for making my short stay in the École Polytechnique Fédéral de Lausanne so pleasant. Special thanks to Marcel Christians, Eugene Van Rooney and Sylwia Szczukiewicz for their support and friendliness.

Contents

List of Figures

List of Tables

Nomenclature

Roman symbols

A	area, m^2
COP	coefficient of performance
c_p	isobaric specific heat, kJ/kgK
C	heat capacity rate, W/K
C_r	heat capacities ratio
D	diameter, m
DE	double-effect
E	energy, kWh
F	approach to equilibrium factor
f	friction factor
G	mass velocity, kg/sm^2
g	gravitational acceleration, m^2/s
GWP	global warming potential
FR	flow ratio
HG	high-pressure generator
h	specific enthalpy, kJ/kg / heat transfer coefficient, W/m^2K
$\overline{h_m}$	mean mass transfer coefficient, m/s
I	incident solar intensity, kW/m^2

ITH integrated temporal horizon

K resistance coefficient of pipe elbows and valves

k conductivity, W/mK

L length, m

Le Lewis number

LG low-pressure generator

$\dot{m}$ mass flow rate, kg/s

NTU number of transfer units

n number

Nu Nusselt number

P pressure, kPa

PER primary energy ratio

PHE plate heat exchanger

Pr Prandtl number

Q heat transfer rate, kW

q specific heat transfer rate, kW/kg_r

R solar radiation, kW

r radial coordinate in the solution sheet, m

Re Reynolds number

RTD resistance temperature detector

RSP recirculation solution pump

R_w wall heat transfer resistance, K/W

SCR solar cooling ratio

SE single-effect

SF solar fraction

SHX solution heat exchanger

SP solution pump

T temperature, °C

t time, s

U global heat transfer coefficient, W/m²K

u velocity, m/s

v specific volume, m³/kg

W power consumption, kW

w specific work, kW/kg$_r$

X concentration of LiBr in the solution (%)

$\hat{X}$ normalized mass fraction

z transversal coordinate in the solution sheet, m

Greek symbols

α thermal diffusivity of the solution, m²/s

ΔP pressure drop, Pa

ΔT_{sub} initial subcooling of the solution sheet flow, °C

ΔX increment in the solution mass fraction, %

ΔX_{lm} logarithmic mean mass fraction difference

δ_3 normalized subcooling

ε effectiveness / thickness of the solution sheet, m

η efficiency

$\hat{\eta}$ normalized transversal coordinate in the solution sheet

μ dynamic viscosity, Pa·s

ν kinematic viscosity, m²/s

$\hat{\xi}$ normalized radial coordinate in the solution sheet

ρ density

θ aperture angle of the sheet, degree

σ ratio of areas in a finned-tube heat exchanger

Subscripts

a absorber

abs absorption

ac air-cooler of the absorber

air air flow

amb ambient conditions

aux ancillary equipment

b bulk conditions

bank bank of sprayers in the absorber

ca cooling air

c solar collectors field

cond condensation/condenser

d daily

e evaporator/evaporation

el electricity/electrical

eq equilibrium conditions

exp experimental

f final position in a flat-fan sheet

fan fan of the prototype

ff free flow

fr frontal

g single-effect generator

HG high-pressure generator

Hshx high-temperature solution heat exchanger

i inlet/initial position in a flat-fan sheet/inner

in	indoor
l	heat loss
LG	low-pressure generator
Lshx	low-temperature solution heat exchanger
max	maximum
min	minimum
o	outlet/outer
oil	thermal oil
out	air surrounding the prototype
p	solution pump
pipes	pipes of the solution-air heat exchanger
pred	predicted
r	refrigerant
room	refrigerated space
rsp	recirculation solution pump
s	solution
seas	seasonal
sec	secondary circuit
sheet	solution flat-fan sheet in the bank of sprayers
shx	solution heat exchanger
sub	sub-cooler
t	water storage tank
th	thermal
v	vapor
w	water
∞	complete adiabatic saturation

Chapter 1

Introduction

1.1 Motivation of the study

Air conditioning represents a relatively new and rapidly expanding market which involves both residential and service sectors. Cooling demand has been steadily increasing in many parts of the world, especially in developed countries with moderate climates, such as most of the EU countries. The higher standard of leaving and the associated increase in the comfort requirements seem to be the main causes of this growth. In addition, the tendency to design more glazed buildings, the greater equipment of the offices and the climatic change may trigger even higher growths in the cooling demand.

A recent study on the European cooling market shows that only 5% of $20.9 \cdot 10^9$ m^2 corresponding to residential space in Europe was air conditioned at the turn of the 21st century, (ECOHEATCOOL, 2007). Likewise, in the service buildings, which has a total floor area of $7.0 \cdot 10^9$ m^2, the rate was around 27%. If taking into account that in the United States and Japan the corresponding rates were between 70 and 100% and that sales of new air conditioners have been increasing at approximately 14% for the last years, (BSRIA, 2005), a fast and strong market expansion is forecasted for the next years in Europe. According to (ECOHEATCOOL, 2007), by the end of 2012 a saturation rate of 60% will be reached for the service sector, while for the residential sector it will be of 40%.

This would mean a fourfold increase in the cooling demand from 2000 and would correspond to 660 TWh of cooling demand in EU-32.

Although the growth of cooling demand has been particularly strong in south Europe (note that, in Spain, the residential air conditioning penetration is today around 30%), a study of the Japan Refrigeration and Air conditiong Industry Association (JRAIA) confirms that this is a world-wide tendency. Actually, in a survey estimating the demand for air conditioners in the world (IIR, 2003), they assessed that the demand for 2002 was about 44.6 million units, whereas for 2006 it was of 52.3 million units.

Regarding the type of cooling equipment, currently residential and service buildings are mostly air conditioned by electrically powered vapor compression machines. Among them, low capacity packaged units are being more and more demanded as compared to large air conditioning systems based on chillers, (ECOHEATCOOL, 2007). Easiness of installation and comparatively reduced costs make low-power air conditioners be widely used, especially those air-cooled.

The strong expansion of the cooling market is therefore associated to an important rise in electricity demand, being the peaks reached on hot summer days notably dangerous for the stability of electricity grids, (Izquierdo et al., 2011a). Likewise, the increasing cooling demand threatens the international agreements on CO_2 emission reduction, since consumption of fossil sources may be increased in order to meet the electricity demand. Moreover, it is necessary to add that the refrigerants commonly used in air conditioning systems present a very high global warming potential (GWP). For instance, in case of the refrigerant R410A, GWP is 3400 times greater than estimated for CO_2 over a 20 year Integrated Temporal Horizon (ITH), and 1300 times greater over a 100 year ITH. Even though some regulations have been approved to restrict the use of fluorinated greenhouse gases, *"F-Gas" Regulation 842/2006*, unavoidable leakages still represents a serious problem for the environment.

The unsustainable situation of air conditioning market has triggered a great interest in solar cooling technologies. The fact that high values of solar irradiation generally concur with peaks of cooling demand makes solar cooling an appealing alternative to replace conventional refrigeration machines based on electricity. In addition, solar cooling systems normally use natural refrigerants, which are not harmful to the environment. Conse-

quently, solar cooling could be considered as a suitable option to cut down electricity consumption, to reduce dependence on fossil sources and to save greenhouse gas emissions.

Several research and demonstration projects about different solar refrigeration options have been carried out for the last years, as shown by (Balaras et al., 2007), (Henning, 2007) or (Fong et al., 2010). From these works, it can be extracted that, among the different technologies available for refrigeration in buildings, solar absorption cooling is one of the most attractive options to replace conventional electrically driven chillers. Specifically, single-effect absorption chillers using $LiBr/H_2O$ appear to be the most interesting machines for use in solar cooling because of their simplicity and their relatively low driving temperature. However, this kind of chillers has traditionally been water-cooled machines, which implies the use of wet cooling towers. This fact makes absorption systems not only more expensive, but also less environmentally friendly because of the high water consumption, which is usually a scant source in areas with high cooling demand, such as South Europe or the Mediterranean region. Moreover, cooling towers are associated with growths of bacteria that may cause various diseases such as *Legionella*.

Taking account of the above mentioned reasons, the development of air-cooled absorption chillers may be looked as a very appropriate alternative for air conditioning in buildings, especially in low capacity applications. This is a point also observed in other publications like (Kim & Infante-Ferreira, 2008b) or (IEA, 2007), where the development of air-cooled machines was proposed as an important subject in the future R&D. However, this technology presents a major drawback, the relatively high risk of solution crystallization, due to the high working temperatures (Izquierdo et al., 2004). In order to overcome this difficulty, a few studies have been performed for the last years. Notwithstanding, in spite of the great effort put into, no air-cooled absorption machines are currently available on the market.

On the other hand, solar systems are not generally designed to meet 100% of seasonal heating or cooling demand because of the intermittency of solar energy, the lack of space, the elevated installation costs, etc. In general, the solar fraction for refrigeration is about 2/3 of seasonal demand, as experimentally found by (González-Gil et al., 2011) for the case of Madrid. Accordingly, an additional system has to be installed in order to supply the remaining third part of the cooling demand. Traditionally, there have been two possible options to face that issue: firstly, installing a conventional vapour compression air conditioning system and, secondly, setting up an external boiler feeding the generator of

the absorption machine. The first alternative is not economically viable, since it implies duplication of cooling systems. In turn, the second choice might result economically interesting only if the same boiler could be used to supply the heating demand in winter. Anyhow, none of those options can be regarded as efficient solutions from an energetic point of view. In the first case, electricity is used as power source and, in the second alternative, a fuel is burned to produce cool with efficiencies around 0.5, if the chiller in the system is an absorption machine. In case of using other solar cooling technologies such as adsorption of desiccant systems, the refrigeration efficiency would be even lower.

The above exposed problem is regarded as one of the major difficulties for the solar refrigeration to compete with conventional vapour compression machines. However, there are some additional troubles that solar cooling technology has to overcome in order to make headway on the domestic air conditioning market, as pointed out by (ESTIF, 2006). Primarily, the lack of package-solutions for residential and small commercial applications. Moreover, the usual need for wet cooling tower increase the size of these systems and, what is more, may trigger *Legionella* contamination. Additionally, the lack of standardized products causes greater initial investment costs in refrigeration machines compared with conventional cooling systems. Lastly, costs associated with solar facilities installation are often very high. Nonetheless, capital cost per unit could be reduced when solar thermal collectors are used for heating applications during winter, as suggested by (Marcos et al., 2011b).

In view of the reasons given above, one can conclude that development of compact air-cooled LiBr/H_2O absorption chillers for low power applications appears as an interesting and promising research line. Specially challenging is the objective of finding out a solution that enables solar cooling systems to be competitive with conventional electricity-powered air conditioners. However, two major difficulties must be overcome to reach this target: avoiding crystallization of LiBr/H_2O solution and designing highly efficient systems able to supply 100% of cooling demand.

1.2 Objectives of the study

The primary objectives of this study are the testing and characterization of a new LiBr/H_2O absorption prototype which has been developed by the *Energy Saving and Emissions Reduction in Buildings* research group, sponsored by the Eduardo Torroja Institute for Construction Science (CSIC). As distinctive characteristics, it is worth mentioning that

this prototype is directly air-cooled, which implies that no cooling tower is needed. Besides, it incorporates compact heat exchanger allowing for a reduced size of the machine. Moreover, it includes an adiabatic absorber working with flat-fan solution sheets, which avoids the crystallization of the working solution at high ambient temperatures. Lastly, it consists of an integrated single–double-effect chiller, which means that it may work as a single-effect unit (4.5 kW) or as a double-effect one (7 kW). Thus, 100% of the cooling demand may be provided by a single absorption machine using solar energy (single-effect) or, when it is not available, a fossil or renewable source in a highly efficient way (double-effect).

Moreover, characterization, modelization and optimization of the air-cooled adiabatic absorber with flat-fan sheets are specific objectives of this thesis.

Finally, the work described in the present study aims at contributing to the development of absorption technology and, by extension to the improvement of solar cooling systems. The final objet of the group's research line is the substitution of conventional electricity-powered air conditioners by more environmental friendly systems.

1.3 Outline of the thesis

Description of the research work that has been carried out in this thesis is presented in the following chapters:

In *Chapter 2*, the current state-of-the art on absorption technologies is discussed. The review is mainly focused on the air-cooled LiBr/H_2O systems.

Chapter 3 describes the new single–double-effect absorption prototype presented in this study. Principles of working and details of its components are given. Besides, the chapter includes a description of the facilities used to test the prototype.

Chapter 4 presents a numerical model to predict the main working parameters of the single–double-effect prototype in both operation modes: single- and double-effect.

In *Chapter* 5, the absorber of the prototype is in-depth described. Additionally, a mathematical model is developed to perform simulations of the absorber behavior under different working conditions. Besides, an optimization of the absorber design is done in this chapter.

In *Chapter 6*, the main results of an experimental campaign carried out to test the single-effect stage of the prototype are shown and discussed. A comparison between experimental and predicted results is as well presented.

Chapter 7 presents and discusses the experimental results corresponding to the double-effect operation mode of the prototype. Likewise, these results are compared with predictions given by the simulation model.

Chapter 8 includes the experimental validation of the absorber model presented in Chapter 5.

In *Chapter 9,* the major findings of this study are summarized. Moreover, topics for further research are proposed.

Chapter 2

State-of-the-art review on absorption technologies

2.1 Introduction

In this chapter, the current state-of-the art on absorption technologies will be reviewed. First, a brief summary the different absorption technologies will be given, paying special attention to the most widely used configurations: single- and double-effect cycles. Then, the commercially available absorption units for small scale air conditioning applications will be listed and analyzed. Finally, on the grounds of the actual state-of-the-art, development of air-cooled single–double-effect absorption machines will be justified.

2.2 Review of available absorption technologies

Essentially, absorption is a refrigeration technology which enables to produce cold by directly using thermal energy. It is based on the phenomena of sorption, which is a collective term for the process where one substance (sorbent) takes up or holds another (sorbate) owing to physical or chemical attraction between the pair of substances. The sorbate plays the role of refrigerant, describing the same thermodynamic cycles as in a vapor compression system. In fact, sorption systems are analogous to conventional refrigeration ones, but using thermal compression instead of mechanical compression.

Thermal compression of the refrigerant basically involves two reverse processes: *desorption*, which consists of separating the sorbate from the sorbent by adding heat; and *sorption*, where the sorbate is soaked up by the sorbent. Contrary to desorption process, sorption is an exothermic reaction.

Sorption systems can be classified into three major groups, depending on the nature of the sorbent and on whether the process occurs in an open or in a closed environment:

- *Absorption*: the liquid or solid sorbent experiences physical and/or chemical changes during the soaking up of the refrigerant.
- *Adsorption*: a solid sorbent attracts the refrigerant onto its surface but it does not change as a result of the process.
- *Desiccation:* the sorbent (solid or liquid) is a hygroscopic material which absorbs the moisture from humid air. It is referred as an open cycle since the refrigerant (water) is discarded from the system after providing the cooling effect.

When air conditioning applications are concerned, it is commonly agreed that absorption technology is the most suitable option among sorption cooling processes, (Fan et al., 2007). Desiccant cooling systems may be an adequate solution when having a good indoor quality is essential. Moreover, their application is limited to large installations because of the high initial cost, as stated by (Kim & Infante-Ferreira, 2008b). On the other hand, adsorption systems present a maximum achievable COP comparable with absorption ones. Yet, their lower densities make them bulkier and more expensive. Nevertheless, they may be a good option when low temperature driving heat is available.

Regarding the working pairs for absorption refrigeration systems, $LiBr/H_2O$ and H_2O/NH_3 are the most widely used. The absorbent is the first term in the formulae whereas the absorbate is the second term. Although other innovative working pairs have been investigated for the last years, see for instance (Schneider et al., 2011), it seems that those two classical pairs will be still the reference for absorption systems in the near future, as predicted by (Ziegler, 2002). Needless to say that each working pair has its advantages and drawbacks, as shown in Table 2.1. By and large, $LiBr/H_2O$ is most adequate for air conditioning purposes, while H_2O/NH_3 is more suitable for refrigeration in industrial applications.

Table 2.1 Comparison between H_2O/NH_3 and $LiBr/H_2O$ as working pairs for absorption systems

Working pair	Advantages	Disadvantages
H_2O/NH_3	Evaporative below 0°C	Toxic
	Inexpensive	High working pressure
		Need for rectification
$LiBr/H_2O$	High COP	Corrosiveness
	Low operation pressures	Vacuum is needed
	Nontoxic	Risk of crystallization
	Large latent heat of vaporization	Not valid for chilling below 0°C

In absorption machines, the condensation and the absorption heats are traditionally removed by means of water or the surrounding air. In case of water-cooled machines, a cooling tower is needed, which increases the initial and operation costs of the system. Besides, cooling towers are related to growth of bacteria causing serious diseases, such as *Legionella*. Another disadvantage of water cooling systems is the associated water consumption, which according to (SACE, 2003) is between 2 kg and 5 kg per kWh of cooling. Note that this represents a significant waste, since by evaporating only 1.4 kg of water an equivalent cooling effect may be provided.

Those drawbacks make water-cooled systems inadequate for small scale cooling applications, especially in regions where water is a scant source. In turn, air-cooled absorption machines are very suitable for that kind of applications. However, they are not able to operate as efficiently as water-cooled systems because of the higher working temperatures in the condenser and the absorber. Besides, the driving temperatures for air-cooled machines are higher than for water-cooled, which is regarded as a clear disadvantage when solar cooling is concerned, (Kim, 2007).

On the other hand, depending upon the temperature level of the driving heat, different cycle configurations are available for absorption machines. As a general rule, it can be said that multi-effect cycles have higher COP but at the expense of higher driving heat temperatures, (Gebreslassie et al., 2010). Below, a brief description of the most usual absorption cycles is given.

The simplest configuration is the **single-effect** cycle. It is a common fact that the coefficient of performance (COP) of $LiBr/H_2O$ machines working with this cycle ranges from

0.6 to 0.8. Besides, driving temperatures are between 80 and 100°C for water-cooled systems, while for air-cooled ones are about 20°C higher. This range of temperatures makes $LiBr/H_2O$ single-effect cycles very appropriate for solar cooling.

By adding some extra components to the basic single-effect configuration, the **double-effect** cycle is able to use the input heat twice for generating a greater amount of refrigerant. Due to the higher working pressures achieved in this configuration, this cycle is not practical for refrigerants with low boiling temperatures such as ammonia. The COP obtained for $LiBr/H_2O$ double-effect systems is typically between 1.1 and 1.3. In turn, the usual range of driving temperatures is 140-170°C for water-cooled machines and 160-190°C for air-cooled ones, (Izquierdo et al., 2002). Those temperatures make more complicated the use of solar energy as driving source; however several technologies are available in the market to provide solar heat at such temperatures, (Mendes, 2007).

As an extension of the previous configuration, the **triple-effect** cycle appears as a promising option to increase the performance of $LiBr/H_2O$ absorption machines. Here, the input heat is used in three stages and driving temperatures above 200°C are needed. In general, COP values around 1.4-1.6 may be achieved. However, there is a major challenge associated with this cycle, the corrosion problems caused by the very high working temperatures. Triple-effect technology is currently under active development, as pointed out by (Kim et al., 2002), (Kaita, 2002) or (Wang et al., 2010).

When the temperature of the available source heat is not high enough to fire a single-effect configuration, the **half-effect** cycle is regarded as an adequate option. The driving temperatures for water-cooled $LiBr/H_2O$ systems are typically between 60 and 75°C. In turn, air-cooled systems require driving temperatures of about 20-30°C higher. In general, COP values achieved with this cycle are roughly half of a single-effect cycle, hence its name. Although this configuration can be also referred as *two-stage* cycle, the former name is usually preferred. The main disadvantages of this cycle are the complicated configuration and the reduced COP, around 0.3-0.4. Some interesting works studying the possibilities of this cycle are, for instance, (Sumathy et al., 2002), (Izquierdo et al., 2004), (Izquierdo et al., 2005) and (Kim & Infante-Ferreira, 2009).

In case the temperature of the heat source is too low for the double-effect cycle and too high for the single-effect cycle, the **one and a half-effect (1.5-effect)** cycle may be a good choice, according to (Wang & Zheng, 2009). Basically, this configuration results from

the combination of single- and half-effect cycles, which leads to complicated schemes. For driving temperatures ranging between 110°C and 140°C, the expected COP is about 1.0.

Lastly, it is interesting to mention the **GAX** cycle, which according to (Herold et al., 1996) is a very elegant way of achieving higher effect performance with a cycle configuration that essentially appears to be a single-effect configuration. It includes a generator-absorber heat exchanger that allows using the waste energy from the absorber as a part of the needed energy in the generator. Consequently, an extra production of refrigerant is obtained and higher COP values are possible. Since this cycle requires a working fluid that is stable in a wide range of temperatures, aqueous ammonia solution is typically used. (Yari et al., 2011) is one of the most recent works concerning this cycle in the literature.

2.2.1 Description of the air-cooled $LiBr/H_2O$ single-effect cycle

As shown by Figure 2.1, a single-effect absorption chiller basically consists of four components that exchange energy with the surroundings, namely: condenser, generator (also known as desorber), evaporator and absorber. Additionally, it presents an internal heat exchanger for the $LiBr/H_2O$ solution, two throttle or expansion valves and a solution pump. The schematic given below is drawn as if it were superimposed on a *Dühring* chart of $LiBr/H_2O$ solution. Hence, the position of each component indicates the relative temperature, pressure and mass fraction of the working solution.

Solution loop

The $LiBr/H_2O$ solution circulates between the absorber and the generator thanks to a pump, which besides raises the solution pressure. In the generator, heat is supplied by external means such as a combustion source or any fluid with a sufficiently high temperature. As a result, the water, which is the most volatile component in the mixture, is separated from the solution as vapor. Then, the generated vapor (refrigerant) flows to the condenser and the remaining liquid solution leaves the desorber flowing back to the absorber.

As the vapor separated from the solution is essentially free of LiBr salt, the solution becomes more concentrated at the exit of the desorber than at the inlet. This strong solution enters the absorber after having reduced its pressure in the throttling valve. In the absorber, the solution takes up the vapor supplied by the evaporator because of its great avidity for water. Consequently the liquid mass fraction (concentration of the solution) is

reduced to the level of the generator input. At the same time, the solution becomes warmer since the vapor absorption is an exothermic process.

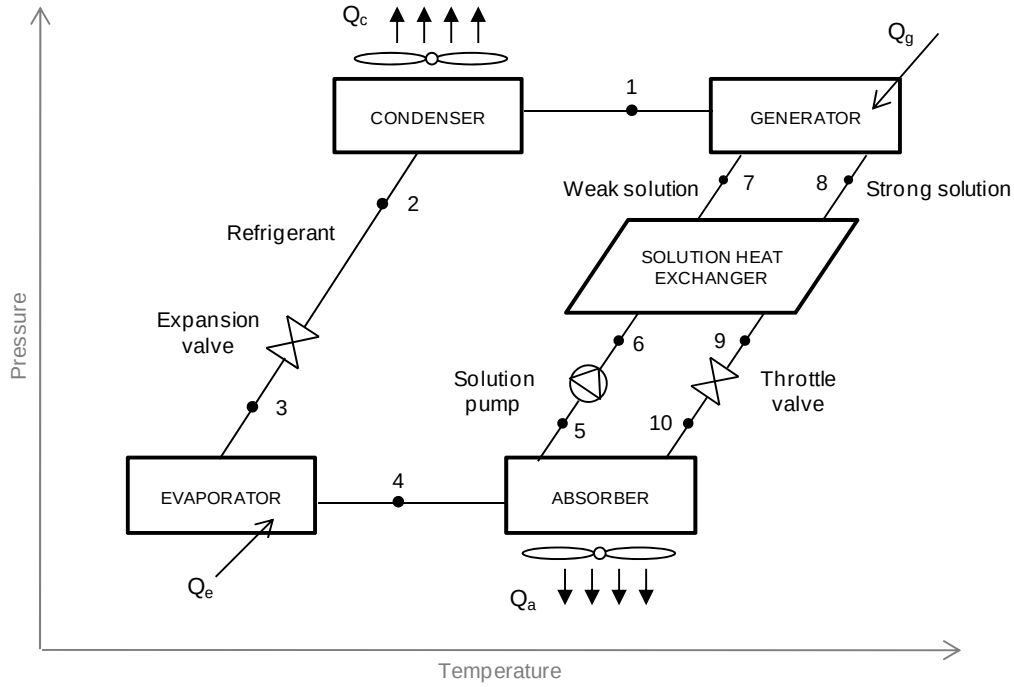

Figure 2.1 Diagram of a generic air-cooled single-effect chiller

Before entering the absorber, the concentrated solution passes through a solution heat exchanger where an exchange of sensible heat takes place. The strong solution reduces its temperature while the weak solution gets warmer. This internal heat exchanger has two main purposes: reducing the external input requirement and cooling down the concentrated solution, what strongly favor the vapor absorption process. The solution heat exchanger is then a key component in absorption machines.

Lastly, it is interesting to mention that the group of components integrating the solution loop is usually known as *thermal compressor* (Izquierdo et al., 2002), since their purpose is to suck vapor from the evaporator and, then, rise its temperature and pressure. As above mentioned, it is equivalent to the mechanical compressor in a conventional air conditioning system.

Refrigerant loop

The refrigerant loop of an absorption chiller is functionally identical to that of a vapor compression machine. The vapor produced in the generator goes directly to the con-

denser where it is liquefied by rejecting heat to a sink. Then, the liquid passes through an expansion valve in order to reduce its pressure. Although this throttling process is typically related with some vapor flashing, the vapor quality leaving the restrictor is relatively low as compared to common refrigerants used in vapor compression systems. This is because of the high latent heat of water. Once in the evaporator, the refrigerant at low pressure boils and it is driven to the absorber thanks to the absorption power of the strong solution.

2.2.2 Description of the air-cooled LiBr/H_2O double-effect cycle

The double-effect technology permits to take advantage of the higher availability associated with a higher temperature heat input (exergy). As a result, the double-effect cycles present a higher COP, approximately twice of single-effect cycles, (Gomri, 2010).

The double-effect absorption cycle has two desorbers, namely the high-pressure generator (HG) and the low-pressure generator (LG). Vapor is generated in the HG by supplying external heat (Q_{HG}). This vapor flows then to the LG, where it changes phase by rejecting heat at sufficiently high temperature that it can be used to separate vapor from the solution flowing through the LG. Thus, the input heat is used twice, which the term "double-effect" refers to.

There are two basic configurations for the double-effect cycle depending upon the distribution of the solution through the components, namely *series* or *parallel flow*. In the former case, the whole solution from the absorber goes through the two generators in series, while in the latter case part of the solution flows to the HG and the rest goes to the LG. As stated in (Arun et al., 2001), the parallel flow configuration offers a higher COP than the series flow. Furthermore, according to (Arun et al., 2000), parallel flow distribution reduces pressure drops in the solution flow. What is more, (Marcos, 2008) reported that parallel flow provides for better control of refrigerant generation.

In Figure 2.2, a schematic representation of a parallel flow double-effect LiBr/H_2O absorption cycle is shown. In the present configuration, the weak solution leaving the absorber is split into two circuits flowing in parallel. One part of the solution flows to the HG by passing through the high-temperature solution heat exchanger, and the other one goes into the LG after passing through the low-temperature heat exchanger. The two solution heat exchangers have a similar role as described for the single-effect cycle. The vapor gen-

erated in the LG is driven directly to the condenser. However, the refrigerant separated in the HG (and condensed in the LG) passes through a sub-cooler to restore its thermodynamic conditions before entering the evaporator.

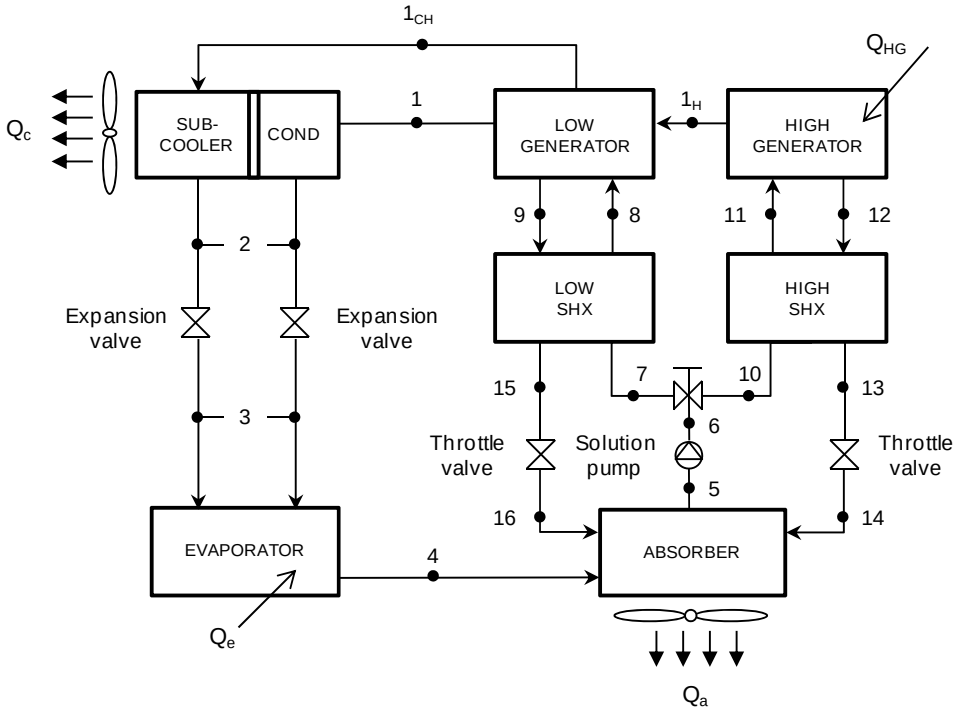

Figure 2.2 Schematic diagram of a parallel flow air-cooled double-effect chiller

Finally, note that, as represented in Figure 2.2, the condenser, the sub-cooler and the absorber are directly refrigerated by the outdoor air.

2.3 Absorption cooling market survey

Since the mid-19th century, when Edmond Carré developed the first absorption machine based on the water-sulfuric acid pair, the absorption cooling technology has been constantly evolving, especially in Japan and the USA, (Thévenot, 1978). The main application of this technology has traditionally been the large systems either for refrigeration or for air conditioning applications. In fact, the greatest part of the present absorption chiller market is taken by machines with cooling capacities higher than 35 kW, as pointed out by (Gluesenkamp et al., 2011) or (Wang et al., 2009).

On the other hand, only a few options can be found in the absorption market for small scale residential and commercial applications. Compiled from the open literature

and the manufacturers' websites, Table 2.2 lists the small capacity absorption chillers presently available in the market.

Table 2.2 Low capacity absorption chillers in the market

Cycle Type	Working pair	Manufacturer	Heating source	Cooling source	Q_e (kW)	Cooling COP
Single-effect	$LiBr/H_2O$	Sonnenklima (Germany)	Water (75-95°C)	Water	10	0.78
	$LiBr/H_2O$	EAW (Germany)	Water (80-90°C)	Water	15	0.71
	$LiBr/H_2O$	Yazaki (Japan)	Water (80-90°C)	Water	17.6	0.70
	$LiBr/H_2O$	Rotartica * (Spain)	Water (80-100°C)	Air (recooling)	4.5	0.67
	H_2O/NH_3	Pink (Austria)	Water (75-85°C)	Water	10	0.64
	$LiCl/H_2O$	ClimateWell (Sweden)	Water (85-110°C)	Water	10	0.70
Double-effect	$LiBr/H_2O$	Broad (China)	Direct-fired (150-170°C)	Water	16	1.20
	$LiBr/H_2O$	Rinnai (Japan)	Direct-fired (150-170°C)	Water	5	1.20
	$LiBr/H_2O$	Yazaki (Japan)	Direct-fired (150-170°C)	Air	28	0.85
GAX	H_2O/NH_3	Robur (Italy)	Direct-fired (180-200°C)	Air	17	0.90

* No longer in production

2.3.1 Units for solar air conditioning

As seen in Table 2.2, most of the options use the $LiBr/H_2O$ solution as a working pair. Nonetheless, the market offers other choices such as the product of the Austrian company *Pink*, which consists of a single-effect H_2O/NH_3 machine suitable for solar cooling, (Jakob & Pink, 2007). As an alternative option to solar cooling based on $LiBr/H_2O$ absorption technology, *ClimateWell* developed a single-effect machine working with a lithium chloride aqueous solution, (Bales et al., 2005). As an example of the GAX technology in the market, the company *Robur* in Italy produces a directly air-cooled water/ammonia

chiller fired by gas, although it can be modified to be driven by pressurized water of a Fresnel collector, (Häberle et al., 2007).

Regarding the single-effect LiBr/H_2O absorption chillers for solar cooling, it is drawn from Table 2.2 that, whereas one can find three water-cooled machines in the market, only one air-cooled machine is available, the *Rotartica 045v*. As a distinguishing aspect of this chiller it is worth mentioning that it has a rotary drum in which the absorption cycle takes place. The rotation is supposed to favor mass and heat transfers, (Gilchrist et al., 2002). Nevertheless, it is interesting to note that the manufacturing company went bankrupt some years ago and, as a result, the chiller is no longer commercialized.

In the literature, it is possible to find several demonstrations and research projects where several commercial LiBr/H_2O chillers were tested. For instance, experimental results for the machine manufactured by *Yazaki* working under different conditions were reported by (Asdrubali & Grignaffini, 2005) or (Syed et al., 2005). Likewise, experimental results corresponding to the *Rotartica 045v* can be found in (Izquierdo et al., 2008), (Agyenim et al., 2010) or (Monné et al., 2011). Besides, it is interesting to cite another complete study concerning *Rotartica 045v:* (Lizarte, 2010). Here, the indirect air-cooling system of *Rotartica 045v* was in-depth analyzed and compared with those directly air-cooled. As a conclusion that experimental work, it was proved that direct air-cooled absorption machines perform more efficiently than indirectly air-cooled ones.

On the other hand, the single-effect units of *EAW, Sonnenklima*, *Yazaki*, *Rotartica* and *ClimateWell* were analyzed and compared by (Asdrubali et al., 2008). The authors found that, for a driving temperature of 85°C and a chilled water temperature of 9°C, the coefficients of performance taking account of the electricity consumption were 0.64, 0.59, 0.52 and 0.53, respectively. Those results were obtained for a cooling source temperature of 30°C. However, the authors concluded that the performance of all the studied chillers dramatically drops when the cooling source temperature exceeds 35°C.

2.3.2 Double-effect chillers

As drawn from Table 2.2, currently in the market it is possible to find three double-effect absorption machines with low cooling capacities. Two of them are water-cooled units, *Broad* and *Rinnai*, while the third model, the *Yazaki ACH-8,* is air-cooled. Moreover, it

is interesting to note that all of them are directly fired by a fuel. No indirect-fired double-effect machines are available for use with waste heat or in trigeneration systems.

Regarding the only air-cooled double-effect chiller in the market, it is fired by natural gas, it presents a nominal cooling capacity of 28 kW and its COP at ambient temperatures of 35°C is 0.85, without taking account of the electricity consumption. Besides, as reported by (Tongu et al., 1993), at outdoor temperatures of 40°C, the provided cooling power decreases to 67% of the cooling capacity. In turn, it cannot work at ambient temperatures higher than 43°C. What is more, the size of this absorption machine is quite huge, about 4.4 m^3. In 2000, the manufacturing company *Yazaki* patented a new solution to be used in this machine, (Yazaki Corporation, 2000), but this new model has not been launched yet, as far as we know.

2.4 Outlook for absorption technologies

On the grounds of the absorption cooling market survey, it can be said that, presently, there is not any air-cooled chiller available for small scale solar air conditioning applications. What is more, it is not possible to find any commercial solution which ensures a reliable and environmental friendly supply of the cooling demand corresponding to a residential or commercial space. Accordingly, our research group strongly believe that, in order to make solar cooling really competitive with conventional air conditioning systems, great efforts must be put into developing low capacity air-cooled absorption machines powered by solar energy, when solar radiation is available, or by efficiently firing a fuel when not.

2.4.1 Development of air-cooled absorption chillers

Development of air-cooled absorption technology is actually receiving an increasing attention by the scientific community. In fact, it was proposed as an important subject in the future R&D in relevant publications like (Kim & Infante-Ferreira, 2008b) or (IEA, 2007). However, apart from the bigger size of the components, this technology presents a major drawback: the likely crystallization of solution when working at higher temperatures. In order to overcome this difficulty, especially associated with the widely used $LiBr/H_2O$ solution, several studies have been performed for the last years. In this sense, in (Wang et al., 2011) a summary of the main strategies proposed to avoid crystallization can be found. Broadly speaking, the main proposals can be grouped into two major actions:

- Finding new working solutions with a wider range of solubility, normally by adding some extra components to the basic pair LiBr/H_2O.
- Developing new absorber designs that permit both a good vapor absorption process and an effective heat evacuation.

With the purpose of developing air-cooled LiBr/H_2O absorption chillers, the *Energy Saving and Emissions Reduction in Buildings* research group opted for the latter option. In this vein, a new generation absorber was developed between 2003 and 2006 under research projects DPI 2002-02439 and ENE 2005-08255-CO2-01, with funding from Spain's Ministry of Industry. As distinguishing features of this innovative device, it is interesting to underline that it consists of a directly air-cooled adiabatic absorber using flat-fan sheets distribution. Besides it is smaller, more readily assembled and with higher mass and heat transfer coefficients than in place to date, (Izquierdo et al., 2010). Up to now, this absorber has been assembled into two direct air-cooled LiBr/H_2O absorption prototypes with excellent results, (González-Gil et al., 2011) and (Izquierdo et al., 2011c).

2.4.2 Development of integrated single–double-effect absorption machines

As earlier mentioned, a very promising idea to efficiently supply the air conditioning demand of a residential or commercial space is to use an absorption machine that combines single- and double-effect cycles in the same unit. In this way, when solar energy was available, it might be used to power the machine and produce cooling with no harmful emissions. In turn, when solar radiation levels were not high enough to run the single-effect stage, the machine could be powered by firing a fuel in the double-effect operation mode, which yields a much higher cooling COP. Besides, if the double-effect stage were designed to be indirectly fired, waste heat, for example coming from an engine in a co-generation plant, could be used to efficiency provide air conditioning.

The concept of combining single- and double-effect into the same absorption chiller has also been regarded as an excellent option to reliably supply cooling by other authors. In this sense, the combination of an absorption system with an internal combustion engine was patented to permit the simultaneous use of both the exhaust gas and the cooling water of the engine, (Mori et al., 1984). In this case, the engine exhaust gas at temperatures of about 700°C powers the double-effect stage of the absorption machine, while the engine cooling water, at temperatures from 60°C to 150°C, drives the single-effect cycle. However, the system needs a cooling tower to be refrigerated.

On the other hand, the operation of a single–double-effect LiBr/H_2O absorption machine is described in (Riepl et al., 2011). It essentially consists of a commercially available single-effect hot water driven chiller which has been adapted for the integration of the double-effect stage, directly gas-fired. The chiller, which has been designed to be installed in large capacity systems, needs a cooling tower as well.

2.5 Conclusion

To sum up, the development of air-cooled single–double-effect LiBr/H_2O absorption machines is plenty of interest nowadays. What is more, it is regarded as a very appropriate solution to make solar air conditioning be competitive with conventional vapor compression systems, especially in small scale applications.

Chapter 3

Description of the single–double-effect absorption prototype

3.1 Introduction

In this chapter, a new single–double-effect absorption prototype for solar cooling applications will be described. Firstly, the design parameters required for its construction will be specified. Then, the principles of working and details of its components will be given. Besides, the testing facilities utilized to evaluate the performance of the prototype will be described.

3.2 Description of the prototype

3.2.1 Requirements of design

With the aim of covering the lack detected in the current absorption technology (Chapter 2), the *Energy Saving and Emissions Reduction in Buildings* research group has designed and built a novel absorption prototype under the project INVISO-subproject SP3, with funding from Spain's Ministry of Industry. The design of the prototype meets the following requirements:

1. It integrates both single- and double-effect cycles in the same absorption machine.
2. In the single-effect operation mode, it is driven by solar heat and the cooling capacity is 4.5 kW.
3. The double-effect stage, with 7 kW as nominal capacity, is indirectly fired by a heat source such as waste heat or fuels, fossil or renewable.
4. It presents a compact design, with a final size of about 1 m^3.
5. The working solution is LiBr/H_2O.
6. The absorption and condensation heats are directly removed from the machine by the surrounding air.
7. The absorber is compact and avoids the solution crystallization under extreme outdoor temperatures.
8. The evaporator of the absorption machine is able to maintain water in a fan-coil circuit between 10°C and 16°C, depending on the outdoor temperature.

3.2.2 General description

Figure 3.1 shows the block diagram of the single–double-effect absorption prototype presented and analyzed in this work. As observed, most of the main components of the machine are common for both working modes of the prototype. Actually, we have that both the single- and the double-effect stages operate with the same solution pump, evaporator, absorber and condenser. Only the generators and the solution heat exchangers are specific for each stage.

A series of valves were installed in the prototype with the purpose of separating both stages, namely: V1, V2, V3, V4 and V5, in Figure 3.1. When solar irradiation is high enough to power the single-effect stage, valves V1 and V3 are kept open while valves V2, V4 and V5 are completely closed. Conversely, in cases of insufficient solar irradiation the double-effect mode is activated by closing V1 and V3 and opening V2, V4 and V5. Note that both V1 and V2 are regulating valves; that is, they permit to control the solution flow towards the corresponding generators. In turn, valves V3, V4 and V5 are uniquely for maintaining the low pressure level in the evaporator and the absorber while operating one of the stages in the prototype.

When working in single-effect mode, the solution is driven from the absorber to the single-effect (SE) generator by means of the solution pump (SP). In the generator, thermal energy is added (Q_G) and the refrigerant (water) boils off the solution. Then, the concentrated solution returns to the absorber passing through a solution heat exchanger (SE-SHX). Before entering the absorber, the solution pressure is reduced into a throttle valve (SE-TV). The refrigerant separated from the solution flows to the condenser, where heat is rejected to the atmosphere as condensation process occurs. Once condensed, the refrigerant flows through an expansion valve (L-VE) and reaches the evaporator, where by means of the heat from the cooling load (Q_e) is evaporated again. In the absorber, the solution soaks up the refrigerant vapor and, as a result, the absorption cycle is completed. The heat generated during the absorption process (Q_a) is removed by means of a solution-air cooler assembled to the adiabatic absorber, which basically consists of a recirculation solution pump (RSP) and two finned heat exchangers.

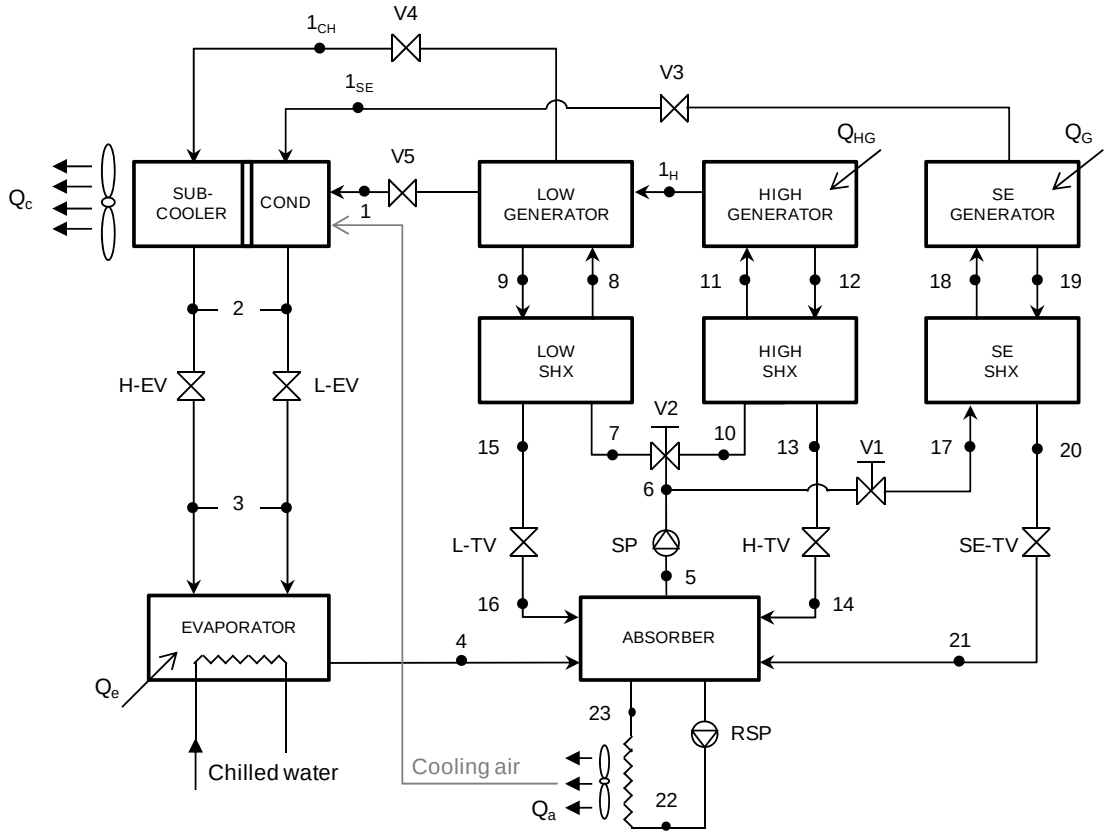

Figure 3.1 Schematic diagram of the single–double-effect prototype

As regards to the double-effect operation mode, the parallel flow configuration was selected because of the reasons given in Chapter 2. As seen in Figure 3.1, the valve V2 di-

vides the solution leaving the absorber into two parallel flows. One flow is driven to the high-pressure generator and the other to the low-pressure generator. Similarly to the single-effect stage, the solution flowing back to the absorber is cooled in the corresponding solution heat exchangers (High- and Low-SHX). The refrigerant separated in the high-pressure generator (point 1_H) is condensed in the low-pressure generator and, then, it is driven to an air-type subcooler where its temperature is reduced. The latent heat rejected during the condensation process in the low-generator is used to separate an additional amount of refrigerant (point 1). This new refrigerant is condensed in the condenser and then, it flows to the evaporator through the same expansion valve as for the single-effect stage (L-EV). The absorption process occurs in the same manner as explained for the single-effect stage.

On the other hand, the prototype's design permits a combined operation of single- and double-effect cycles. Therefore, it can be stated that the present absorption prototype has three cooling operation modes:

a) *Pure solar single-effect mode*, when solar heat temperature is high enough to provide the whole cooling demand. The nominal cooling power under this operation mode is 4.5 kW and the expected COP is about 0.6.

b) *Pure double-effect mode*, when available solar heat temperature is not sufficient to power the single-effect stage. The cooling demand is provided exclusively by burning a fuel (or by means of waste heat). The cooling capacity in this case is 7 kW and the COP is about 1.1.

c) *Solar-assisted mode,* when available solar heat is able to power the single-effect stage but the cooling demand cannot be exclusively met by this means. The double-effect stage provides part of the cooling demand depending on the availability of solar heat. The cooling capacity is 10 kW and the COP varies between 0.6 and 1.1, depending on the solar fraction.

On those grounds, it can be said that the proposed absorption prototype is well suited for application in solar cooling plants, where the availability of the heat source is not constant. Likewise, it is interesting to note that the cooling capacity of the pure solar single-effect mode has been designed to provide around 65% of the prototype's nominal capacity, which permits a reasonable ratio of investment and solar coverage.

Regarding the appearance of the prototype, it is noteworthy the compactness achieved, especially taking into account that it is an air-cooler machine. The final dimensions are 1.2 m length, 0.8 m width and 1 m high, which yields a volume of about 1 m^3.

3.2.3 Description of the main components

In this subsection, the main components of the single–double-effect absorption prototype will be characterized.

Generators

As earlier mentioned, one of the requirements for the prototype was to achieve a compact design. On account of this, plate heat exchangers (PHE) were used in every generator of the absorption machine. It is well known that this kind of devices presents a high ratio of heat transfer rates to volume and, consequently, may reduce the final size of absorption machines (de Vega et al., 2006).

The high-pressure generator is indirectly fired; that is, an intermediate fluid previously heated by an external source like waste heat or fuel combustion flows through one of the sides of the PHE. In the other side of the PHE, the $LiBr/H_2O$ solution pumped from the absorber flows and, as a result of the heat transfer taking place, part of the refrigerant boils off the solution. The behavior of this kind of heat exchangers working as high-pressure generator was in-depth studied by (Marcos et al., 2009).

Regarding the low-pressure generator, it consists of a PHE with similar characteristics to the previous one, except for the heat transfer capacity, which is lower. In this case, $LiBr/H_2O$ solution from the absorber flows through one side of the PHE, while in the other side the refrigerant previously separated in the high-generator is condensed. In the literature, one can find some previous works reporting on absorption prototypes where PHEs were used as low-pressure generators, (Marcos, 2008) and (Izquierdo et al., 2011c). Notwithstanding, there is not any study specifically analyzing the heat transfer coefficients nor the pressure drops in this kind of generators.

The PHE used as generator in the single-effect stage is analogous to the other generators in the prototype. In one of its sides, the solution from the absorber flows and boils. In the other side, the hot water from the solar facility delivers the heat needed to boil the solution.

It is also interesting to mention that a solution-vapor separator is placed at the outlet of each generator in the prototype. The design of these devices was developed by our research group and a detailed description can be found in (Marcos, 2008). Additionally, a flow viewer was installed at the outlet of each separator to check that no solution flows through the vapor tubes. In Figure 3.2, it is observed the vapor flowing through the viewer installed at the outlet of the single-effect generator.

Figure 3.2 Detail of the vapor flow viewer at the outlet of each generator

Solution heat exchangers

In the same manner as for the generators, the three solution heat exchangers in the prototype are plate heat exchangers. The main function of this kind of devices is to reduce the temperature of the solution coming from the generators before entering the absorber. At the same time, the solution flowing to the generators is preheated and, as a result, the input energy needed to boil the solution is lower.

Condenser and subcooler

The condenser of the prototype is a finned heat exchanger where coolant separated in both the low-generator and the single-effect generator is directly condensed by the outdoor air. Refrigerant flows inside a cooper tube while air circulates through the aluminum fins in a cross flow configuration. As well know, the heat transfer coefficients of the air are quite low, thus the importance of increasing the air-side surface by means of the fins.

The subcooler is a heat exchanger similar to the condenser but with a considerably lower heat transfer capacity. The function of this device is to reduce the temperature of the refrigerant condensed in the low-generator, ensuring besides that no vapor flows to the expansion valve.

The condenser and the subcooler are horizontally placed just below the fan. They are installed in such a way that the air coming from the heat exchanger of the adiabatic absorber firstly passes through the condenser and then through the subcooler.

Evaporator-absorber assembly

In this prototype, the evaporator and the absorber are assembled together in the same chamber, Figure 3.3. In this way, the water vapor generated in the evaporator is directly absorbed by the solution in the absorber. The lack of piping between these two components significantly reduces the pressure drop and consequently improves the absorption process, (Izquierdo et al., 2010).

The evaporator basically consists of a falling film heat exchanger where the chilled water circulates inside a cooper coil and the refrigerant drops on its outer surface. With the purpose of improving the heat transfer from the chilled water to the refrigerant, both inner and outer surfaces of the tube coil tube are enhanced surfaces. In this sense, while the inner surface presents helical fins, the outer of the tubes is a micro-structured surface. The effect of this kind of surface enhancements is in depth studied in (Thome, 2004), (Poniewski & Thome, 2008) or (Christians, 2010).

Regarding the absorber assembly, it is interesting to note that it transfer mass and heat separately, as an adiabatic unit. It basically comprises a tank to store the diluted solution, a bank of flat-fan sheet sprayers, a solution pump and an air-cooling system to refrigerate the solution. The storage tank collects concentrated solution coming from the generators through three sprayers, one for each return. In this process, the strong solution absorbs a considerable amount of the vapor generated in the evaporator and, consequently, gets warmer. In order to remove this absorption heat, a solution air-cooler was assembled. This cooling system is formed by a recirculation solution pump, two finned heat exchangers and a fan. The diluted and warmed solution is pumped from the tank through the heat exchangers, where it is refrigerated directly by the outdoor air. Once cooled, the solution returns to the absorber storage tank through a few of sprayers, also contributing to the vapor absorption process. Lastly, part of the solution in the tank is driven again to the generator by the solution pump.

As will be seen in Chapter 5, the selected absorber configuration increases both the mass and the heat transfer coefficients, significantly reducing the absorber volume. Notice

that one of the design requirements for the prototype was installing a compact prototype which allows working with relatively low solution temperatures.

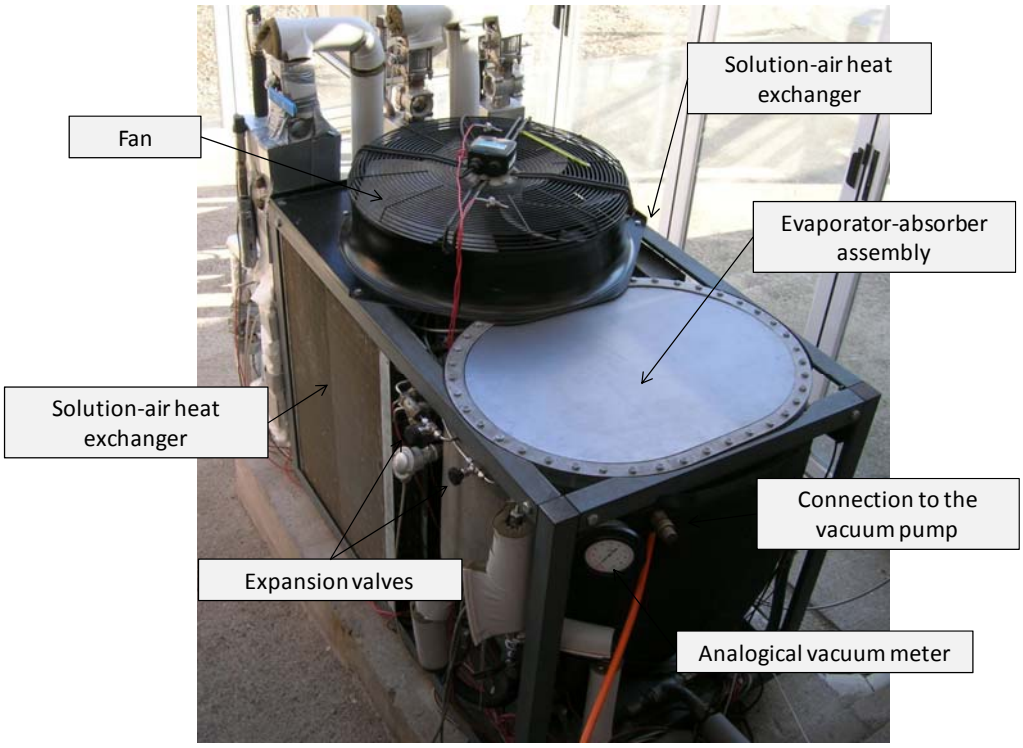

Figure 3.3 View of the evaporator-absorber assembly

Expansion devices

Two expansion valves where installed in the prototype: the first at the outlet of the condenser and the second at the exit of the subcooler. They consist of two flow restrictor devices generating a pressure drop in the refrigerant entering the evaporator chamber. As seen in Figure 3.3, they are hand controlled valves.

Air-cooling system

As depicted in Figure 3.1, the air-cooling system of the prototype is designed in such a way that, with only a fan, the absorber, the condenser and the subcooler are cooled at the same time. The surrounding air firstly passes through the absorber heat exchangers, then through the condenser and finally through the subcooler. This series flow configuration permits to work with lower absorption temperatures and yields more compact designs. A similar air flow distribution was also utilized by (Izquierdo et al., 2011c) in a double-effect prototype, or by (Castro et al., 2008) in a single-effect prototype.

Figure 3.3 illustrates the air-cooling system of the absorption prototype. The fan on the top of the machine sucks the surrounding air through both two solution-air heat exchangers forming the absorber cooler. Note that those finned heat exchangers have the same geometry and have been symmetrically installed on both sides of the prototype so that the air flow rate through each of them is the same. The condenser and the subcooler have been horizontally installed just below the fan.

Piping materials

In this prototype, the tubes and surfaces in contact with the $LiBr/H_2O$ solution are made of stainless steel, while those ones exclusively contacting water are made of copper. Even though the aqueous LiBr solution is known to be highly aggressive to these metals (and to many others) in the presence of dissolved oxygen, the hermetic environment inside an absorption machine strongly reduces the amount of oxygen and, consequently, the corrosion rates are much slower.

Vacuum system

From the design requirements, it can be drawn that the needed evaporation temperatures are between 8°C and 14°C, which implies vapor pressures around 1 kPa (or 10 mbar). Although these pressure levels are not particularly low, the sensibility of $LiBr/H_2O$ absorption technology to leaks is very high, not only because of performance considerations, but also because of corrosion problems. This fact makes indispensable to control the vacuum inside the prototype in a very effective way.

In the construction of the prototype, special care was taken into sealing all the joints. Besides, in order to ensure no vacuum loses occur through the solution pumps, magnetically driven gear pumps were utilized. Additionally, a vacuum pump and a vacuum meter were installed in the prototype, Figure 3.3. This vacuum system permits to pump out the air from the absorption machine before introducing the solution for the first time. What is more, this system enables to recover the low pressures in case of maintenance operations are needed.

3.3 Description of the prototype testing facilities

In order to test the single–double-effect absorption prototype, a group of testing facilities has been installed in the CSIC's Experimental Plant of Solar Energy, which is located in Arganda del Rey, Madrid (Figure 3.4).

Figure 3.5 shows a schematic representation of the experimental facilities. As seen, the whole installation essentially consists of three subsystems, namely: hot source supplier, absorption prototype and chilled water distribution. Note that, in order to supply the energy needed to drive the prototype, the system accounts with a solar facility and a thermal oil heater. In general, the solar facility will power the single-effect stage whereas the thermal oil will be used to fire the double-effect mode.

Figure 3.4 CSIC's Experimental Plant of Solar Energy in Arganda del Rey (Madrid)

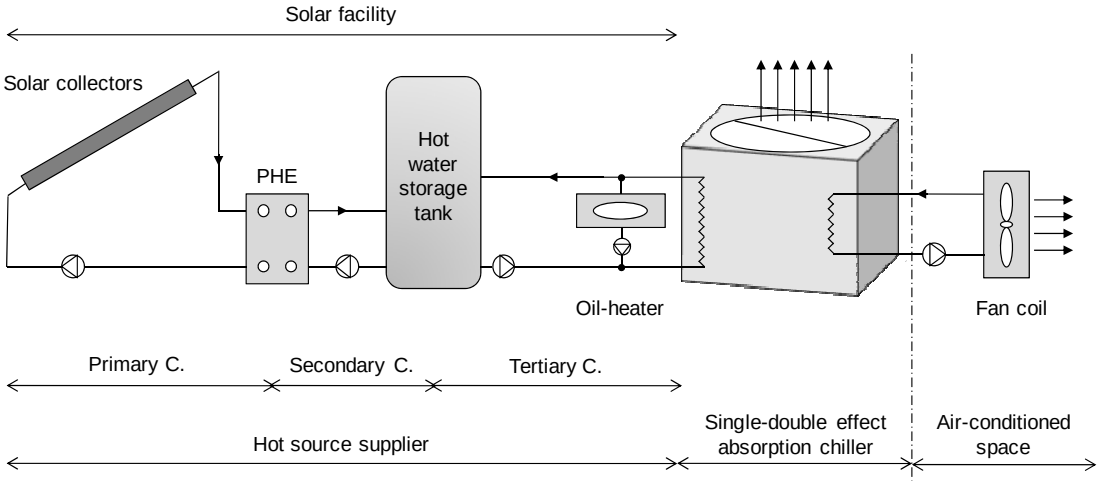

Figure 3.5 Facilities to test the single–double-effect prototype

In Figure 3.6, one can see the prototype and its two driving facilities. The thermal oil heater is on the left of the picture while the solar facility is at the back. On the other hand,

from Figure 3.6 it is interesting to note that the prototype is placed inside a climatic chamber which permits to simulate outdoor summer conditions when necessary, even in winter. Needless to say that the climatic chamber is unclosed for summer tests.

Following, a more detailed description of each testing facility is shown.

Figure 3.6 Photograph of the prototype and its driving facilities

3.3.1 Solar facility to test the single-effect stage

The solar facility designed to produce the hot water feeding the prototype's single-effect generator is formed by three different circuits (Figure 3.5). The primary circuit consists of a 48 m^2 field of evacuated flat plate solar collectors (42 m^2 of useful surface), a water pump and the hot side of a plat heat exchange. The secondary circuit, designed to store the solar energy transferred from the primary circuit, includes the cold side of the PHE, a water pump and a 1500 l stratified storage tank. Lastly, in the tertiary circuit, a pump drives the hot water from the tank to the prototype's generator. In order to avoid overheating situations, the solar facility includes a heat-dissipation system installed in the tertiary circuit.

The whole solar facility is automatically controlled in order to achieve a high performance. Worth mentioning is that water pump in the secondary circuit is allowed to run

only when temperature in this circuit is 2-7°C higher than temperature in the storage tank. In Figure 3.7, a picture of the solar facility is shown.

Twenty-four evacuated flat plate collectors, with 1.76 m^2 of absorber surface area each, were used in this solar facility. South-facing installed (30°), they were arranged in four groups in such a way that each group presents the same pressure drop. This design enables to achieve a hydraulic equilibrium and makes each collector perform at its highest. Unlike conventional flat plate collectors, in this case vacuum is maintained between the absorber surface and the collector glaze, providing a much higher insulation performance. As a result, the working fluid can reach higher temperatures.

Figure 3.7 Solar facility

A water-glycol solution (30 wt%) was used as working fluid in the primary circuit, allowing a range of operation temperatures from -10°C to 125°C. By contrast, in both the secondary and tertiary circuit a concentration of 10 wt% was used, since the working temperatures are not so extreme. Nominal flows corresponding to primary, secondary and tertiary circuits are, respectively, the following: 1.7 m^3/h, 1.3 m^3/h and 1 m^3/h. As for the electrical power of the water pumps, the nominal values are, respectively: 295 W, 175 W and 110 W.

In case of cloudy days, the prototype may be also tested by means of the aforementioned oil heater, which is able to rise the temperature of a thermal oil circuit. This thermal fluid may feed the prototype's generator instead of the solar warmed water when solar radiation is not available.

3.3.2 Thermal oil facility to test the double-effect stage

This facility basically consists of an isolated thermal oil tank with electrical resistances, a pump (AM880KY4 from *AEG*) and a circuit driving the fluid to the prototype's generators. The circuit is configured in such a way that, by opening or closing a couple of valves, thermal oil can be supplied either to the high-generator in the double-effect stage or to the single-effect generator. Electrical resistances inside the tank may provide a maximum power of 10 kW, heating up the thermal oil above 200°C.

3.3.3 Air conditioned space and chilled water circuit

The water chilled in the prototype's evaporator is delivered to a fan coil placed inside a room of the laboratory, which is the space to be air conditioned. The room has a net floor area of 40 m^2 and a volume of 120 m^3. It is supposed to be occupied for a mean of three people from 9:00 h to 20:00 h. According to the methodology presented in (Izquierdo et al., 2011a), it is assessed that, at an outdoor temperature of 42°C, the thermal load for a comfortable indoor temperature of 24°C is about 4.5 kW.

The chilled water circuit consists of a pump and a water-air heat exchanger (fan coil) which refrigerates the space. The maximum cooling capacity of the fan coil is 10 kW. Piping is made of cooper and is properly isolated to minimize thermal loses

3.4 Conclusion

This chapter described the new single–double-effect absorption prototype presented in this thesis. Principles of working and details of its components were given. Besides, a brief description of the facilities used to test the prototype was included in this chapter.

Chapter 4

Simulation of single- and double-effect direct air-cooled LiBr/H_2O absorption machines

4.1 Introduction

In this chapter, two simulation codes will be developed for the parametric investigation of single-effect and parallel flow double-effect LiBr/H_2O absorption machines. The mathematical models will be applied to assess the main working parameters of the single–double-effect prototype in both operation modes: single- and double-effect. Comparison of the prototype simulation outcomes with experimental results will be performed in Chapter 6 and Chapter 7.

4.2 Mathematical modelling of direct air-cooled single-effect chillers

In the open literature, one can find a vast number of works describing different analytic models of single-effect absorption cycles, such as, (Joudi & Lafta, 2001), (Kohlenbach & Ziegler, 2008), (Kim & Infante-Ferreira, 2008a), (Arora & Kaushik, 2009) or (Banasiak & Koziol, 2009). Most of them are, however, either complex to implement or too highly computer source consuming for the purpose of this work. Therefore, based on the principles of

energy and mass conservation that can be found in (Herold et al., 1996) and (Izquierdo, 1996), a simple mathematical model was developed for quick steady state simulation of direct air-cooled single-effect LiBr/H_2O absorption chillers.

Below, energy and mass balances for each component of the cycle are presented for a refrigerant flow rate of $\dot{m}_r = 1$ kg/s. Nomenclature of state points is based on the schematic shown in Figure 2.1.

Generator

If the solution mass flow rate passing through the generator is $\dot{m}_s$ and the vapor rate separated is $\dot{m}_r$, then an energy balance in this component yields

$$q_g + \dot{m}_s h_7 - \dot{m}_r h_1 - (\dot{m}_s - \dot{m}_r) h_8 - q_{l,g} = 0$$

where $q_{l,g}$ represents the heat loss to the ambient. Considering the generator as an adiabatic component, the input heat to the generator per unit of refrigerant mass flow can be written as

$$q_g = (h_1 - h_8) + \dot{m}_s (h_8 - h_7) \tag{4.1}$$

Absorber

An energy balance in the absorber can be expressed as

$$-q_a + \dot{m}_r h_4 - \dot{m}_s h_5 + (\dot{m}_s - \dot{m}_r) h_{10} - q_{l,a} = 0$$

Neglecting the thermal losses to the ambient ($q_{l,g}$), the heat that must be removed from the absorber per unit of refrigerant mass flow is given by

$$q_a = (h_4 - h_{10}) + \dot{m}_s (h_{10} - h_5) \tag{4.2}$$

Solution heat exchanger

From an energy balance in the solution heat exchanger, the heat recovered by the weak solution is defined by

$$q_{shx} = \dot{m}_s (h_7 - h_6) \tag{4.3}$$

Considering an adiabatic heat exchanger, the heat delivered by the strong solution can be calculated by

$$q_{shx} = (\dot{m}_s - 1)(h_8 - h_9) \tag{4.4}$$

The effectiveness of the solution heat exchanger is defined as the ratio between the heat delivered by the strong solution and the maximum heat that could be recovered. That is to say

$$\varepsilon_{shx} = \frac{h_8 - h_9}{h_8 - h_6} \tag{4.5}$$

Throttle valve

In this flow restrictor, it is considered that an isenthalpic pressure reduction takes place. Thus, the following expression can be written

$$h_9 = h_{10} \tag{4.6}$$

Solution pump

From an energy balance in the solution pump, its energy consumption is given by

$$w_p = \dot{m}_s(h_5 - h_6) \tag{4.7}$$

Condenser

An energy balance in the condenser can be expressed as

$$-q_{cond} + \dot{m}_r(h_1 - h_2) - q_{l,cond} = 0$$

Neglecting thermal losses to the ambient, the condensation heat per unit of refrigerant mass flow is calculated by

$$q_{cond} = (h_1 - h_2) \tag{4.8}$$

Expansion valve

As it is assumed that an isenthalpic expansion of the liquid refrigerant occurs, it can be written that

$$h_2 = h_3 \tag{4.9}$$

Evaporator

In the evaporator, an energy balance can be expressed as

$$q_e + \dot{m}_r h_3 - \dot{m}_r h_4 + q_{l,e} = 0$$

Considering that no thermal losses to the ambient take place, the evaporation heat per unit of refrigerant is obtained as

$$q_e = (h_4 - h_3) \tag{4.10}$$

Mass balance

Assuming that in point 1 there is only pure water vapor, the following mass balance can be written for the refrigerant in the generator

$$\dot{m}_s(1 - X_a) = (\dot{m}_s - \dot{m}_r)\big(1 - X_g\big) + \dot{m}_r$$

where X_a and X_g represent the LiBr mass fraction in the solution circulating through the absorber and the generator, respectively. From this expression, the following flow ratio between the solution and the refrigerant mass flows can be drawn

$$FR = \frac{\dot{m}_s}{\dot{m}_r} = \frac{X_g}{X_g - X_a} \tag{4.11}$$

The water vapor mass flow circulating in the refrigerant loop can be defined as the ratio between the cooling power required in the evaporator (Q_e) and the evaporation heat per unit of refrigerant (q_e). Considering that the cooling load in the evaporator is equal to the thermal load of the air conditioned space (Q_{room}), the following equation can be used to calculate the refrigerant mass flow

$$\dot{m}_r = \frac{Q_e}{q_e} \tag{4.12}$$

Coefficient of performance and electricity consumption

The thermal coefficient of performance corresponding to an absorption chiller is obtained as the following ratio

$$COP_{th} = \frac{Q_e}{Q_g} \tag{4.13}$$

For obtaining the electricity consumption of the solution pump, the following equation can be used

$$W_p = \frac{w_p \cdot m_s}{\eta_p} \tag{4.14}$$

where η_p represents the efficiency of the pump in converting electricity into mechanical power.

4.3 Simulation of direct-air-cooled single-effect absorption machines

Based on the above mathematical model and following the assumptions exposed below, a computational algorithm was implemented in *Matlab* to perform simulations of single-effect direct air-cooled absorption machines. In this case, the model was applied to simulation of the prototype's single-effect operation mode. The thermodynamic properties corresponding to all the working fluids were obtained according to (Pátek & Klomfar, 2006) and (ASHRAE, 2009).

4.3.1 Assumptions

Some general simplifying assumptions were made to carry out the numerical simulation. These are:

- The refrigerant vapor leaving the generator is considered to be superheated water vapor at the generator temperature.
- The refrigerant leaving the condenser and the vapor leaving the evaporator are assumed to be saturated.
- The solution leaving both the absorber and the generator is assumed to be saturated in equilibrium conditions at the respective temperatures and concentrations.
- The solution heat exchanger has a constant effectiveness.
- The heat and pressure losses in the components are negligible.

Table 4.1 shows some additional assumptions made to simulate the prototype's single-effect stage. Since presently in the market there is not any commercial $LiBr/H_2O$ absorption chiller directly cooled by air, the assumptions made to simulate the absorption prototype correspond to its design specifications. As described in Chapter 3, the prototype includes an adiabatic absorber directly cooled by the surrounding air. Besides, it is interesting to note that the prototype was designed in such a way that the same air flow firstly refrigerates the absorber and then the condenser.

Table 4.1 Design parameters assumed for the prototype's single-effect operation mode

Parameter	Prototype
T_{cond}	T_{out} + 11
T_a	T_{out} + 6
ε_{shx}	0.8
η_p	0.7

The evaporation temperature in a direct air-cooled absorption system is supposed to vary linearly with the ambient temperature, according to (Marcos, 2008).

Regarding the increment of the solution concentration in the generator, a safety margin of 1.5% with respect to the crystallization limit is assumed, (Marcos et al., 2011a).

4.3.2 Simulation results

To begin with the single-effect simulation results, Table 4.2 shows some of the main parameters obtained for the absorption prototype working under two particular ambient temperatures: 36°C, which is a very common summer temperature not only in Madrid, but also in the Mediterranean coast; and 41°C, which represents extreme working conditions, rarely reached in Spain.

From that table, it is interesting to bring out the high performance expected for the prototype not only at outdoor temperatures close to the design point (35°C), but also at very high ambient temperatures. As for any air-cooled refrigeration machine, both the cooling capacity and the coefficient of performance decrease with high ambient temperatures. However, it is remarkable the reasonably high performance expected for this prototype at extreme outdoor temperatures. In this vein, we have that the cooling capacity at

41°C is just about 25% lower than nominal capacity (4.5 kW). Likewise, a COP of 0.60 is predicted for that ambient temperature, which is not far from values corresponding to water-cooled single-effect absorption machines reported on the literature.

Table 4.2 Main working parameters expected for the prototype's single-effect stage

Working parameter	T_{out} = 36°C	T_{out} = 41°C
Q_e (kW)	4.4	3.8
Q_g (kW)	6.2	6.3
Q_a (kW)	5.8	5.9
Q_{cond} (kW)	5.6	5.7
COP_{th}	0.71	0.60

In Figure 4.1, the thermodynamic cycles described by the prototype working at the aforementioned ambient temperatures are plotted in a Dühring chart. It can be seen that great increments of concentration may be reached in the generator since the adiabatic absorber enables to operate at the relatively low absorption temperatures. The high effectiveness of the solution heat exchanger also plays a relevant role in that sense.

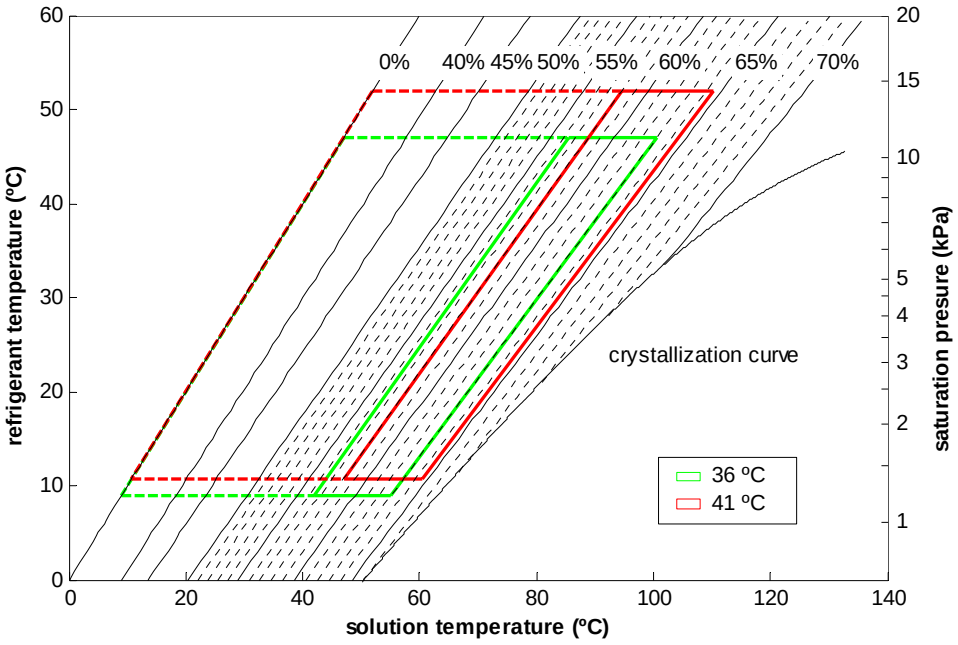

Figure 4.1 Dühring plot expected for the prototype working at 36°C and 41°C in single-effect mode

On the other hand, Figure 4.2 shows the numerical results for the COP_{th} of prototype working under the weather conditions of a real summer day in Madrid. In that day, which is 13 July 2010, the highest outdoor temperature was 38.5°C at 17:00 h.

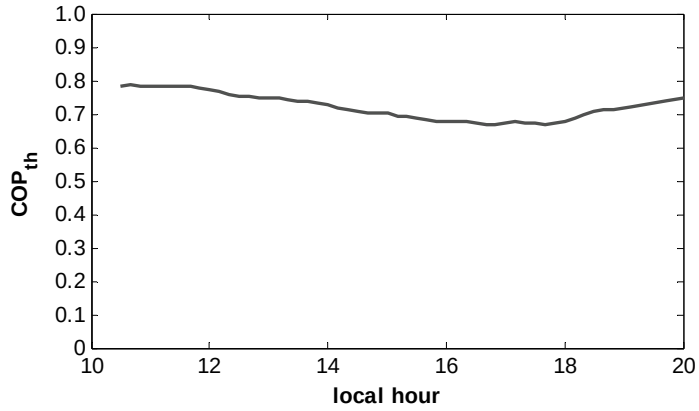

Figure 4.2 Thermal COP of the prototype's single-effect stage on a real day: 13/07/2010

Regarding the validation of the model, we have to say that there is not any direct air-cooled single-effect absorption machine in the market to establish comparison. On these grounds, the obtained results were compared with those published in a recent paper reporting on a new method to simulate this kind of machines, (Marcos et al., 2011a), and an excellent agreement was found.

4.4 Mathematical modelling of direct air-cooled double-effect chillers

As for the single-effect modelization, in the literature one can find a large number of works studying double-effect absorption cycles, for instance (Wang et al., 2007) or (Gomri & Hakimi, 2008). However, in the present work an alternative mathematical model was developed to perform a parametric analysis of the prototype's double-effect operation mode. The modelization is made for air-cooled parallel flow double-effect LiBr/H_2O absorption chillers. Following, the governing equations obtained from energy and mass balances in each component, all assumed adiabatic, are presented.

High-pressure generator (HG)

Assuming the refrigerant flow rate separated in this generator is $\dot{m}_{r,1H}$, the energy and mass balances can be written as

$$Q_{HG} = \dot{m}_{r,1H} h_{1H} + \dot{m}_{12} h_{12} - \dot{m}_{11} h_{11} \tag{4.15}$$

$$\dot{m}_{11} = \dot{m}_{r,1H} + \dot{m}_{12} \tag{4.16}$$

$$X_{11} \dot{m}_{11} = X_{12} \dot{m}_{12} \tag{4.17}$$

$$\frac{\dot{m}_{11}}{\dot{m}_{r,1H}} = \frac{X_{12}}{X_{12} - X_{11}} \tag{4.18}$$

$$\dot{m}_{r,1H} = \frac{Q_{HG}}{\frac{X_{12}}{X_{12} - X_{11}} \cdot (h_{12} - h_{11}) + (h_{1H} - h_{12})} \tag{4.19}$$

Low-pressure generator (LG)

As above mentioned, the heat source for this desorber is the refrigerant vapor separated in the HG, which transfers its latent heat to the solution (Q_{LG}). The input power can be therefore written as

$$Q_{LG} = \dot{m}_{r,1H} \cdot \left(h_{1H} - h_{1,CH}\right) \tag{4.20}$$

If $\dot{m}_{r,1}$ is the refrigerant separated in the low-generator, the energy and mass balances for this component can be expressed as

$$Q_{LG} = \dot{m}_{r,1} h_1 + \dot{m}_9 h_9 - \dot{m}_8 h_8 \tag{4.21}$$

$$\dot{m}_8 = \dot{m}_{r,1} + \dot{m}_9 \tag{4.22}$$

$$X_9 \dot{m}_9 = X_8 \dot{m}_8 \tag{4.23}$$

$$\frac{\dot{m}_8}{\dot{m}_{r,1}} = \frac{X_9}{X_9 - X_8} \tag{4.24}$$

$$\dot{m}_{r,1} = \frac{\dot{m}_{r,1H} \cdot \left(h_{1H} - h_{1,CH}\right)}{\frac{X_9}{X_9 - X_8} \cdot (h_9 - h_8) + (h_1 - h_9)} \tag{4.25}$$

Absorber

Energy and mass balances in the absorber (assumed as adiabatic) are given by

$$Q_a = \dot{m}_{14}h_{14} + \dot{m}_{16}h_{16} + \dot{m}_4h_4 - \dot{m}_5h_5 \tag{4.26}$$

$$\dot{m}_{16} + \dot{m}_{14} = \dot{m}_8 + \dot{m}_{11} - \dot{m}_r \tag{4.27}$$

where $\dot{m}_r$ represents the total refrigerant mass flow

$$\dot{m}_r = \dot{m}_{r,1} + \dot{m}_{r,1H} \tag{4.28}$$

Condenser

The latent heat rejected in the condenser by the vapor produced in the LG is given as

$$Q_{cond} = \dot{m}_{r,1}(h_1 - h_2) \tag{4.29}$$

Sub-cooler

In this component, an energy balance is expressed as

$$Q_{sub} = \dot{m}_{r,1H}\left(h_{1,CH} - h_2\right) \tag{4.30}$$

Evaporator

An energy balance in the evaporator yields

$$Q_e = \dot{m}_r(h_3 - h_4) \tag{4.31}$$

High-temperature solution heat exchanger

The effectiveness of this heat exchanger, which has the purpose of cooling down the concentrated solution leaving the HG, is given by

$$\eta_{Hshx} = \frac{h_{12} - h_{13}}{h_{12} - h_{10}} \tag{4.32}$$

The heat recovered in this component can be calculated as

$$Q_{Hshx} = \dot{m}_{12}(h_{12} - h_{13}) = \dot{m}_{12} \cdot c_{p,s} \cdot (T_{12} - T_{13}) \tag{4.33}$$

As well, it can be expressed as

$$Q_{Hshx} = \dot{m}_{11}(h_{11} - h_{10}) = \dot{m}_{11} \cdot c_{p,s} \cdot (T_{11} - T_{10}) \tag{4.34}$$

Low-temperature solution heat exchanger

Similarly to the high-temperature solution heat exchanger, the effectiveness of this component is given by

$$\eta_{Lshx} = \frac{h_9 - h_{15}}{h_9 - h_7} \tag{4.35}$$

The heat recovered in this component can be calculated as

$$Q_{Lshx} = \dot{m}_9(h_9 - h_{15}) = \dot{m}_9 \cdot c_{p,s} \cdot (T_9 - T_{15}) \tag{4.36}$$

$$Q_{Lshx} = \dot{m}_7(h_8 - h_7) = \dot{m}_7 \cdot c_{p,s} \cdot (T_8 - T_7) \tag{4.37}$$

Split valve

Energy and mass balances in the valve that divides up the solution flow yield

$$\dot{m}_5 = \dot{m}_8 + \dot{m}_{11} \tag{4.38}$$

$$h_6 = h_7 = h_{10} \tag{4.39}$$

Expansion valves

Isenthalpic process is assumed to occur in the expansion devices located at the outlet of both the condenser and the sub-cooler. Thus, it is obtained that

$$h_2 = h_3 \tag{4.40}$$

Throttle valves

In these flow restrictors, it is considered that an isenthalpic pressure reduction takes place. Hence, the following expressions can be written

$$h_{13} = h_{14} \tag{4.41}$$

$$h_{15} = h_{16} \tag{4.42}$$

Solution pump

The pump driving the solution must be able to exceed the pressure drops in all the components, maintaining a constant pressure in both generators. The work performed by the pump is calculated as follows:

$$W_p = \frac{\dot{m}_5 \cdot (P_6 - P_5)}{\rho_5 \cdot \eta_p} \tag{4.43}$$

Coefficient of performance

The thermal coefficient of performance is defined by

$$COP_{th} = \frac{Q_e}{Q_{HG}} \tag{4.44}$$

4.5 Simulation of direct air-cooled double-effect absorption machines

From the above mathematical model and the assumptions exposed below, a computational program was developed in *Matlab* to perform simulations of double-effect direct air-cooled absorption machines. In this case, the model was applied to simulate the prototype's double-effect operation mode. As in the single-effect simulation, the thermodynamic properties corresponding to all the working fluids were obtained according to (Pátek & Klomfar, 2006) and (ASHRAE, 2009).

4.5.1 Assumptions

The assumptions concerning the states of the vapor and the solution are essentially the same as in the single-effect case (section 4.3.1). Table 4.3 shows some specific assumptions made to simulate the double-effect stage of the prototype, based on its design specifications. Similarly to the single-effect simulation, the evaporation temperature is supposed to vary linearly with the ambient temperature. Besides, it is supposed that the solution concentration is equally incremented in both generators, according to optimization performed by (Marcos et al., 2011a).

Table 4.3 Design parameters assumed for the prototype's double-effect operation mode

Parameter	Prototype
T_{cond}	T_{out} + 12
T_a	T_{out} + 8
ε_{shx}	0.8
η_p	0.7

4.5.2 Simulation results

Table 4.4 shows some of the main parameters obtained for the prototype working under the two ambient temperatures specified in section 4.3.2: 36°C and 41°C. From that table, it is noticeable that the prototype's double-effect stage is expected to work with high performances not only in conditions near to the design point (35°C), but also at extreme ambient temperatures. In this sense, simulation results indicate that, at 41°C ,the cooling capacity of the prototype's double-effect stage is just 17% lower than the nominal capacity (7 kW). What is more, it is expected that the prototype can work with COP values around 1.1 at that ambient temperature.

Table 4.4 Main working parameters expected for the prototype's double-effect stage

Working parameter	T_{out} = 36°C	T_{out} = 41°C
Q_e (kW)	6.9	5.8
Q_{HG} (kW)	5.9	5.3
Q_{LG} (kW)	4.0	3.4
Q_{cond} (kW)	3.2	2.7
Q_a (kW)	9.1	8.0
COP_{th}	1.17	1.09
m_{10}/ m_5	0.57	0.57

In Figure 4.3, the thermodynamic cycles for the prototype working in double-effect mode under the aforementioned outdoor conditions are plotted in a Dühring chart. It is seen that the low absorption temperatures allow for high increments of the solution concentration in both generators without risk of crystallization.

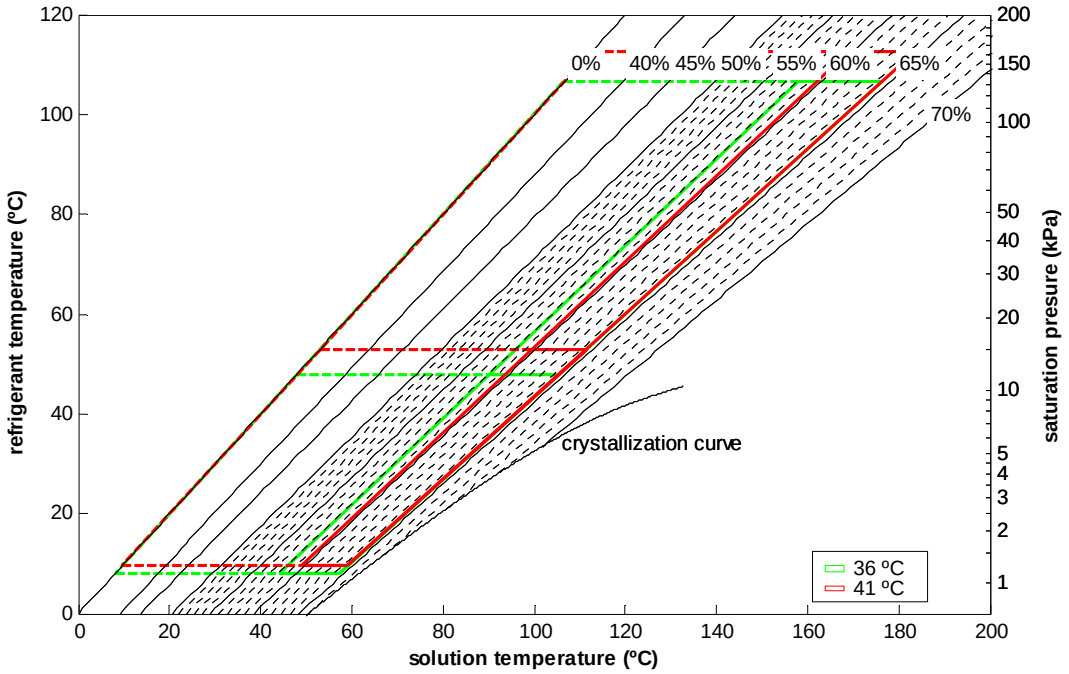

Figure 4.3 Dühring plot expected for the prototype working at 36°C and 41°C in double-effect mode

In Figure 4.4, one can see the simulation results for the COP_{th} of the absorption prototype operating in double-effect mode during the same real day as exposed in section 4.3.2 (13 July 2010), where 38.5°C was the highest outdoor temperature.

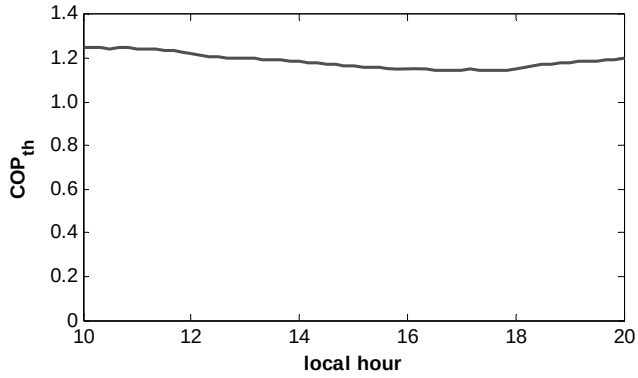

Figure 4.4 Thermal COP of the prototype's double-effect stage on a real day: 13/07/2010

Finally, the obtained results were compared with those reported in (Marcos et al., 2011a) for direct air-cooled double-effect absorption machines and a very good agreement was observed. Note that there is not any direct air-cooled double-effect absorption chiller in the market to establish comparison with real machines.

4.6 Conclusions

In this chapter, two mathematical models were developed to perform quick steady state simulations of direct air-cooled LiBr/H_2O absorption machines working with single- and parallel flow double-effect cycles. When applying these models to simulate the absorption prototype described in Chapter 3, it was found that COP_{th} values of around 1.2 are predicted for the double-effect operation mode. Likewise, the single-effect stage is expected to perform with COP_{th} around 0.7. Furthermore, it was seen that the prototype may perform efficiently at extreme outdoor temperatures without risk of solution crystallization. A comparison between simulation and experimental results for the prototype will be carried out in Chapter 6 and Chapter 7.

Chapter 5

Description and modeling of the prototype's air-cooled adiabatic absorber

5.1 Introduction

In this chapter, the absorber of the single–double-effect prototype will be characterized. Additionally, the development of a new mathematical model for analysis and simulation of air-cooled adiabatic absorbers with flat-fan sheets will be presented. As far as we know, there is not any similar work in the literature describing and simulating this kind of absorbers for LiBr/H_2O air-cooled machines. Furthermore, the chapter includes an optimization of the prototype's absorber design.

5.2 Background of air-cooled adiabatic absorbers with flat-fan sheets

As earlier highlighted, the development of air-cooled absorption chillers is looked as an appropriate alternative for air-conditioning in buildings, especially in low capacity applications. As compared to water-cooled systems, they do not need a cooling tower to remove the heat from condensation and absorption processes, but they use the surrounding air as a free coolant. Consequently, the installation and operational costs are lower and, what is more, health problems such as *Legionella* are avoided. Furthermore, the lack of water consumption makes air-cooled machines very adequate for regions where this

source is a precious commodity. However, in spite of all those advantages, currently in the market one cannot find any air-cooled absorption chiller, as seen in Chapter 2.

On the other hand, $LiBr/H_2O$ solution is regarded as one of the most interesting working fluids for absorption chillers because of its high performance, as pointed out by (Ziegler, 2002) or (Gluesenkamp et al., 2011). However, a relatively high risk of solution crystallization appears when operating at high absorption temperatures, as reported by (Izquierdo et al., 2004) or (Herold et al., 1996). Due to the heat transfer limitations of air as cooling source, air-cooled absorbers normally operate at higher temperatures than water-cooled ones and, as a result, solution is forced to work riskily closer to crystallization limits. Nowadays, this is regarded as the main obstacle for commercialization of air-cooled absorption machines based on $LiBr/H_2O$.

Even though in the literature there are only a few publications about air-cooled absorption machines, one can find some interesting works reporting on possible solutions to overcome the crystallization problem. Some of them are investigations on new salt mixtures that do not crystallize in such working conditions, for instance (Lee et al., 2000), (Kim et al., 1999), (Bourouis et al., 2005) or (Jian et al., 2010). Other reports, like (Medrano et al., 2002) or (Castro et al., 2008) analyzed new configurations for falling film absorbers, traditionally used with water-cooled technology. Alternatively, a new control strategy based on increasing the chilled water temperature was proposed by (Liao & Radermacher, 2007). Lastly, the use of lower driving temperature was proposed as a different option to develop air-cooled $LiBr/H_2O$ absorption chillers, (Kim & Infante-Ferreira, 2009).

In spite of the fact that the above exposed options seem to be adequate to solve the crystallization problems in air-cooled absorption machines, they are either complex to implement or they reduce the performance of $LiBr/H_2O$ cycles. In contrast, the utilization of adiabatic absorbers looks like a valid solution to reduce the risk of crystallization and keep the operation of $LiBr/H_2O$ absorption cycles simple. Unlike traditional falling film absorbers, in an adiabatic absorber heat and mass processes are separated. Absorption of the evaporated refrigerant takes place in an adiabatic chamber and the absorption heat is removed from the solution in a separate heat exchanger. By facing the mass and heat transfer problems separately, a higher improvement of both processes can be achieved. Furthermore, the absorber size may be considerably reduced, as pointed in different publications such as (Wang et al., 2007). Note that an enhancement in the air-cooler heat

transfer coefficient not only leads to a reduction in the heat exchanger size, but also in the absorption chamber.

With the aim of achieving compact absorption chambers in adiabatic absorbers, different configurations for the solution distribution have been proposed. To begin with, some authors like (Ryan, 1993) or (Warnakulasuriya & Worekx, 2008) suggested the atomization of the solution to increase the vapor-solution interface area and therefore enhance the absorption process. However, in (Arzoz et al., 2005) it is concluded that energy consumed in these spray absorbers is relatively high and, besides, the mean mass transfer coefficients are relatively small. Instead, they studied three alternative configurations for the fluid flow without any artificially generated pressure difference: mono-disperse droplets, unstable jets breaking into poli-disperse droplets and films falling along sloping ramps. They proved that the latter configuration is the most adequate. In turn, (Palacios et al., 2009a) reported that conical liquid sheets can considerably scale down the absorber chambers, nevertheless, at the cost of consuming about 5-6 kJ of mechanical energy per kg of vapor absorbed. Lastly, a flat-fan sheet configuration was proposed in (Palacios et al., 2009b). The experimental investigation carried out in that work demonstrated that this configuration performs better than falling film and spray absorbers. Besides, although the rate of vapor absorbed per absorption chamber volume is slightly lower than for conical sheets, the energy demanded is much lower, around 1.5 kJ per kg of vapor absorbed. Similar conclusions concerning the absorption performance of flat-fan sheets can be drawn from a recent theoretical study, (Acosta-Iborra et al., 2009).

To summarize, the use of flat-fan sheet sprayers can be regarded as a very adequate configuration for $LiBr/H_2O$ air-cooled adiabatic absorbers. It enables a reasonably high rate of vapor absorption per chamber volume and, what is more, with a comparatively low demand of mechanical energy.

5.3 Description of the prototype's absorber

Based on the above exposed reasons, an adiabatic absorber with flat-fan sheets was selected for installation in the prototype. Interesting to mention is that the design of this absorber has been developed and patented by the *Energy Saving and Emissions Reduction in Buildings* research group, sponsored by the Eduardo Torroja Institute for Construction Sciences (CSIC), (Izquierdo et al., 2010).

Figure 5.1 shows a schematic of the adiabatic absorber specifically designed for the single–double-effect prototype. As seen, it essentially comprises a reservoir to store the diluted solution, a bank of flat-fan sheet sprayers, a solution gear pump (SP) and an air-cooling system to refrigerate the solution. The concentrated solution coming from the generators reaches the absorber chamber through three different sprayers: one of them is for the single-effect generator and the other two are for the high- and low-pressure generators of the double-effect stage.

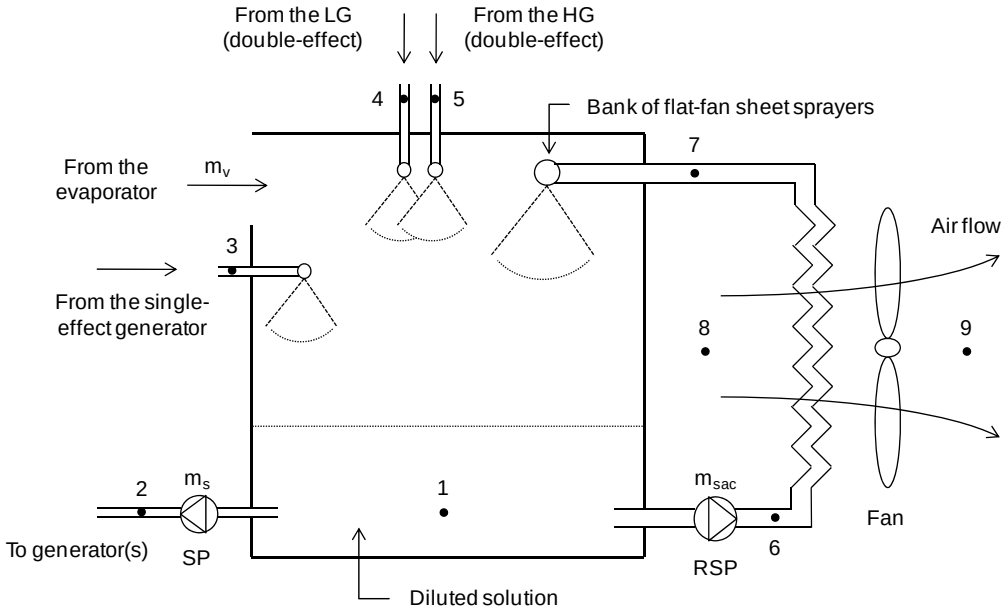

Figure 5.1 Schematic diagram of the prototype's adiabatic absorber

An air-cooling system was assembled to remove the heat resulting from the vapor absorption process. As represented in Figure 5.1, this cooling system is formed by a recirculation solution pump (RSP), a solution air-cooler and a fan. The diluted and warmed solution is pumped by a magnetically driven gear pump through the heat exchanger ($\dot{m}_{sac}$), where it is directly refrigerated by the outdoor air. Once cooled, it returns to the absorber reservoir through a series of flat-fan sheet sprayers, considerably contributing to the absorption of the vapor generated in the evaporator, ($\dot{m}_v$). Finally, part of the solution in the reservoir ($\dot{m}_s$) is pumped again to the generator/s, thus completing the LiBr/H_2O solution cycle. Since the absorption process is favored by low solution temperatures, it is clearly understandable the great relevance of both the solution heat exchangers and the solution air-cooler.

The flat-fan sheets configuration was selected because it represents a significant improvement comparing with other configurations, for instance with spray, droplets or falling film absorbers, as experimentally proved by (Palacios et al., 2009b). Furthermore, in a recent experimental work it was corroborated that liquid sheets also perform better than droplets, (Gutiérrez-Urueta et al., 2011). Due to the fact that liquid sheets develop radially, the solution is forced to move from the refrigerant-poor core of the sheet to its interface, which favors the liquid-gas interface renewal and consequently improves the mass transfer. In addition to that, the flat-fan sheets can be densely packed and therefore a comparatively reduced chamber size can be achieved. In a word, the use of flat-fan sheet sprayers affords adiabatic absorbers greater heat transfer capacity in smaller exchange areas.

As regards to the solution air-cooler integrated in the adiabatic absorber, it is worth mentioning that it is formed by two finned-tube heat exchangers installed in parallel circuits. These circuits were designed to work with identical pressure losses, which implies that the solution mass flow circulating through each of them must be roughly the same; that is $\dot{m}_{sac}/2$.

On the other hand, it is notable that the absorber and the evaporator are assembled together in the same chamber. In this way, the water vapor generated in the evaporator is directly absorbed by the solution in the absorber. The lack of piping between these two components significantly reduces the pressure drop and consequently improves the absorption process.

Regarding the solution mass flow through each injector nozzle, from (Palacios et al., 2009b) it can be drawn that 100 kg/h provides the highest vapor absorption rate with the minimum pressure drop, or what is the same, with the lowest consumption of mechanical energy. Besides, the authors of that paper concluded that 200 mm is an adequate length for the absorption chamber since the absorption process is nearly finished at this point. In this sense, it was reported that around 90% of the sheet absorption capacity is achieved in the first 200 mm.

With the aim of achieving a highly efficient and compact absorber, the above considerations were taking into account at the design stage. Thus, 200 mm was chosen as the distance between the outlet of the sprayers and the free surface of the solution in the reservoir; that is, the sheets length is approximately 200 mm. Likewise, it was decided that a constant mass flow rate of 100 kg/h must circulate by each sprayer. The number of spray-

ers in the absorber chamber and the air flow rate through the solution air-cooler will be determined after the optimization process exposed below.

5.4 Modelling of the prototype's adiabatic absorber

In this section, a mathematical model describing the behavior of the prototype's adiabatic absorber will be developed. It is worth mentioning that, as far as we know, there is not any complete modelization of air-cooled adiabatic absorbers using $LiBr/H_2O$ flat-fan sheets in the current literature.

5.4.1 Absorption process in flat-fan sheets

As above mentioned, in the selected configuration the solution moves into the chamber through a series of injectors that produce expanding flat-fan-shaped liquid sheets. As represented in Figure 5.2, the expansion of the solution stream makes the sheet gradually narrow in the flow direction. Once the solution exits the injector ($r=r_i$), the absorption of the vapor in the chamber starts out and, consequently, the solution is getting warmer and diluted as the sheet develops. At the end of the flat-fan sheet ($r=r_f$), the absorption process finishes. Note that the vapor is in contact with both sides of the liquid sheet.

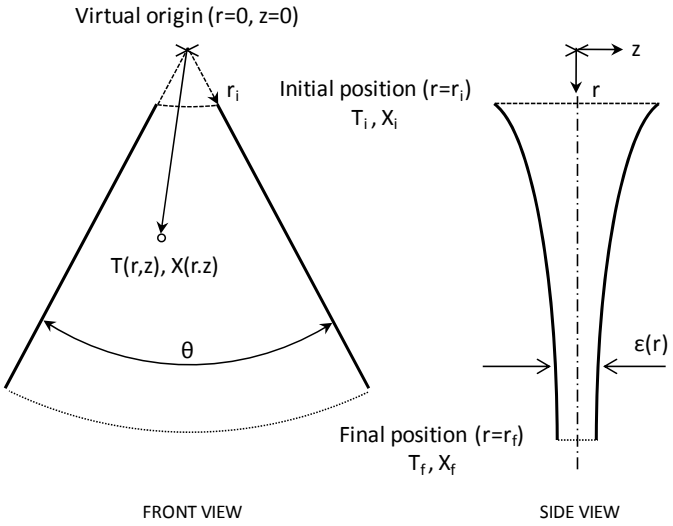

Figure 5.2 Schematic representation of the expanding solution sheet

The absorption capacity of the sheets depends on the mass transfer, which occurs because of the difference between the vapor pressure in the chamber and the partial pres-

sure of water vapor in the solution interface. Once the absorption process starts, the partial pressure of the vapor raises due to the temperature increase and the concentration decrease in the interface of the solution. Hence the great relevance of having an efficient renewal of the liquid-gas interface, such as in flat-fan sheets configuration.

The absorption potential of the $LiBr/H_2O$ solution can be improved either by raising the absorption pressure or by reducing the partial vapor pressure in the solution. Although by increasing the absorption pressure (or the evaporating temperature) a higher COP can be achieved (Liao & Radermacher, 2007), an increase in this parameter implies a higher temperature of the chilled water, which is commonly undesirable in air conditioning applications. What is more, an increase in the absorption pressure limits the refrigerant evaporation and, consequently, may reduce the cooling capacity of the chiller. Reducing the partial pressure of the vapor is regarded then as a better option. To do this there are two possible alternatives: increasing the concentration of the solution while keeping the temperature invariable, (Xie et al., 2008); or lowering the solution temperature with a constant concentration. The second option seems to be the most adequate for adiabatic absorbers since the solution can be efficiently cooled down in the external heat exchanger and crystallization risks are limited.

Finally, it is interesting to mention that the unavoidable presence of non-absorbable gases reduces the absorption potential of the $LiBr/H_2O$ solution, (Kim et al., 1995). Hence the importance of including an effective vacuum system that enables to take out these gases from the chamber before starting up the absorption machine.

5.4.2 Mathematical model of vapor absorption into a single flat-fan sheet

In the literature, one can find a large number of models for simulation of vapor absorption into falling films of aqueous lithium bromide solutions. In contrast, as far as we know, there is only one paper developing a model for flat-fan sheets: (Acosta-Iborra et al., 2009). In this publication, a detailed formulation describing the non-isothermal absorption of vapor into freely expanding liquid sheets is provided, including different liquid flow configurations such as conical, disk and flat-fan. However, an experimental validation of the model was not given in that paper. In spite of this fact, in principle it was assumed as a valid methodology for numerical simulation of vapor absorption into flat-fan sheets and, therefore, it was implemented in the present investigation.

The model developed by (Acosta-Iborra et al., 2009) enables to obtain a wide variety of parameters concerning the coupled heat and mass transfer in a single liquid sheet. For instance, it is possible to estimate the mass fraction at any point of the sheet or the corresponding mass transfer coefficient. Below, a brief description of the fundamentals of the model is given. Special interest was put into describing the main equations that will be used in the modelization of the prototype's absorber.

The absorption model was developed on basis of the coordinate system shown in Figure 5.2. By assuming that the Lewis number, $Le = \alpha/D$, is much greater than one and the sheet mass flow rate keeps practically constant as it develops, a simplified analytical solution for the system of differential equations governing the heat and mass transfer was found by (Acosta-Iborra et al., 2009). The following expression was proposed to obtain the bulk mass fraction of the solution (X_b) at any point in the sheet:

$$\hat{X}_b(\hat{\xi}) = \frac{X_b - X_i}{X_\infty - X_i} = \int_0^1 \hat{X}(\hat{\xi}, \hat{\eta}) \tag{5.1}$$

In Equation (5.1), X_∞ is the concentration that may be reached under complete adiabatic saturation. Besides, $\hat{X}(\hat{\xi}, \hat{\eta})$ represents the normalized mass fraction in the point of the sheet with normalized coordinates $\hat{\xi}$ (radial) and $\hat{\eta}$ (transversal). Interesting to note is that the normalized bulk mass fraction is equivalent to the *Approach to Equilibrium Factor (F)* utilized in different studies about adiabatic absorbers such as (Arzoz et al., 2005), (Palacios et al., 2009a) or (Palacios et al., 2009b).

On the other hand, the rate of vapor absorbed by a LiBr/H_2O sheet with solution mass flow $\dot{m}_{si}$ is calculated with the following expression

$$\frac{\dot{m}_v}{\dot{m}_{si}} = \frac{\delta_3 \hat{X}_b}{1 - \delta_3 \hat{X}_b} \approx \delta_3 \hat{X}_b \tag{5.2}$$

where δ_3 is a dimensionless group representing the normalized subcooling of the solution at the initial position of the sheet, see (Acosta-Iborra et al., 2009).

5.4.3 Simulation of vapor absorption in the prototype's adiabatic absorber

Based on the above model for single LiBr/H_2O flat-fan sheets, in this subsection we will focus on modeling the absorption process in the whole absorber chamber. In this regard, the following considerations are taken into account:

- Steady state conditions.
- At the initial position of the sheet, the temperature and mass fraction are uniform (T_i and X_i, respectively).
- The solution properties are considered invariable under the narrow range of temperatures and concentrations reached during the development of the sheet (ρ, c_p, D, α).
- Heat transfer from the solution to its surroundings and viscous thermal dissipation are neglected.
- Water vapor is the only gaseous substance in the absorption chamber.
- The absorption pressure is assumed to be constant through the entire chamber.
- The bank of sprayers consists of a series of injectors that produce solution flat-fan sheets with identical properties; that is, solution mass flow, sheet length, aperture angle, initial concentration and temperature.
- As a simplification, it is assumed that length of the sheets formed at each generator return is the same as for the sheets in the bank of sprayers, that is 200 mm.

As the absorption capacity of the absorber determines the cooling power of the absorption machine, the first step consists of calculating the maximum amount of water vapor that may be absorbed by the group of flat-fan sheets in the absorber. In this regard, the following nomenclature will be used from now on:

- $(\dot{m}_{v,sheet})_{max}$ is the maximum rate of vapor absorbed into each of the sheets forming the bank of sprayers.
- $(\dot{m}_{v,bank})_{max}$ is the maximum rate of vapor absorbed by all the sheets forming the bank of sprayers.

- $(\dot{m}_{v,g})_{max}$ is the maximum rate of vapor absorbed into the sheet formed at the return of the single-effect generator.
- $(\dot{m}_{v,HG})_{max}$ is the maximum rate of vapor absorbed into the sheet generated at the return of the high-pressure generator (double-effect stage).
- $(\dot{m}_{v,LG})_{max}$ is the maximum rate of vapor absorbed into the sheet generated at the return of the low-pressure generator (double-effect stage).
- $(\dot{m}_{v})_{max}$ is the maximum rate of vapor absorbed by the all the solution sheets present in the absorption chamber; in other words, it represents the absorption capacity of the absorber.

If knowing the conditions of the solution at the initial position of a single sheet, the highest mass fraction at its end may be obtained by using Equation (5.1). Note that this expression must be evaluated at *r=0.2*. Then, by knowing the maximum bulk mass fraction, the highest rate of vapor absorbed by that sheet is determined by Equation (5.2).

According to the above considerations, it is possible to state that all the solution sheets in the bank of sprayers have the same absorption potential. Thus, the following expression can be written

$$(\dot{m}_{v,bank})_{max} = n_{sheet} \cdot (\dot{m}_{v,sheet})_{max} \tag{5.3}$$

where n_{sheet} represents the number of solution sheets in the bank of sprayers.

In the single-effect mode, the maximum rate of absorbed vapor will be given by

$$(\dot{m}_{v})_{max} = (\dot{m}_{v,bank})_{max} + (\dot{m}_{v,g})_{max} \tag{5.4}$$

whereas for the double-effect stage it can be expressed as

$$(\dot{m}_{v})_{max} = (\dot{m}_{v,bank})_{max} + (\dot{m}_{v,HG})_{max} + (\dot{m}_{v,LG})_{max} \tag{5.5}$$

Once the absorption capacity of the absorber is determined, it must be compared with the demanded vapor rate, $\dot{m}_{v,abs}$, which is a function of the cooling requirements of the machine, Q_e. If the value of $\dot{m}_{v,abs}$ is equal or lower than $(\dot{m}_{v})_{max}$, then it can be affirmed that the cooling demand may be met. Naturally, for this it will be necessary that the machine is able to generate the required refrigerant. In turn, if $\dot{m}_{v,abs}$ is higher than

$(\dot{m}_v)_{max}$, it will not be possible to produce the desired cooling effect. In that case, $Q_{e,max}$ will be the maximum cooling capacity of the machine. Note that part of $(\dot{m}_v)_{max}$ is due to the flashing process taking place in the expansion valve and does not yield cooling effect.

When considering the single-effect stage, the amount of vapor absorbed into the sheet of the generator return is given by

$$\dot{m}_{v,g} = \frac{(\dot{m}_{v,g})_{max}}{(\dot{m}_v)_{max}} \cdot \dot{m}_{v,abs} \tag{5.6}$$

In the same way, for the double-effect operation mode it can be written that

$$\dot{m}_{v,HG} = \frac{(\dot{m}_{v,HG})_{max}}{(\dot{m}_v)_{max}} \cdot \dot{m}_{v,abs} \tag{5.7}$$

$$\dot{m}_{v,LG} = \frac{(\dot{m}_{v,LG})_{max}}{(\dot{m}_v)_{max}} \cdot \dot{m}_{v,abs} \tag{5.8}$$

In turn, the vapor absorbed into each single sheet of the bank of sprayers is given by

$$\dot{m}_{v,sheet} = \frac{(\dot{m}_{v,sheet})_{max}}{(\dot{m}_v)_{max}} \cdot \dot{m}_{v,abs} \tag{5.9}$$

In knowing the rate of vapor absorbed by every flat-fan sheet present in the absorber chamber, it is possible to ascertain some interesting parameters at their final positions, namely: solution temperature, solution mass fraction, approach to equilibrium factor or mean mass transfer coefficient.

If taking, for instance, one single sheet of the bank of sprayers, the temperature at its final position can be obtained from the following energy balance.

$$(\dot{m}_v \cdot h_{abs})_{sheet} = \dot{m}_{s,sheet} \cdot c_{p,i} \cdot \left(T_f - T_i\right)_{sheet} \tag{5.10}$$

where $\dot{m}_{s,sheet}$ is the solution mass flow through each injector and h_{abs} is the specific heat of absorption.

According to (Arzoz et al., 2005), the approach to equilibrium factor for a sheet in the bank of sprayers is defined as

$$F_{sheet} = \left(\frac{X_f - X_i}{X_\infty - X_i}\right)_{sheet} \approx \left(\frac{T_f - T_i}{T_\infty - T_i}\right)_{sheet} \tag{5.11}$$

In knowing T_f from Equation (5.10), F_{sheet} is obtained and then, the solution mass fraction at the end of the sheet, X_f, can be calculated by using Equation (5.11).

The mean mass transfer coefficient in the considered sheet, $\overline{h_{m,sheet}}$, is obtained from the following expression, utilized in several studies such as (Arzoz et al., 2005) or (Palacios et al., 2009b):

$$\dot{m}_{v,sheet} = \left(\overline{h_m} \cdot A \cdot \overline{\Delta\rho}\right)_{sheet} \approx \left(\overline{h_m} \cdot A \cdot \rho_i \cdot \Delta X_{lm}\right)_{sheet} \tag{5.12}$$

where ΔX_{lm} is the logarithmic mean mass fraction difference, expressed as

$$\Delta X_{lm} = \frac{\Delta X_i - \Delta X}{\ln\left(\frac{\Delta X_i}{\Delta X}\right)} \tag{5.13}$$

with $\Delta X = X_b - X_{eq}$ defined as the difference between the mass fraction of the bulk and the mass fraction corresponding to equilibrium conditions at the local temperature of the solution. Note that whereas ΔX is evaluated at a given position in the sheet, ΔX_i is calculated at the beginning of the sheet.

In Equation (5.12), A_{sheet} represents the solution sheet surface, which is given by

$$A_{sheet} = \frac{\pi\theta\left(r_f^2 - r_i^2\right)}{180} \tag{5.14}$$

being θ the aperture angle of the sheet. The value of θ depends on the solution mass flow through the nozzle injector and can be taken from (Palacios et al., 2009b).

Lastly, the subcooling of the solution at the beginning of the considered sheet can be calculated from the following expression

$$\Delta T_{\text{sub}} = T_{eq}(X_i) - T_i \tag{5.15}$$

Needless to say that equations from (5.10) to (5.15) are valid to obtain the parameters corresponding to any solution flat-fan sheet in the absorber.

5.4.4 Modeling of the solution air-cooler

As earlier mentioned, the solution air-cooler assembled in the adiabatic absorber consists of two identical finned-tube heat exchangers installed in parallel circuits. Besides, the system incorporates a fan to move the outdoor air through those heat exchangers. More details about the absorber cooler can be found in section 3.2.3.

The equations used to model this air-cooling system are summarized below. To begin with, the overall heat transfer coefficient of a tubular finned heat exchanger is generally expressed as

$$\frac{1}{UA} = \frac{1}{h_i A_i} + R_w + \frac{1}{h_o A_o} \tag{5.16}$$

where the subscripts *i* and *o* refer to the inner and the outer surfaces of the tubes, respectively.

In the above equation, the heat transfer resistance of the tube wall, R_w, can be neglected without introducing a significant error.

The correlation proposed by (Gnielinski, 1976) was utilized to determine the internal heat transfer as a function of the solution mass flow. This is a modification of the Petukhov correlation which extends its application to Reynolds numbers in the transition regime (the applicability range is from Reynolds numbers of 3000 to $5 \cdot 10^6$). It can be written as

$$Nu = \frac{h_i D_i}{k_s} = \frac{(f_s/8)(Re_s - 1000)Pr_s}{1 + 12.7(f_s/8)^{1/2}\left(Pr_s^{2/3} - 1\right)} \tag{5.17}$$

Assuming we have smooth tubes, the friction factor f_s is calculated according to (Petukhov, 1970)

$$f_s = (0.790 \ln Re_s - 1.64)^{-2} \tag{5.18}$$

The *Reynolds* and *Prandtl* numbers of the solution through the heat exchanger are expressed as

$$Re_s = \frac{4\,\dot{m}_{sac}}{\pi D_i \mu_s} \tag{5.19}$$

$$Pr_s = \frac{\nu_s}{\alpha_s} \tag{5.20}$$

On the other hand, the pressure drop in the solution circuit (ΔP_{sac}) is the result of adding the pressure loss in the bank of sprayers and the pressure drop through the pipes of the heat exchanger. Thus, it can be written as

$$\Delta P_{sac} = \Delta P_{bank} + \Delta P_{pipes} \tag{5.21}$$

Considering that the injectors are set up in parallel configuration, the pressure loss in the bank of sprayers is the same as for a single spray. In this sense, from (Palacios et al., 2009b) it is drawn that a pressure loss of 25 kPa is observed for the selected solution mass flow (100 kg/h). In turn, the pressure drop through the pipes of the heat exchanger (ΔP_{pipes}) is obtained from the *Darcy-Weisbach* correlation. Taking into account the influence of valves and pipe elbows in the solution circuit, the following expression is derived

$$\Delta P_{pipes} = f_s \cdot \frac{L_{pipes}}{D_i} \cdot \frac{{u_s}^2}{2g} + \sum K \cdot \frac{{u_s}^2}{2g} \tag{5.22}$$

The energy consumption of the recirculation pump can be obtained by

$$W_{rsp} = \Delta P_{sac} \cdot \frac{\dot{m}_{sac}}{\eta_{rsp} \cdot \rho_s} \tag{5.23}$$

where η_{rsp} refers to the efficiency of the recirculation solution pump. It is taken as 0.5 in the present study.

Regarding the air side of the absorber heat exchangers, the heat transfer coefficient h_o is calculated according to conventional equations taking account of the fins effect, (Incropera & De Witt, 1999). Following the same reference, the pressure drop suffered by the air through the external side of the heat exchanger is given by

$$\Delta P_{air} = G_{air}^2 \frac{v_{air,i}}{2}\left[(1+\sigma^2)\left(\frac{v_{air,o}}{v_{air,i}} - 1\right) + f_{air}\frac{A_o}{A_{ff}}\left(\frac{\left(v_{air,i} + v_{air,2}\right)/2}{v_{air,i}}\right)\right] \tag{5.24}$$

where G_{air} is the air mass velocity, calculated as the mass flow rate over the frontal area of the heat exchanger, A_{fr}; $v_{air,i}$ and $v_{air,o}$ represent the specific volume of the air at the inlet and outlet of the heat exchanger, respectively; and σ is the ratio between the free flow area through the fins (A_{ff}) and the frontal area of the heat exchanger (A_{fr}). The friction fraction

f_{air}, which is dependent upon the Reynolds number of the air flow, is estimated according to (Kays & London, 1984).

An expression analogous to Equation (5.23) gives the energy consumed by the fan

$$W_{fan} = \Delta P_{air} \cdot \frac{\dot{m}_{air}}{\eta_{fan} \cdot \rho_{air}} \tag{5.25}$$

where the fan's efficiency is 0.5. Note that in order to estimate the fan consumption, only the pressure drop corresponding to the absorber heat exchanger is computed. If the operation of the whole prototype were considered, the pressure drop in the condenser should be taken into account as well.

Lastly, the energy consumption associated with the absorber operation (W_a) is the result of adding the consumption of the recirculation pump and the fan.

$$W_a = W_{rsp} + W_{fan} \tag{5.26}$$

5.4.5 Energy balance in the prototype's adiabatic absorber

As above mentioned, the solution air-cooler assembled in the adiabatic absorber is formed by two finned-tube heat exchangers wit the same thermal-hydraulic characteristics. Besides, as the parallel circuits integrating those heat exchangers are designed to present the same pressure losses, it can be assumed that both solution circuits have identical performance. Thus, taking into account the state points indicated in Figure 5.1, the following energy balance can be written for each of the solution-air heat exchangers

$$Q_{ac} = \frac{1}{2}\dot{m}_{sac} \cdot c_{p,s} \cdot (T_6 - T_7) \tag{5.27}$$

with $T_6 \approx T_1$.

In turn, regarding the air side of the heat exchanger the energy balance can be expressed as

$$Q_{ac} = \frac{1}{2}\dot{m}_{air} \cdot c_{p,air} \cdot (T_9 - T_8) \tag{5.28}$$

where T_8 represents the ambient temperature, T_{out}.

If $\dot{m}_{sac}$ and $\dot{m}_{air}$ are defined as operation parameters of the absorption machine and both the outdoor temperature and the solution temperature in the reservoir are known, it is possible to ascertain the heat transfer rate and the outlet temperature of the two fluid flows; that is Q_{ac}, T_7 and T_9. The *effectiveness-NTU* method, in-depth described in (Incropera & De Witt, 1999), was followed to perform those calculations. As well know, this method proceeds by finding out the maximum heat transfer rate that hypothetically could be achieved in a counter-flow heat exchanger of infinite length, Q_{max}, defined as

$$Q_{max} = C_{min}(T_6 - T_9) \tag{5.29}$$

being C_{min} the smallest heat capacity rate between the two fluid flows: solution and cooling air.

Since the effectiveness of the heat exchanger is defined as the ratio between the actual and the maximum heat transfer rates, the following expression can be written

$$Q_{ac} = \varepsilon_{ac} \cdot q_{max} \tag{5.30}$$

Following (Incropera & De Witt, 1999), the effectiveness of the present heat exchangers may be assessed with the equation given below

$$\varepsilon_{ac} = 1 - \exp\left[\left(\frac{1}{C_r}\right)(NTU)^{0.22}\{\exp[-C_r(NTU)^{0.78}] - 1\}\right] \tag{5.31}$$

where $C_r = C_{min}/C_{max}$ and NTU is a dimensionless number representing the number of transfer units, $NTU = (UA)_{ac}/C_{min}$. The value of $(UA)_{ac}$ is obtained from Equation (5.16).

On the other hand, according to the methodology shown in section 5.4.3, the heat transferred to the solution during the vapor absorption process, Q_{abs}, can be expressed as

$$Q_{abs} = \sum_{1}^{n} \dot{m}_v \cdot h_{abs} \tag{5.32}$$

where n represents the number of solution flat-fan sheets in the absorber: bank of sprayers and returns of generators.

Thus, considering the single-effect operation mode, an energy balance in the absorber assembly yields

$$Q_{abs} + (\dot{m}_s - \dot{m}_v)h_3 - \dot{m}_s h_2 - 2Q_{ac} = m_1 c_{p,s} \frac{dT_1}{dt} \tag{5.33}$$

Note that Equation (5.33) allows us to predict how the solution temperature in the absorber's reservoir varies with time.

For the energy balance corresponding to the double-effect stage, the equation is equivalent, just taking account of the solution parameters at the return of both high- and low-pressure generators; that is:

$$Q_{abs} + \left(\dot{m}_{s,HG} - \dot{m}_{v,HG}\right)h_4 + \left(\dot{m}_{s,LG} - \dot{m}_{v,LG}\right)h_5 - \dot{m}_s h_2 - 2Q_{ac} = m_1 c_{p,s} \frac{dT_1}{dt} \tag{5.34}$$

with $\dot{m}_s = \dot{m}_{s,HG} + \dot{m}_{s,LG}$ and $\dot{m}_v = \dot{m}_{v,HG} + \dot{m}_{v,LG}$.

5.5 Optimization of the absorber design

In this section, the above exposed model for adiabatic absorbers will be used to perform an analysis of the proposed absorber design. Assuming a fixed geometry for the solution air heat exchangers (note that it is limited by the final dimensions of the absorption machine), this analysis aims at determining the most adequate number of sprayers in the absorption chamber and specifying the air flow rate through the absorber cooling system.

5.5.1 Fundamentals of the analysis

When varying the number of sheets in the bank of sprayers, the solution mass flow through the solution-air cooler is modified and, consequently, the initial subcooling of the solution changes. Hence, the absorption potential of the sheets also varies. Moreover, the pressure drop in the solution-air cooler circuits is affected by the solution mass flow variations, which influences the energy consumption of the pump. Likewise, changes in the air flow rate modify the heat transfer rates in the solution air-cooler and, therefore, the initial subcooling of the solution sheets. In the same way, the energy consumption of the fan is affected by the air flow rates. On these grounds, an optimization process seems to be necessary to establish the number of sheets in the bank of sprayers and to select the air flow rate through the heat exchangers.

The following considerations will be taken into account for the present optimization of the absorber design:

- The analysis is carried out for an outdoor temperature of 35°C.
- The geometry of the solution air heat exchangers is considered fixed.
- The solution mass flow through each sprayer is kept constant since, as above indicated, 100 kg/h provides the highest vapor absorption rate with the minimum pressure drop.
- The air mass flow through the solution-air heat exchanger is varied from 1 kg/s to 5 kg/s. Note that, as this flow has also influence on the condenser performance, its optimization should consider both devices, the absorber and the condenser. However, this extended study is out of the aims of the present work and, then, only the influence of the air flow rate on the absorber will be taken into account.
- Input parameters for the absorber simulation such as evaporation temperature or solution concentration at the beginning of the sheets are obtained from a previous simulation of the whole absorption machine, see Chapter 4.

5.5.2 Results for the single-effect operation mode

Figure 5.3 shows the variation of the *UA* coefficient in the absorber air-cooler with the number of sheets and the air flow rate. As seen, *UA* is higher when considering more sprayers in the absorber and when increasing the air flow rate. As well known, heat transfer is enhanced with higher flow rates; in this vein, an increase in the solution mass flow improves the inner heat transfer coefficient and, similarly, higher air flow rates enhance the air-side coefficient.

Moreover, it is observed from Figure 5.3 that the influence of the solution flow in *UA* is less marked as the number of sheets grows. In fact, it may be stated that the heat transfer improvement is noticeably less significant when exceeding around 20 sprayers. Likewise, the improvement achieved by varying the air flow rate seems to be less important at higher rates. For instance, whereas a mean enhancement of about 180% is reached by changing the air flow rate from 1 to 3 kg/s, it is just 60% when varying the flow rate from 3 kg/s to 5 kg/s.

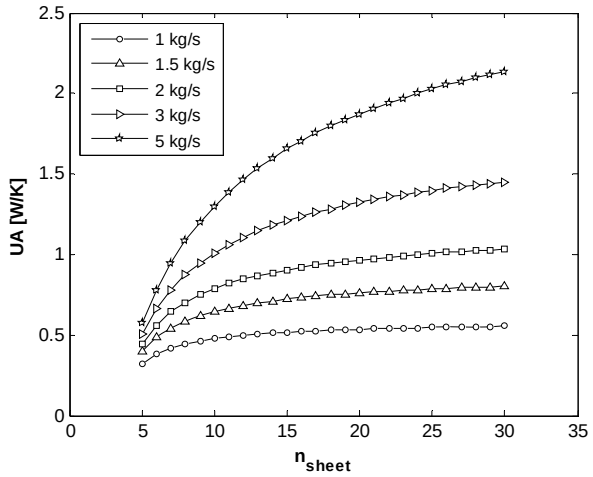

Figure 5.3 Influence of the number of sheets and the air flow rate on the *UA* coefficient

The effect of fluid flows variations on the solution temperature at the exit of the absorber air-cooler is represented in Figure 5.4. It is seen that, even though an increase in the solution flow rate enhances the global heat transfer coefficient, the solution temperature at the exit of the heat exchangers raises with the number of sheets. This fact shows that the effect of having higher solution flow rates is more significant than the heat transfer enhancement. However, this negative effect may be mitigated by increasing the air mass flow rate through the heat exchangers, as will be seen in Figure 5.6.

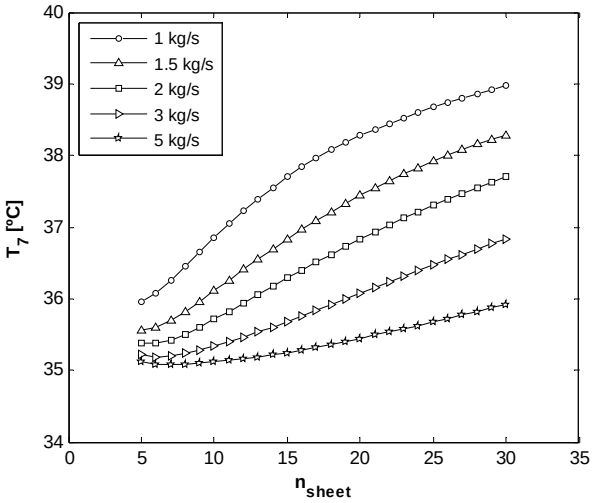

Figure 5.4 Influence of the number of sheets and the air flow rate on the solution temperature at the outlet of the absorber air-cooler

In Figure 5.5, the influence of the studied parameters on the subcooling of the solution at the beginning of the sheets is depicted. Since the subcooling is directly related to

the solution temperature at the outlet of absorber air-cooler, it is clearly understandable that higher air flow rates yield higher subcooling degrees. Likewise, the subcooling is lower when increasing the number of sheets in the absorber because higher solution flow rates are circulating inside the heat exchangers. As in the previous case, the influence of the number of sheets seems to be less significant at higher air flow rates.

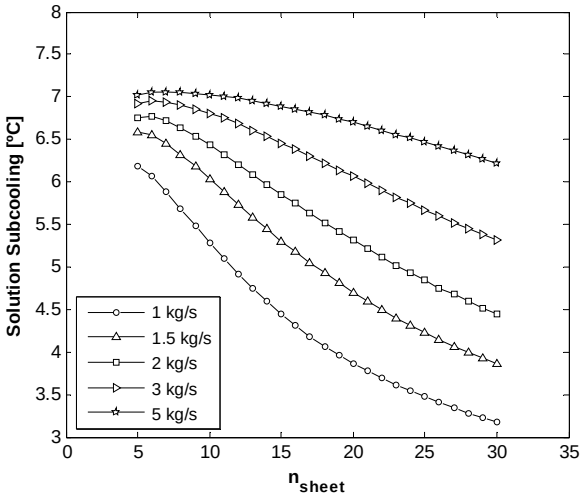

Figure 5.5 Influence of the number of sheets and the air flow rate on the initial subcooling of the solution sheets

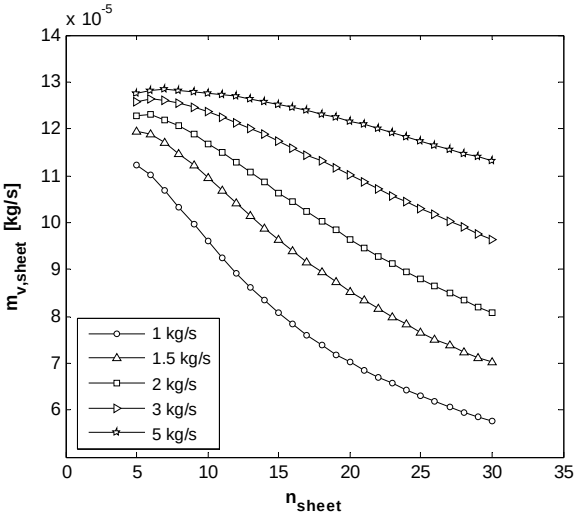

Figure 5.6 Influence of the number of sheets and the air flow rate on the vapor absorption potential of each solution sheet

As earlier mentioned, the subcooling of the solution entering the absorber determines its absorption capacity. In this event, Figure 5.6 shows that the amount of vapor

potentially absorbed by each solution sheet is positively influenced by high subcooling degrees.

In Figure 5.7, it is seen the variation of the absorber capacity as a function of the number of sheets and the air flow rate. First, it is interesting to notice that, although the total absorption capacity of the absorber increases by adding sprayers, the improvement tends to be lower as the number of sprayers is higher. For instance, if taking an air flow rate of 1.5 kg/s and considering 20 sheets, the cooling power of a hypothetical prototype might be 4.3 kW as the maximum. In contrast, by selecting 30 sprayers and the same air flow rate, the maximum capacity of the absorber would be 5.1 kW, which represents an enhancement of just about 20%. Nonetheless, this effect is less marked when considering higher air flow rates.

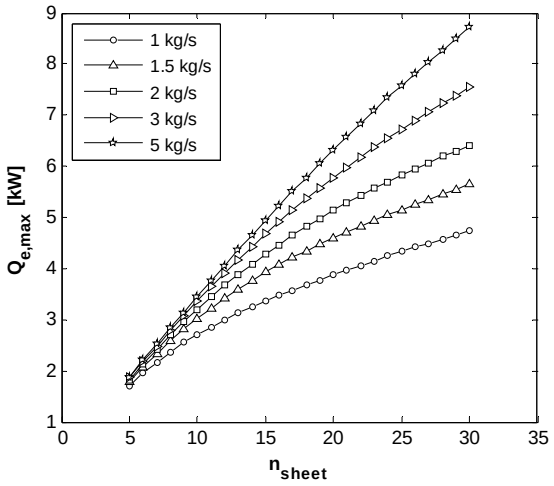

Figure 5.7 Influence of the number of sheets and the air flow rate on the absorber capacity

On the other hand, it is clearly seen in Figure 5.7 that the absorber may improve its capacity by increasing the air flow rate through the external solution-air cooler. However, it is observed that the benefit achieved is less significant at higher rates.

Once analyzed the effect of the number of sheets and the air flow rate on the main working parameters of the absorber, it may result interesting to know how they affect to the energy consumption of both the recirculation solution pump and the fan. In this regard, Figure 5.8 shows how the pump consumption varies with the number of sprayers and Figure 5.9 depicts the effect of the air flow rate on the fan consumption. Furthermore, in Figure 5.10 the total consumption of both devices is plotted as a function of the number of solution sheets and the air flow rate. It is seen that, whereas an increment in the num-

ber of sheets barely affects the total consumption, the air flow rate has a strong influence. This is due to the fact that, while the energy consumed by the pump is directly proportional to the solution mass flow rate, the consumption of the fan is a quadratic function of the air flow rate.

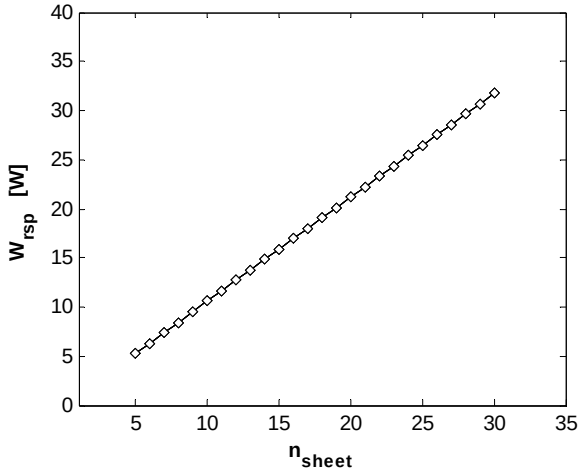

Figure 5.8 Consumption of the recirculation solution pump depending on the number of sheets

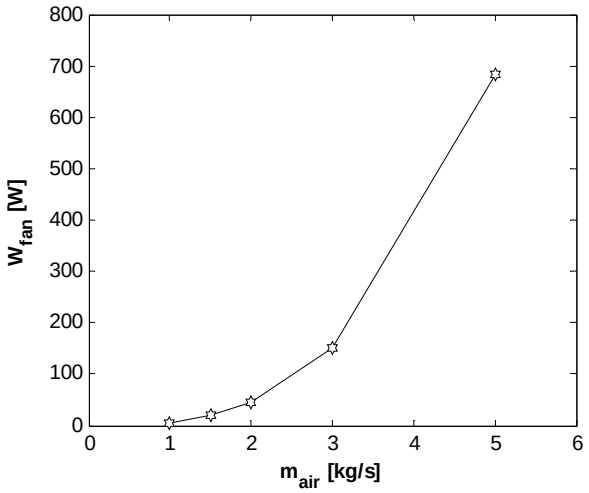

Figure 5.9 Consumption of the fan depending upon the air flow rate

Figure 5.11 shows the ratio between the potential cooling capacity given by the absorber and the associated energy consumption (fan and recirculation pump). As seen, the ratio is considerably lower at higher air flow rates. Besides it is observed that, for intermediate air flow rates (1.5 to 3 kg/s), the ratio grows less significantly when exceeding around 15-20 sheets.

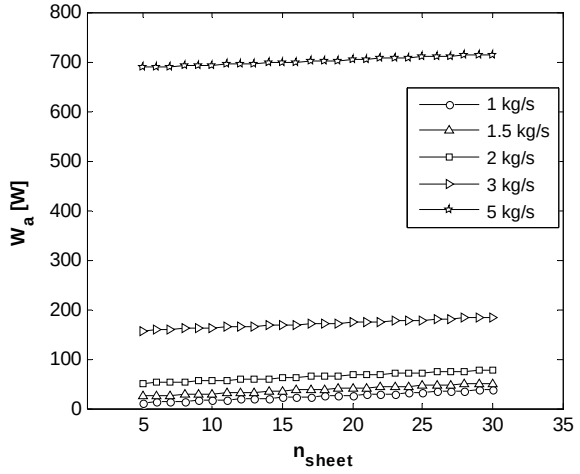

Figure 5.10 Influence of the number of sheets on the power consumption of both the recirculation pump and the fan

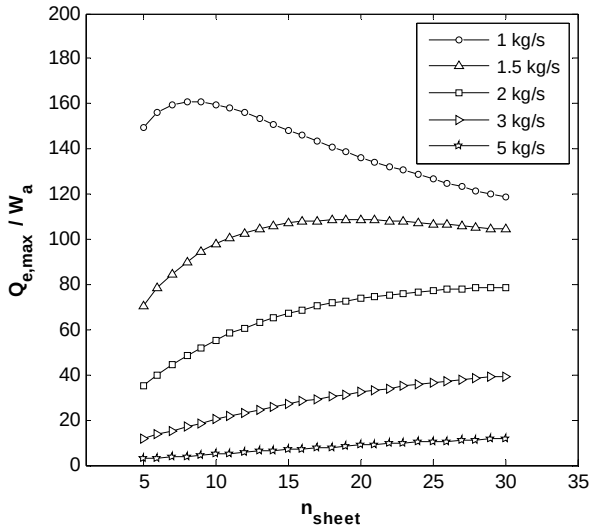

Figure 5.11 Ratio of cooling capacity to energy consumption in the absorber

To summarize, in light of the above results it can be said that both the number of sprayers in the absorber and the air flow rate trough the external heat exchangers have a significant influence on the absorber capacity. In general, higher flows (solution and air) enhance both the heat and mass transfer in the absorber, which improves its cooling capacity. However, higher power consumptions are associated to those enhancements. As a result, a compromise between cooling effect and power consumption must be reached for an efficient design of the absorber. In this vein, it has been shown that with air flow rates between 1.5 kg/s and 2 kg/s and by setting up around 18 sprayers, nominal cooling capacities of about 4.5 kW may be obtained with relatively low power consumption, in single-effect operation mode.

5.5.3 Results for the double-effect operation mode

Considering the double-effect operation mode of the air-cooled adiabatic absorber, an optimization analysis was performed to determine the most appropriate number of sheets in the absorption chamber and the air flow rate through solution air-cooler. This process was analogous to that corresponding to the single-effect mode. It is thought that presentation and discussion of all the obtained results might be redundant, so they were avoided. Nevertheless, it is worth mentioning that with 18 injectors in the bank of sprayers and 2.2 kg/s as air flow rate, around 7 kW of cooling capacity may be achieved with a reasonably low power consumption at ambient temperatures of 35°C, Figure 5.12.

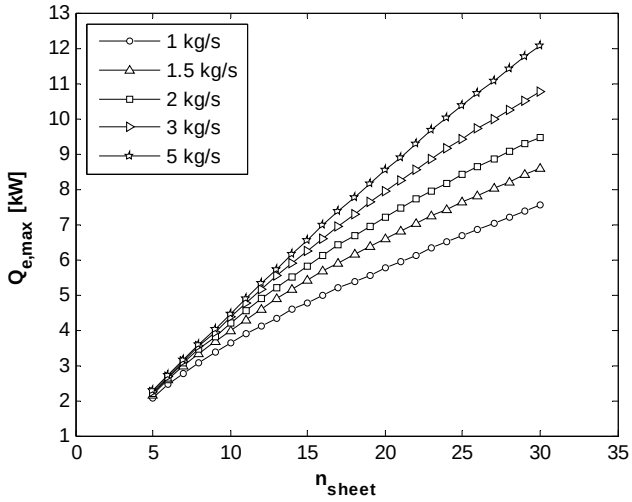

Figure 5.12 Capacity of the absorber in double-effect operation mode

5.5.4 Conclusion of the optimization process

In view of the above results, it can be stated that installing 18 sprayers is a valid option to obtain a good ratio between absorption capacity and energy consumption, for both single- and double-effect operation modes. Regarding the air flow rate through the solution air-cooler, it can be concluded that 1.6 kg/s is an adequate value to efficiently achieve a nominal cooling capacity of 4.5 kW under single-effect operation. In turn, a rate of 2.2 kg/s is needed to obtain 7 kW in the double-effect mode.

5.6 Simulation results for the selected absorber configuration

In order to simulate the behavior of the selected absorber configuration under different working conditions, a computational program was developed in *Matlab* following

the above exposed mathematical model. Below, some of the most relevant results obtained from simulations are exposed and discussed.

5.6.1 Single-effect operation mode

In Table 5.1 one can find some of the numerical outcomes obtained when simulating the single-effect operation mode of the prototype under two different outdoor temperatures, 36°C and 41°C. Notice that variables needed to run the program were taken from the simulation of the whole machine (Chapter 4).

Table 5.1 Main simulation results for the prototype's absorber under single-effect operation

Parameter	T_{out} = 36°C	T_{out} = 41°C
$Q_{e,max}$ (kW)	4.4	3.8
Q_{abs} (kW)	4.9	4.3
T_9 (°C)	38.3	43.3
$\dot{m}_{s,sheet}$ (kg/s)	$2.78 \cdot 10^{-2}$	$2.78 \cdot 10^{-2}$
$T_7 = T_{i,sheet}$ (°C)	37.8	42.8
$\Delta T_{sub,sheet}$ (°C)	5.2	4.6
F_{sheet}	0.937	0.939
$\overline{h_{m,sheet}}$ (m/s)	$3.09 \cdot 10^{-4}$	$3.02 \cdot 10^{-4}$
$\dot{m}_{v,sheet}$ (kg/s)	$9.42 \cdot 10^{-5}$	$8.12 \cdot 10^{-5}$
$T_{f,sheet}$ (°C)	42.7	47.1
$X_{i,sheet}$ (%)	57.0	58.3
$X_{f,sheet}$ (%)	54.4	56.1
$\dot{m}_{s,g}$ (kg/s)	$2.03 \cdot 10^{-2}$	$2.16 \cdot 10^{-2}$
$T_{i,g}$ (°C)	44.2	49.8
$\Delta T_{sub,g}$ (°C)	10.9	10.5
F_g	0.933	0.938
$\overline{h_{m,g}}$ (m/s)	$2.29 \cdot 10^{-4}$	$2.19 \cdot 10^{-4}$
$\dot{m}_{v,g}$ (kg/s)	$1.31 \cdot 10^{-4}$	$1.23 \cdot 10^{-4}$
$T_{f,g}$ (°C)	54.4	59.7
$X_{i,g}$ (%)	63.0	64.5
$X_{f,g}$ (%)	58.0	59.8

Firstly, it is seen that the higher is the outdoor temperature the lower is the cooling capacity of the absorption machine, $Q_{e,max}$. This is because at high ambient temperatures, the solution enters the absorber warmer and, consequently, its absorption potential decreases. Cornering the solution air-cooler, the simulation results showed that it may work quite efficiently, with outlet solution temperatures between 1.5°C and 2°C above the ambient air. This fact enables to reach subcooling rates of about 5°C for the flat-fan sheets in the sprayer bank, which leads to a great absorption potential.

On the other hand, simulation results showed that mean mass transfer coefficients of about $3 \cdot 10^{-4}$ m/s may be obtained for the solution sheets. It is notable that these results are consistent with those experimentally found by (Palacios et al., 2009b). What is more, the values obtained for the approach to equilibrium factor are in excellent agreement with those given in that experimental work, about 0.90 for 200-mm-length sheets. The slightly higher values obtained in this simulation are likely due to the fact that disintegration of the sheet was not considered in the model. Nevertheless, according to (Palacios et al., 2009b), for a solution mass flow of 100 kg/h, disintegration hardly occurs before 200 mm.

Besides, it is interesting to underline the great absorption power of the solution sheet at the return of the generator. In fact, it is able to absorb a rate of vapor higher than sheets in the bank of sprayers. This is due to the excellent performance of the solution heat exchanger, which enables to keep the temperature of the concentrated solution around 40-50°C.

After the vapor absorption process, the solution flowing through the sprayer of the generator return is diluted by approximately 5%, while its temperature increases around 10°C. In turn, the LiBr concentration of the other solution sheets decreases about 2.5%, whereas the temperature rises between 4°C and 5°C. The fact of obtaining a greater increase in the solution temperature for the "generator sheet" is not only due to the higher rate of absorbed vapor, but also to the following reasons: firstly, the solution mass flow rate is lower in the "generator sheet"; secondly, the higher concentration of the solution yields higher specific absorption heat rates.

5.6.2 Double-effect operation mode

In Table 5.2, the simulation results corresponding to the absorber working in double-effect operation mode are shown for two ambient temperatures, 36°C and 41°C.

Table 5.2 Main simulation results for the prototype's absorber under double-effect operation

Parameter	T_{out} = 36°C	T_{out} = 41°C
$Q_{e,max}$ (kW)	6.9	5.8
Q_{abs} (kW)	7.6	6.1
T_9 (°C)	37.8	43.0
$\dot{m}_{s,sheet}$ (kg/s)	$2.78 \cdot 10^{-2}$	$2.78 \cdot 10^{-2}$
$T_7 = T_{i,sheet}$ (°C)	37.7	42.8
$\Delta T_{sub,sheet}$ (°C)	9.1	7.7
F_{sheet}	0.940	0.941
$\overline{h_{m,sheet}}$ (m/s)	$2.99 \cdot 10^{-4}$	$2.87 \cdot 10^{-4}$
$\dot{m}_{v,sheet}$ (kg/s)	$1.60 \cdot 10^{-4}$	$1.36 \cdot 10^{-4}$
$T_{f,sheet}$ (°C)	46.2	50.0
$(X_i - X_f)_{sheet}$ (%)	4.4	3.6
$\dot{m}_{s,HG}$ (kg/s)	$1.43 \cdot 10^{-2}$	$1.62 \cdot 10^{-2}$
$\overline{h_{m,HG}}$ (m/s)	$1.02 \cdot 10^{-4}$	$9.04 \cdot 10^{-5}$
$\dot{m}_{v,HG}$ (kg/s)	$1.36 \cdot 10^{-5}$	$1.09 \cdot 10^{-5}$
$\dot{m}_{s,LG}$ (kg/s)	$1.11 \cdot 10^{-2}$	$1.21 \cdot 10^{-2}$
$\overline{h_{m,LG}}$ (m/s)	$1.64 \cdot 10^{-4}$	$1.52 \cdot 10^{-4}$
$\dot{m}_{v,LG}$ (kg/s)	$3.10 \cdot 10^{-5}$	$2.03 \cdot 10^{-5}$

As for the single-effect stage, it was noticed that the absorption capacity decreases when the outdoor temperature rises. Comparing with the single-effect operation mode, the solution flat-fan sheets of the bank are able to absorb a greater rate of vapor owing to the higher concentration of the solution. In turn, the vapor absorption capacity of the solution sheets at the generator returns is considerably lower because of the higher solution temperatures.

5.7 Validation of the absorber mathematical model

In order to validate the model of the absorber, it is essential to compare the simulation outcomes with experimental results. In this regard, it was decided to run the absorber model with some experimental parameters as input variables, namely: pressure in the

absorber, outdoor air temperature, mass flow rates in the solution air-cooler and solution conditions at the generators returns (temperature, concentration and mass flow rate). The objective is to compare the experimentally measured values with the simulation results for the same input variables.

In Chapter 8 a detailed comparison of experimental and simulation results will be shown. The experimental data used there come from several trials carried out during the testing campaign of the single–double-effect absorption prototype. As will be seen, a very good agreement was found between experimental results and predictions, which enables us to conclude that the proposed model is valid to perform numerical simulations of air-cooled adiabatic absorbers with LiBr/H_2O flat-fan sheets.

5.8 Conclusions

In this chapter, the direct air-cooled adiabatic absorber of the single–double-effect prototype was described and discussed. On the basis of other related studies in the literature, it was concluded that adiabatic absorbers seem to be the best alternative to develop air-cooled LiBr/H_2O absorption machines. Besides, it was drawn that flat-fan sheets configuration is a very adequate option for the solution distribution into the absorption chamber of this kind of absorbers. Regarding the absorber design, some key parameters were detailed and the absorption process taking place was described.

Besides, a mathematical model was developed to simulate that kind of absorbers. Based on that model, a detailed analysis of the absorber design was performed. As a result, it has been concluded that the following configuration is within the optimum range for the absorber operation: 18 injectors producing solution flat-fan sheets; air flow rate of 1.6 kg/s for the single-effect mode; and 2.2 kg/s as air flow rate for the double-effect stage.

Finally, as a remarkable conclusion of the work exposed in this chapter, we have to highlight that the absorber air-cooler allows having such low solution temperatures that the machine can work far from crystallization limits. As far as we know, there is not any absorber with similar characteristics neither in the market nor in the scientific literature.

Chapter 6

Experimental evaluation of the prototype operating in single-effect mode

6.1 Introduction

The absorption prototype was tested in its single-effect operation mode during a summer campaign carried out in 2010. The corresponding results and the experimental procedure will be shown in this chapter. The presented data include detailed operation parameters for two typical summer days in Madrid (5 August and 13 July) and a summary of the results corresponding to the whole campaign. Finally, the experimental results will be compared with predictions obtained from a numerical simulation of the prototype's single-effect stage.

6.2 Experimental setup

The major objective of the experimental campaign carried out in summer 2010 was testing the single-effect operation mode of the earlier described absorption prototype. Therefore, parameters of all components were intended to be determined under different working conditions.

Figure 6.1 shows the block diagram corresponding to the single-effect stage of the prototype, which has a design cooling capacity of 4.5 kW. All the process variables meas-

ured during the single-effect operation of the prototype are shown in that diagram. Details of the single-effect operation mode and the solar facility used to test this stage of the prototype can be found in Chapter 3.

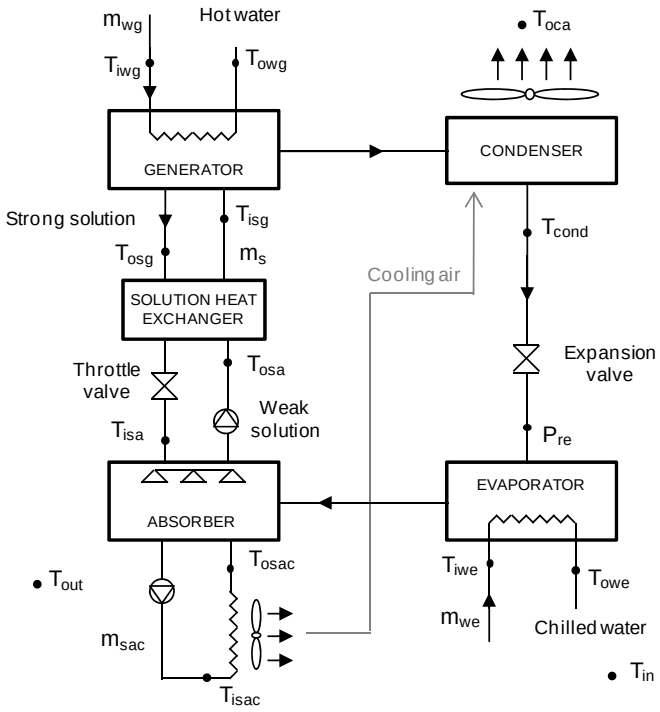

Figure 6.1 Schematic diagram of the single-effect configuration

The measurement system implemented on the facility basically consists of resistance temperature detectors (RTD), flow meters and a vacuum meter, as specified in Table 6.1. For further detail concerning the measuring apparatus, see Appendix B.

Table 6.1 Specification of the different measuring devices

Device	Type	Range	Uncertainty
Thermometer	Pt-100 RTD	-200 to 200°C	±0.1 K
Flow meter	Ultrasonic	100 to 5000 l/h	1-3 %
Vacuum meter	Capacitive absolute pressure sensor	0.1 to 200 mbar	0.2 % f.s.

RTDs were placed at the inlets and the outlets of the following components: generator (T_{iwg}, T_{owg}, T_{isg}, T_{osg}), solution heat exchanger (T_{isg}, T_{osg}, T_{isa}, T_{osa}), evaporator (T_{iwe}, T_{owe}) and solution air-cooler (T_{isac}, T_{osac}); besides, in the condenser, two RTDs measured the refrigerant condensation temperature (T_{cond}) and the cooling-air temperature at the outlet

(T_{oca}), respectively. Ultrasonic flow meters were put in the following circuits: hot water ($\dot{m}_{wg}$), chilled water ($\dot{m}_{we}$), diluted solution ($\dot{m}_s$) and air-cooled solution ($\dot{m}_{sac}$). A vacuum meter was placed inside the evaporator-absorber assembly (P_{re}). The temperature of the air surrounding the prototype (T_{out}) was measured by a RTD located at a distance of 1 m from the floor, in the climatic chamber where the prototype was placed. In the same manner, the indoor temperature corresponding to the air conditioned space (T_{in}) was also registered by a RTD. Lastly, the solar irradiation (I) was registered by a weather station available at the Experimental Plant.

All the measurements were made every 10 seconds and averaged every minute. A computer attached to a data acquisition system was used to register and process all the experimental data.

At this point, it is interesting to say that the utilized measurement interval is considered small enough to not miss relevant information during the prototype evaluation. As it will be shown below, the variations observed in the working parameters are relatively small, mostly without steep changes. In turn, transitory regimes are also observed, mainly during the start-up and the shutdown of the prototype. However, since these transitory periods are relatively large with respect to the total experience time, the selected measurement interval is still regarded as appropriate.

6.3 Experimental procedure

All the single-effect tests carried out during the experimental campaign of summer 2010 were performed by using the solar facility described earlier. That is, the auxiliary circuit of thermal oil was not utilized in any test.

The prototype was operated in such a way that the highest cooling effect could be obtained at every moment. This means that, depending on the input water temperature at the generator, the solution mass flow was regulated so that the prototype deliver the maximum cooling power, obviously avoiding crystallization of LiBr/H_2O solution. Even though all the fluid flows in the prototype might also have been regulated, in this experimental campaign it was decided to keep them constant. In this regard, the nominal chilled water flow was 0.6 m^3/h; the nominal driving water flow, 1 m^3/h; the nominal air-cooled solution flow, 1.2 m^3/h; and the nominal cooling air flow, 5700 m^3/h. It is worth mentioning that this investigation mainly focused on testing the operation of the new prototype.

However, based on the findings of the present work, an optimization process regarding the management of the fluid flows is expected to be performed in the future.

With regards to the initial concentration of the LiBr/H_2O solution, a few preliminary tests were carried out in order to find the most adequate value for the prototype operation. A concentration range between 53% and 57.5% was tested. Although more experiments will be needed to draw a final conclusion, it was seen that 56% appears as the most appropriate concentration value. Actually, when testing more diluted solutions, it was observed that the absorption prototype performed worse. Whereas the coolant production was improved by using lower concentrations, the absorption process was clearly disfavored. Among different regulation problems, this fact implied a higher evaporation pressure. Conversely, at LiBr concentrations higher than 56%, it was noticed that, although the water vapor absorption was excellent, the coolant production rate in the generator was quite low. As known, the more concentrated is the solution, the higher is the temperature needed to make it boil.

6.4 Data reduction

Although some operation variables such as temperatures were directly measured, other important parameters had to be calculated from measurements. In the following, expressions used to obtain heat transfer rates and efficiencies are shown.

To begin with, the total solar radiation on the field of collectors is calculated by

$$R_c = I \cdot A_c \tag{6.1}$$

The heat transferred from the solar collectors to the hot water storage tank is defined by

$$Q_t = \dot{m}_{w,sec} \cdot c_{p,w} \cdot (T_{iwt} - T_{owt}) \tag{6.2}$$

Assuming that there is not heat loss to surroundings, the power delivered to LiBr/H_2O solution in the generator can be obtained as

$$Q_g = \dot{m}_{wg} \cdot c_{p,w} \cdot (T_{iwg} - T_{owg}) \tag{6.3}$$

The cooling capacity of the prototype can be obtained from an energy balance in the evaporator as follows

$$Q_e = \dot{m}_{w,e} \cdot c_{p,w} \cdot (T_{iwe} - T_{owe}) \tag{6.4}$$

Neglecting thermal losses to the surroundings, the following energy balance can be written for the chiller considered as a whole

$$Q_{ca} = Q_a + Q_{cond} = Q_e + Q_g \tag{6.5}$$

where the heat transferred in the absorber cooler (Q_a) can be assessed by Equation (6.6). In knowing Q_{ca} and Q_a, the heat transfer rate in the condenser (Q_{cond}) may be obtained.

$$Q_a = \dot{m}_{sac} \cdot c_{p,s} \cdot (T_{isac} - T_{osac}) \tag{6.6}$$

An evaluation of the cooling effectiveness of the solution heat exchanger is made by using the following simplified equation

$$\varepsilon_{shx} = \frac{T_{osg} - T_{isa}}{T_{osg} - T_{osa}} \tag{6.7}$$

The thermal coefficient of performance of the prototype is obtained as the following ratio

$$COP_{th} = \frac{Q_e}{Q_g} \tag{6.8}$$

If considering the primary energy required to produce the electricity consumed by the pumps and the fan (W_{aux}), the prototype's performance is given by the "Primary Energy Ratio" as follows

$$PER = \frac{Q_e}{Q_g + \frac{W_{aux}}{\eta_{el}}} \tag{6.9}$$

where η_{el} represents the average efficiency of electricity production process. In this work, a value of 0.38 is assumed (MICYT, 2010).

Another parameter commonly used to measure the performance of absorption chillers is the electrical COP, which is defined as the ratio of cooling power to electrical power consumed by the prototype

$$COP_{el} = \frac{Q_e}{W_{aux}} \tag{6.10}$$

The efficiency of the whole system, including the solar facility and the absorption prototype, can be evaluated by using the solar cooling ratio (*SCR*), which is defined as

$$SCR = \frac{Q_e}{R_c} \tag{6.11}$$

The average performance of the absorption prototype, daily or seasonal, is the ratio of the total cooling energy production to the total heat delivered to the generator, as expressed by Equation (6.12). Similarly, daily and seasonal values for *PER* and COP_{el} can be obtained by integrating Equations (6.9) and (6.10), respectively.

$$COP_{d/seas} = \frac{\int Q_e dt}{\int Q_g dt} \tag{6.12}$$

The average solar cooling system performance (daily or seasonal) is the ratio of the total cooling energy production to the total solar radiation on the collector field. It is expressed as

$$SCR_{d/seas} = \frac{\int Q_e dt}{\int R_c dt} \tag{6.13}$$

Lastly, solar fraction (*SF*) gives the percentage of the total cooling demand that is met by the prototype, Equation (6.14). The thermal load of the air conditioned space (Q_{room}) is calculated as mentioned in section 3.3.3.

$$SF_{d/seas} = \frac{\int Q_e dt}{\int Q_{room} dt} \tag{6.14}$$

The thermodynamic properties corresponding to all the working fluids were obtained from (Pátek & Klomfar, 2006) and (ASHRAE, 2009).

6.5 Selection of two representative experiments

The absorption prototype was tested in single-effect operation mode during the summer of 2010. In the following sections, experimental results from tests carried out during two days will be detailed: 5 August and 13 July. The first day can be taken as a typi-

cal clear summer day in the region of Madrid, with maximum ambient temperatures of 35°C. Likewise, it could be regarded as a representative hot summer day in other regions such as the Mediterranean coast. As regards to 13 July, it can be considered as a typical cloudless hot summer day in Madrid, with a maximum temperature of 38.5°C. Contrary to the former day, on 13 July the experiment began before the solar radiation was high enough to power the prototype; that is, the absorption machine was started by using the heat stored in the tank during the previous day.

6.6 Results on a warm day: 5 August 2010

This can be considered as a typical warm summer day in the region of Madrid. As above mentioned, it was clear and the ambient temperature reached 35°C as the highest value. The global horizontal solar radiation was maximum at 14:30 h, reaching 945 W/m^2.

6.6.1 Main results for the solar facility

The most relevant results corresponding to the solar facility used to test the single-effect operation mode of the prototype are summarized below (see description of the solar facility in section 3.3.1).

Figure 6.2 shows the incident solar radiation on the field of collectors (R_c) and the heat power delivered to the solar storage tank (Q_t). Whereas the daily solar insolation on the collectors was 286.49 kWh, the energy transferred to the hot water in the storage tank was 52.13 kWh. The ratio between these two parameters can be regarded as the efficiency of the solar facility, which for the whole day reached a value of 0.18. However, it is notable that this efficiency presented a value of 0.32 about 14:00 h. The spikes observed around 12:00 h and 17:00 h were due to solar facility regulation. As mentioned in section 3.3.1, the pump in the secondary circuit only starts up when water temperature in the primary circuit is 7°C higher than temperature in the storage tank; it stops when the difference between these temperatures are below 2°C. Then, several start/stop processes happened until solar irradiation was high enough to keep the solar facility working continuously (or until the facility was finally stopped).

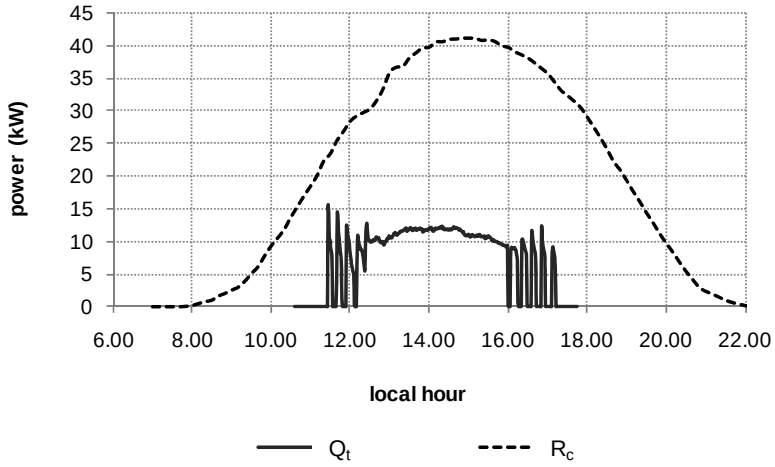

Figure 6.2 Incident solar radiation on the field of collectors and heat power transferred to the storage tank (05/08/2010)

6.6.2 Operation parameters of the prototype

In this subsection, the main working parameters obtained during the operation of the prototype's single-effect stage are presented and discussed. A schematic representation of the single-effect cycle with all the measured variables was given in Figure 6.1.

Generator

To begin with, in Figure 6.3, temperatures corresponding to both sides of the generator are shown. At the beginning of the experiment, at 11:45 h, hot water from the solar facility entered the plate heat exchanger at 97°C, reaching the maximum of 107°C at 16:40 h. Although no more heat was delivered to the storage tank from about 17:20 h, the prototype continued working until 18:40 h, when temperature of hot water was 92°C. On the other hand, LiBr/H_2O solution was heated a mean of 14°C in the generator, ranging the outlet temperature from 80°C to 95°C. Spikes observed around 12:00 h and 17:00 h were mainly due to fluctuations in the driving hot water temperature, which in turn were caused by the aforementioned regulation of secondary circuit. If no heat is transferred to the storage tank, energy consumption in the prototype's generator makes hot water temperature decrease sharply. In turn, start-up of the pump in secondary circuit makes driving water temperature rise again.

In Figure 6.4, the measured values of the solution mass flow through the generator ($\dot{m}_s$) were plotted. Whereas hot water mass flow had a nearly constant value of 0.23 kg/s,

solution mass flow varied from 0.025 kg/s to 0.054 kg/s. Note that, depending on the input water temperature at the generator (T_{iwg}), the solution mass flow was regulated so that the prototype could deliver the maximum cooling power, obviously avoiding crystallization of $LiBr/H_2O$ solution. Thus, in increasing the hot water temperature coming from the storage tank, the solution mass flow was raised. Conversely, when input water temperature went down, the solution flow rates had to be diminished. In order to reduce the observed fluctuations in $\dot{m}_s$, an improved control system could be implemented.

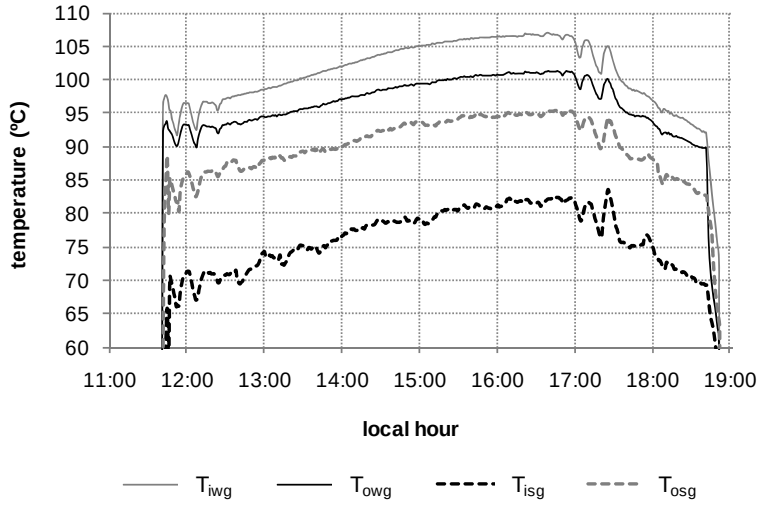

Figure 6.3 Temperatures in the generator (05/08/2010)

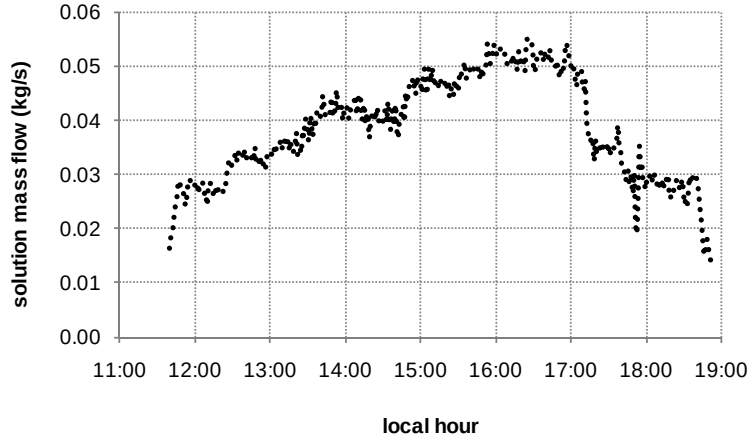

Figure 6.4 Solution mass flow rates (05/08/2010)

Absorber

Figure 6.5 shows the solution temperatures at the inlet and outlet of the absorber (T_{isa}, T_{osa}), as well as the temperature at the outlet of the solution air-cooler (T_{osac}). Outdoor

air temperature (T_{out}) is also represented to establish comparisons. Note that temperatures T_{isac} and T_{osa} are exactly the same: they represent the solution temperature in the absorber's tank. In the following, T_{osa} will be also referred as final absorption temperature.

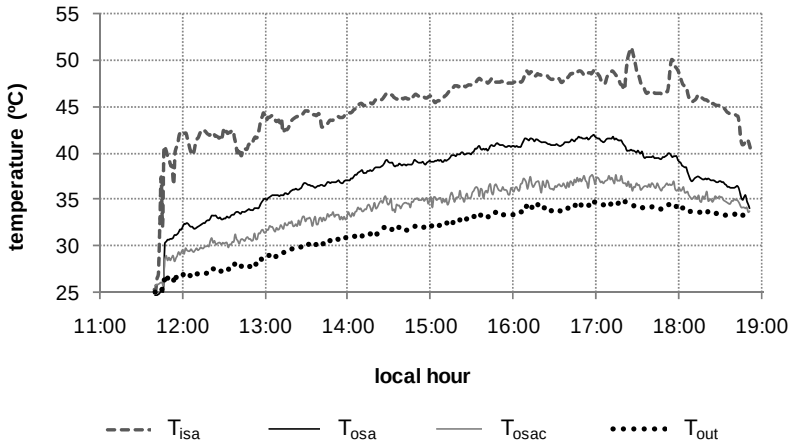

Figure 6.5 Temperatures in the absorber (05/08/2010)

As seen in Figure 6.5, the solution air-cooler was able to reduce the solution temperature about 4-5°C, making absorption temperature not go over 42°C at any time. In other words, the absorber cooler made the final absorption temperature be just 5-7°C higher than ambient temperature. This fact may be regarded as a significant achievement for development of air-cooled LiBr/H_2O absorption chillers, since the absorber is directly refrigerated by the surrounding air, avoiding the secondary cooling water loop present in other air-cooled chiller designs (Izquierdo et al., 2008). Peaks observed in T_{isa} were mainly due to variations in the input water temperature. However, it is interesting to note that two noticeable decreases in the solution mass flow contributed to make peaks between 17:00 h and 18:00 h more pronounced (see Figure 6.4).

Solution Heat Exchanger

As regards to operation of the solution heat exchanger, Figure 6.6 shows both the solution temperature reduction and the heat transfer effectiveness (ε_{shx}). As seen, this plate heat exchanger was able to lower the temperature of solution coming from the generator up to 47°C under steady-state conditions. The effectiveness of the heat transfer process varied between 0.85 and 0.88 during the most of the experiment, being 0.86 the mean value. As known, the solution heat exchanger plays a key role in the absorption process as

it lowers the temperature of the solution flowing to the absorber. For this reason, it is of interest to use an efficient heat exchanger such as PHE.

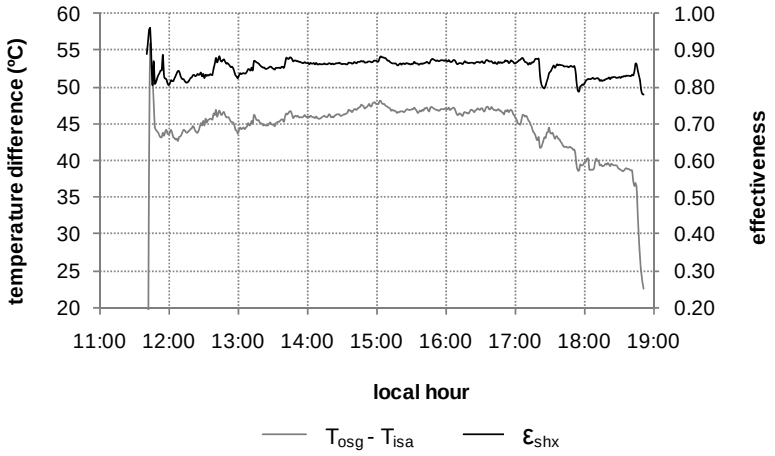

Figure 6.6 Working parameters of the solution heat exchanger (05/08/2010)

Condenser

Figure 6.7 represents the condensation temperature of the refrigerant (T_{cond}) and the cooling air temperature at the condenser outlet (T_{oca}), after passing through the absorber cooler and the condenser. The outdoor air temperature is as well shown. It is interesting to note that the condensation temperature was maintained between 35°C and 47°C during the whole experiment, i.e. about 10-12°C over the outdoor air temperature. If comparing with absorption temperature (Figure 6.5), one can conclude that condensation temperature was about 5°C higher.

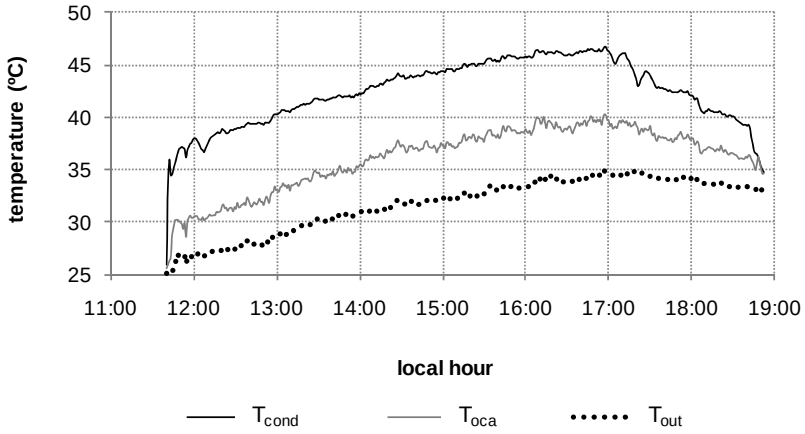

Figure 6.7 Temperatures in the condenser (05/08/2010)

Evaporator

In Figure 6.8, the cooling effect of the prototype is shown. Water temperatures at the inlet and the outlet of the evaporator are represented (T_{iwe}, T_{owe}), as well as the evaporation temperature (T_e). Besides, indoor temperature corresponding to the air conditioned space is plotted (T_{in}). One can see that the prototype was able to keep the indoor temperature between 23°C and 25°C by cooling down the water up to 12.8°C. Evaporation temperature was under 10°C for most of the time, while the minimum difference with respect to chilled water temperature was 5°C.

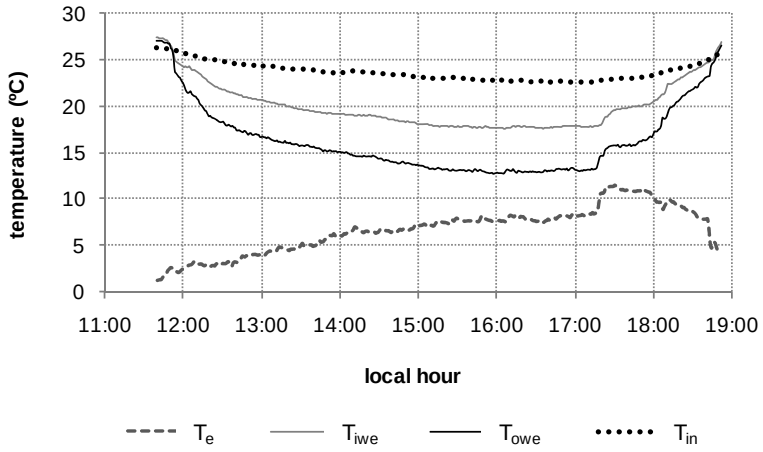

Figure 6.8 Temperatures in the evaporator and the air conditioned space (05/08/2010)

Figure 6.8 also shows that, whereas at the beginning of the experiment the indoor temperature was 26°C, after an hour it was 24°C. Likewise, the chilled water temperature went from 27°C to 17°C in the same period of time. On account of this, the prototype can be considered to have a short start-up time, which is regarded as an important requirement for solar cooling systems. Moreover, it is interesting to note that at the maximum outdoor temperature (35°C at 17:00 h) the water temperature was decreased 4.5°C in the evaporator, reaching 13.3°C. The lowest water temperature was 12.8°C, measured around 16:00 h, when outdoor temperature was 33.5°C. The slight downward slope observed in the chilled water temperature curve is due to the slightly lower increase in the cooling demand than in the prototype's cooling effect. When no more hot was supplied to the storage tank, approximately at 17:20 h, the chilled water temperature sharply increased until the end of the experiment.

Energy balances

Cooling capacity (Q_e) and input power to generator (Q_g) are shown in Figure 6.9. Heat power absorbed by lithium bromide solution went from 2 kW, at the start-up, to about 5.5 kW, when the hot water temperature reached its maximum value. Regarding the measured cooling power, it ranged from 2 kW at start-up to a maximum of 3.7 kW, reached at 16.20 h. From 15:00 h to 17:15 h, when outdoor temperature varied from 32°C to 35°C, the cooling power stayed more or less constant around 3.5 kW, which represents about 78% of the nominal capacity. As above mentioned, the chilled water mass flow rate was kept constant at a value of 0.18 kg/s.

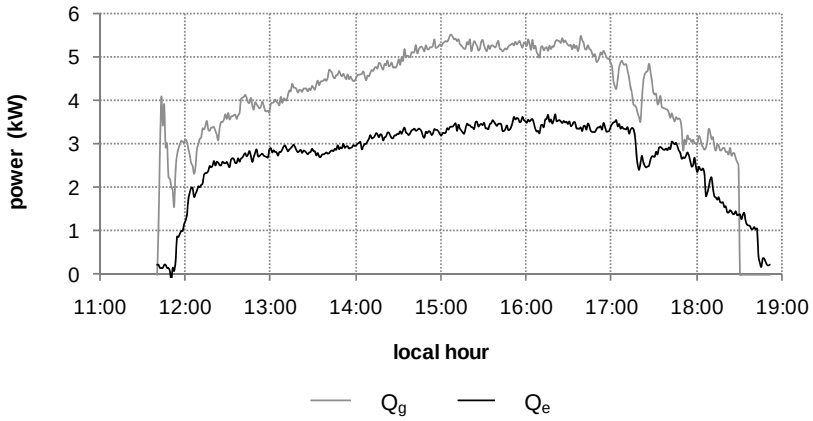

Figure 6.9 Heat power delivered in both the evaporator and the generator (05/08/2010)

Another aspect worth mentioning from Figure 6.9 is the rapid response of the prototype, which was able to deliver cooling power only 10 minutes after the start-up. Moreover, it is notable that refrigeration continued some minutes after cutting off the hot water supply thanks to the inertia of the prototype.

In Figure 6.10, the cooling power of the prototype was depicted together with the thermal load corresponding to the refrigerated space (Q_{room}). As mentioned in section 3.3.3, the room is supposed to be occupied from 9:00 h to 20:00 h, however no need of cooling was observed until 11:00 h. After this point, the thermal load of the room increased constantly up to 3.3 kW, which represented the highest for this day. Afterwards, the cooling load declined gradually up to the laboratory closing time. In contrast, it can be seen that the prototype started delivering cooling power around 12:00 h and stopped before 19:00 h.

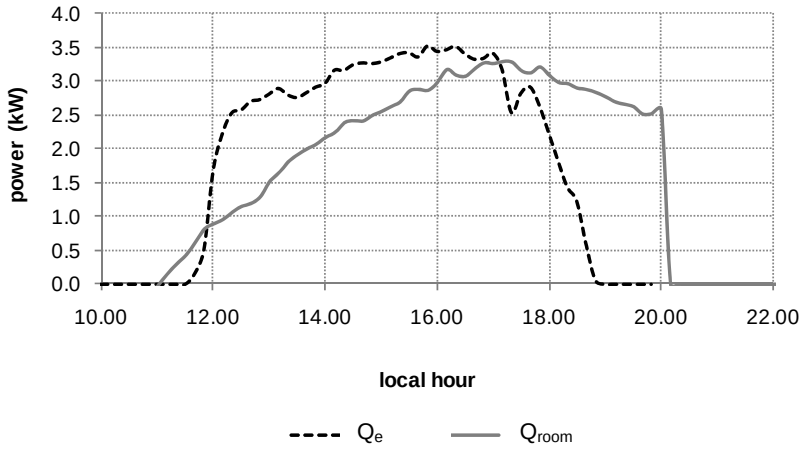

Figure 6.10 Cooling power versus thermal load of the air conditioned space (05/08/2010)

As seen in Figure 6.10, the prototype was nearly able to meet the cooling demand from 12:00 h to 17:00 h. In fact, before 17:00 h the cooling production was higher than the demand. Consequently, the indoor temperature decreased during this period of time (see Figure 6.8). Despite the fact that, according to Equation (6.14) solar fraction for this day was 100%, it is clearly seen that it was not possible to cover the whole cooling demand of the room by using exclusively solar refrigeration. Hence, it was concluded that an additional air conditioning system is needed to meet the cooling demand once the solar radiation is not enough to power the single-effect unit. Another option to overcome that difficulty might be applying fuel fired boilers as back-up heat source for the absorption chiller. However, for an improved utilization of that fuel, we propose to use the double-effect operation mode of the integrated single–double-effect prototype. In this way, the cooling production performance could be about two times higher.

Figure 6.11 shows the total heat removed from the prototype by the air-cooling system (Q_{ca}), as well as the heat transfer rate in the solution air cooler (Q_a). As explained before, the prototype's fan was operated at constant velocity, with a nominal air flow of 1.6 m^3/s. The solution mass flow through the absorber cooler was also kept constant, at a mean value of 0.47 kg/s. In the central part of the experiment, when the highest cooling effect was reached, the heat rejected to the atmosphere was about 9 kW, while the absorption heat ranged between 4 kW and 5 kW.

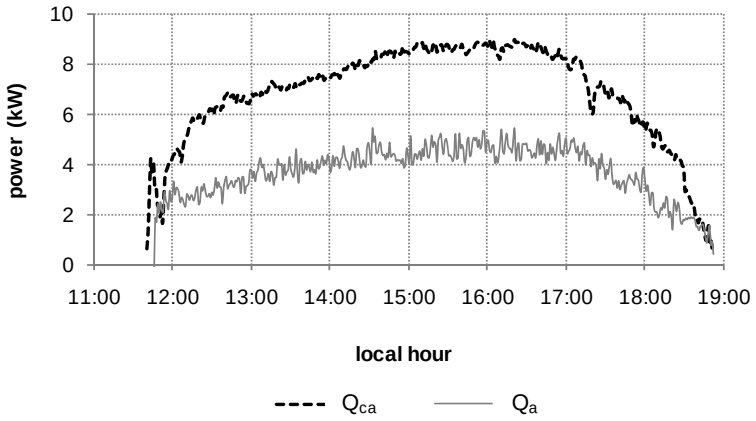

Figure 6.11 Heat power rejected to the atmosphere by the air-cooling system (05/08/2010)

Performance

In Figure 6.12 different prototype's coefficients of performance were plotted. It is seen that thermal COP values were mostly between 0.6 and 0.7. Notwithstanding, in the final part of the experiment the COP_{th} tended to rise, reaching a peak value of 0.9 around 18:00 h. This was due to the fact that, while the input heat power sharply decreased after 17:00 h, the cooling capacity decreased more slowly because of the evaporator's inertia. The spikes observed around 17:00 were mainly caused by the aforementioned flow regulation. The daily thermal COP presented a value of 0.65. Regarding to solar cooling ratio, it ranged between 7% and 10%, which is not far from the values obtained with water-cooled absorption chillers, (Syed et al., 2005).

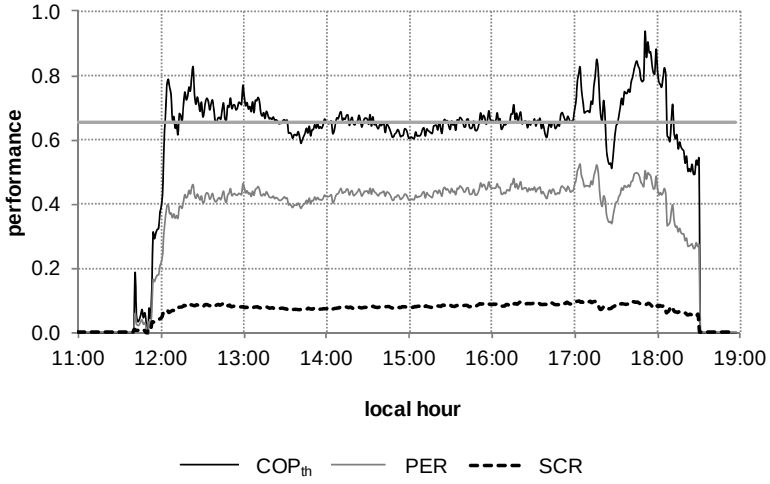

Figure 6.12 Coefficients of performance (05/08/2010)

As far as electricity consumed by the ancillary equipment, measurements yielded a mean value of 930 W. Note that, since all the fluid flows in the prototype except for the solution mass flow were kept constant, the electric consumption stayed practically constant. Taking account of the consumption during the whole experiment, the primary energy ratio (*PER*) was calculated with Equation (6.9) and plotted in Figure 6.12. Its daily value was 0.42.

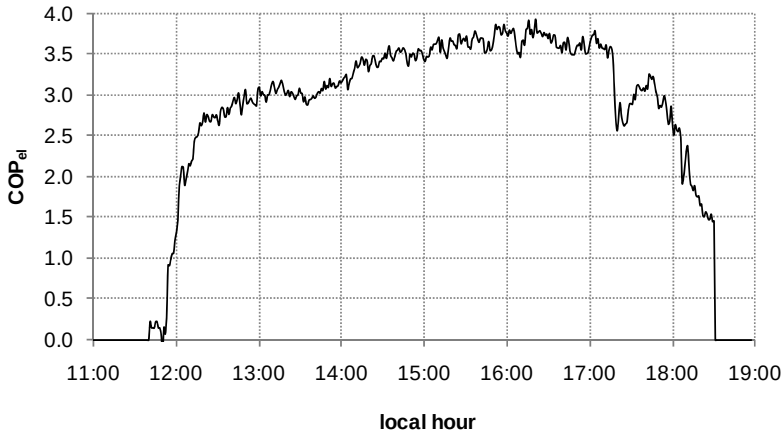

Figure 6.13 Electrical coefficient of performance (05/08/2010)

In Figure 6.13, the electrical COP of the prototype was depicted. As described in section 6.4, COP_{el} represents the ratio of the cooling power over the electrical consumption of the prototype. As seen, during this experiment it mostly ranged between 3.0 and 3.8. It is noteworthy that, at outdoor temperatures about 35°C, the electrical COP presented values around 3.7, which means the prototype is able to perform as efficiently as air-condensed electric compression systems, see for instance (Carrier, 2011). The daily value for COP_{el} was 2.99. Despite these promising results, higher electrical performances could be achieved by carrying out an optimization the prototype. For instance, by focusing on the regulation of the different flow rates in the prototype, the electricity consumption might be cut down and, consequently, the COP_{el} would increase.

Solution cycle

With regards to the cycle described by the $LiBr/H_2O$ solution, Figure 6.14 shows the concentration of both the strong and the weak solution (X_g and X_a, respectively). Besides, the difference between the concentration at the inlet and outlet of the generator was plotted (ΔX). Since equilibrium conditions were assumed in the calculation of the solution con-

centration, only the period with no large fluctuations in the hot water temperature was represented.

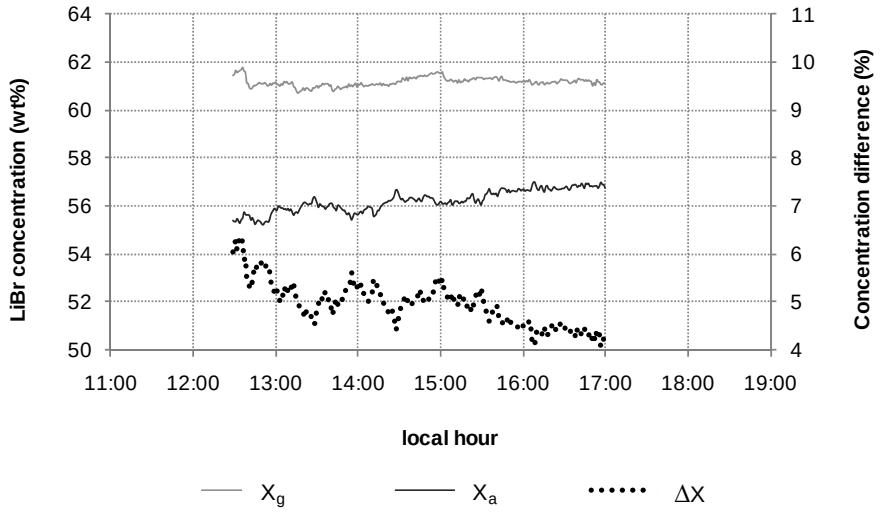

Figure 6.14 Concentration of $LiBr/H_2O$ solution (05/08/2010)

As seen in Figure 6.14, the strong solution concentration was under 62% during the whole experiment and practically constant. In turn, a slight increase was observed in the concentration of the diluted solution, varying from the initial 55.5% up to 57%. This rise was likely due to the increase in the outdoor temperature, which made the solution temperature be higher and higher at the outlet of the absorber air-cooler (T_{osac}). As X_g was maintained more or less constant during the considered lapse of time, ΔX experienced a noticeable decrease, from 6% to 4%.

In Figure 6.15, three absorption cycles at different moments of the experiment were represented in a Dühring chart. As the counterpart, in Table 6.2 some of the cycle properties are indicated. Note that the selected points correspond to instants in which nearly steady conditions were observed. It is seen that when the outdoor temperature rises, the concentration increment suffered by the solution in the generator is lower. In other words, at higher ambient temperatures the plotted cycle narrows. Besides, it can be observed that the higher is the outdoor temperature, the higher are the condensation, the absorption and the evaporation temperatures. However, these increases are not so large, proving the good design of the direct air-cooling system. Lastly, it is interesting to underline that the strong solution concentration is far from crystallization conditions.

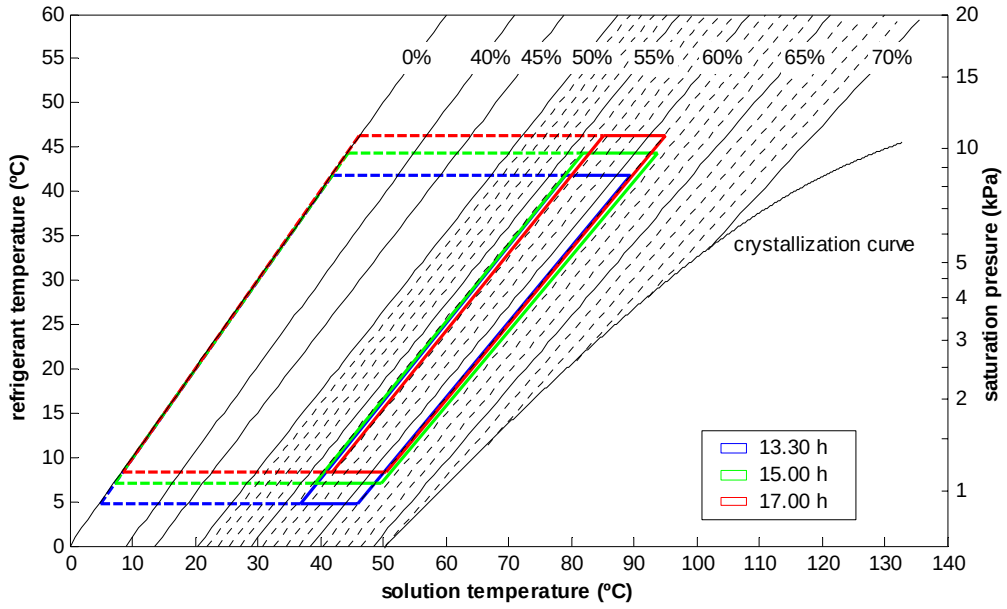

Figure 6.15 Absorption cycles in the Dühring diagram (05/08/2010)

Table 6.2 Properties of the represented absorption cycles (05/08/2010)

Hour	T_{out}	T_a	T_{cond}	T_e	ΔX
13:30	30.3	36.8	41.8	4.8	4.7
15:00	32.2	39.2	44.4	7.1	5.4
17:00	34.7	41.8	46.3	8.4	4.3

6.7 Results on a hot day: 13 July 2010

In this subsection, the experimental results corresponding to a single-effect test carried out on 13 July 2010 are presented. Discussion will be focused on comparing these results, obtained under more adverse weather conditions, with those from the above exposed experiment. Aspects that could be repetitive will be avoided.

This day can be considered as a typical cloudless hot summer day in the region of Madrid, with a maximum temperature of 38.5°C. The highest global horizontal solar radiation was 981 W/m^2, recorded at 15:15 h.

6.7.1 Main results for the solar facility

The most relevant results associated with the solar facility used to run the prototype's single-effect stage on 13 July are summarized below (see description of the solar facility in section 3.3.1).

In Figure 6.16, both the incident solar radiation on the field of collectors (R_c) and the heat power delivered to the solar storage tank (Q_t) are plotted. During the whole day, a total solar radiation of 277.62 kWh was registered on the collectors field, which is a value quite similar to the one of the previously exposed day. In turn, the energy transferred to the hot water storage tank was slightly lower, 51.40 kWh. The daily efficiency of the solar facility resulted to be 0.19, however it is noticeable that at 14:00 it presented an instantaneous value of 0.32. As explained in section 6.6.1, the spikes observed around 12:00 h and 17:00 h were due to the regulation of the secondary circuit in the solar facility.

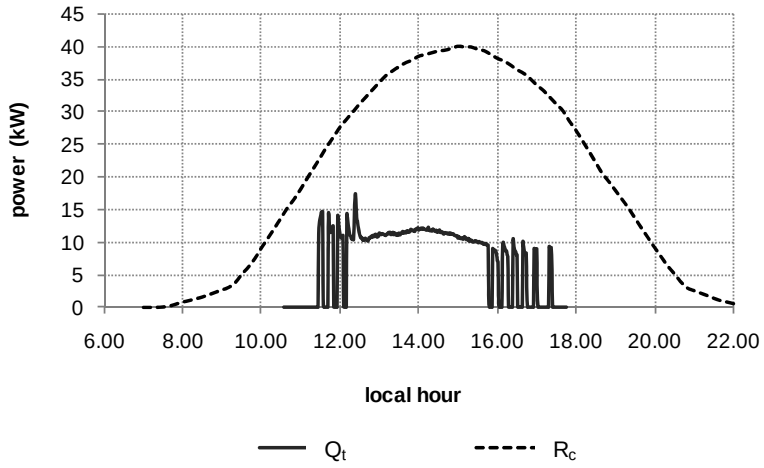

Figure 6.16 Incident solar radiation on the field of collectors and heat power transferred to the storage tank (13/07/2010)

6.7.2 Operation parameters of the prototype

Generator

In Figure 6.17, one can see that this test was started up earlier than previous, around 10:15 h. The initial water temperature was higher, about 105°C, but in just an hour it decreased to 90°C. While during this period of time no heat was transferred to the storage tank (Figure 6.16), the prototype was constantly consuming energy from it. Only when solar intensity was high enough to deliver energy to the storage tank (about 600 W/m^2),

the input water temperature began to increase. The highest input water temperature, 107.7°C, was registered at 16:30 h. Disregarding the start-up, the highest solution temperature at the outlet of the generator was 97°C. This test was finished earlier than previous, at 18:00, when the hot water temperature was about 97°C. Anyhow, in (Izquierdo et al., 2011b) it can be seen that the single-effect stage of the prototype is able to work with driving temperatures up to 85°C.

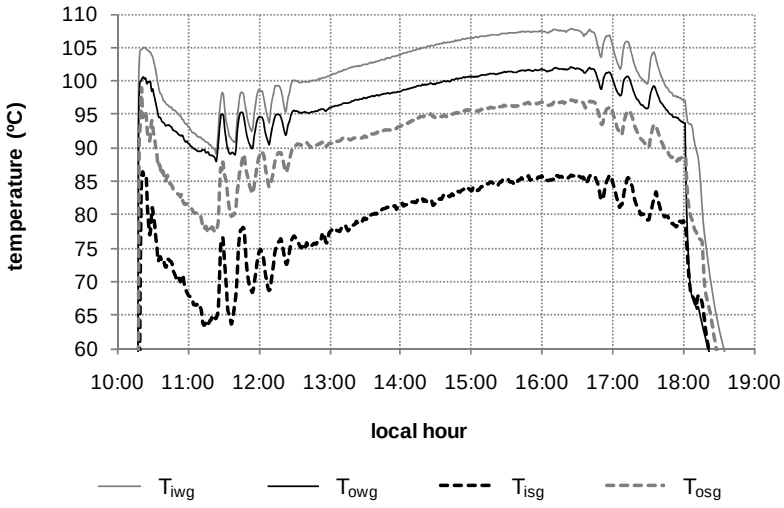

Figure 6.17 Temperatures in the generator (13/07/2010)

Regarding the solution mass flow through the generator, Figure 6.18 shows how it was regulated during the test. As in the former experiment, the flow rate was dependent on the driving water temperature. In fact, as the inlet temperatures were more or less the same in both experiences, the values of $\dot{m}_s$ were quite similar. In this case, for the highest water temperature, 107°C, the solution mass flow increased up to 0.052 kg/s. In turn, the lowest solution mass flow measured was 0.010 kg/s, when input water temperature was about 90°C.

It can be said that the regulation was quite satisfactory in this test. However, for the period of time between 11:00 h and 12:00 h, it turned complex because of the pronounced peaks in the driving water temperature. As stated before, the implementation of a more accurate control system might improve the solution flow regulation.

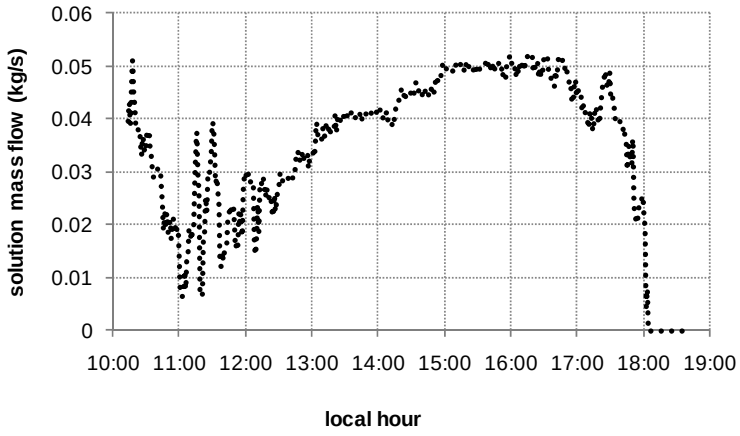

Figure 6.18 Solution mass flow rates (13/07/2010)

Absorber and condenser

Data plotted in Figure 6.19 compare temperatures measured in both the absorber and the condenser with the outdoor temperature. It is seen that final absorption temperature (T_{osa}) reached higher values than in the previous test, since the ambient air temperature was as well higher. Its maximum value was 45.5°C, at 17:00 h, when outdoor temperature was 38.5°C. During the whole experiment, final absorption temperature was kept between 5°C and 8°C above the ambient temperature. Though it is not represented here, it is interesting to mention that a difference of 4-5°C was maintained between the solution temperatures at the inlet and the outlet of the absorber heat exchanger.

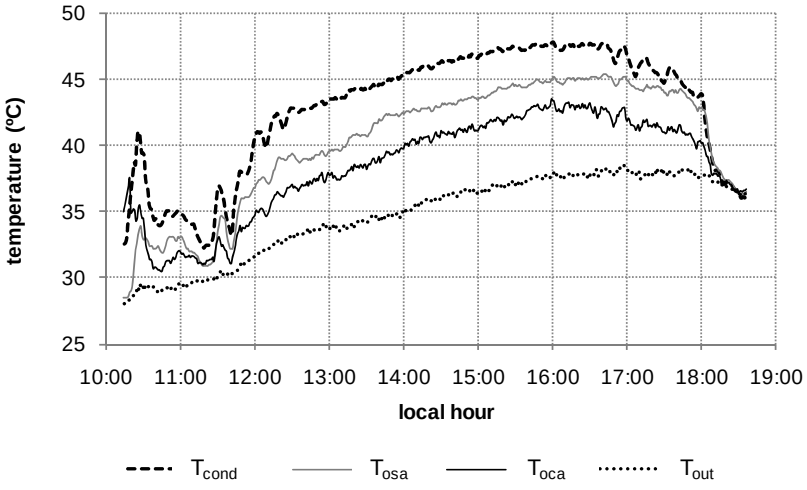

Figure 6.19 Temperatures in the absorber and the condenser (13/07/2010)

On the other hand, in Figure 6.19 it is shown that the condensation temperature reached a maximum value of nearly 48°C, while the air cooling at the outlet of the condenser was 43°C. Again, the condensation temperature was maintained about 9-11°C higher than the ambient air temperature at steady conditions. In spite of the higher temperatures, the air-cooling system for the condenser and the absorber was observed to perform as well as in the previous test.

Solution heat exchanger

As regards to the solution heat exchanger, Figure 6.20 shows that in spite of the more adverse conditions, its working parameters were very similar to those obtained in the previously exposed test. Whereas the mean effectiveness was 0.86, at steady conditions it presented values around 0.88. The solution coming from the generator was cooled down around 45°C during the central part of the experiment.

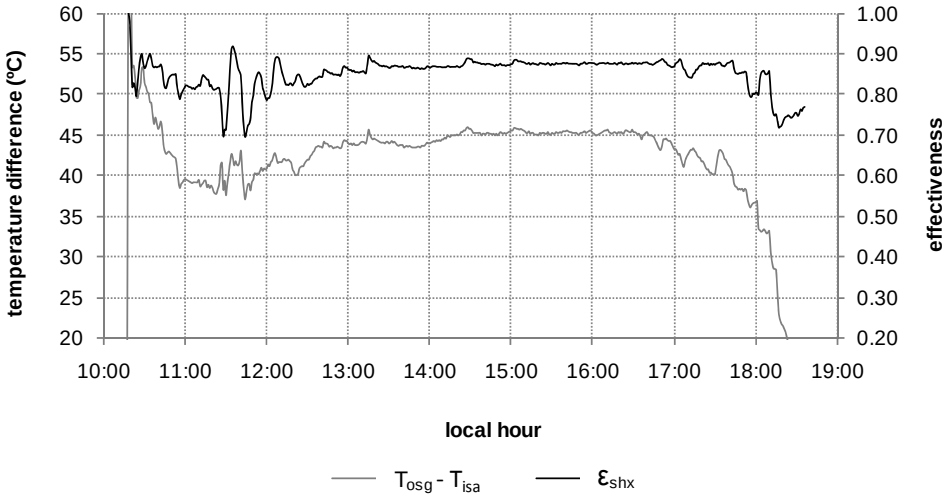

Figure 6.20 Working parameters of the solution heat exchanger (13/07/2010)

Evaporator

Figure 6.21 shows the cooling effect of the prototype. It is interesting to note that it began working properly one hour and a half after the start-up, when the input hot water reached steady conditions. Despite the fact that the input water temperature was high enough at the beginning of the experience, it suffered such a strong decrease that the cooling effect practically disappeared. Then, it can be concluded that, in order to successfully start up the prototype, it is necessary to have a minimum solar radiation that enables to

keep hot water at adequate conditions. This is an important limitation of solar cooling systems that have been emphasized in this experiment.

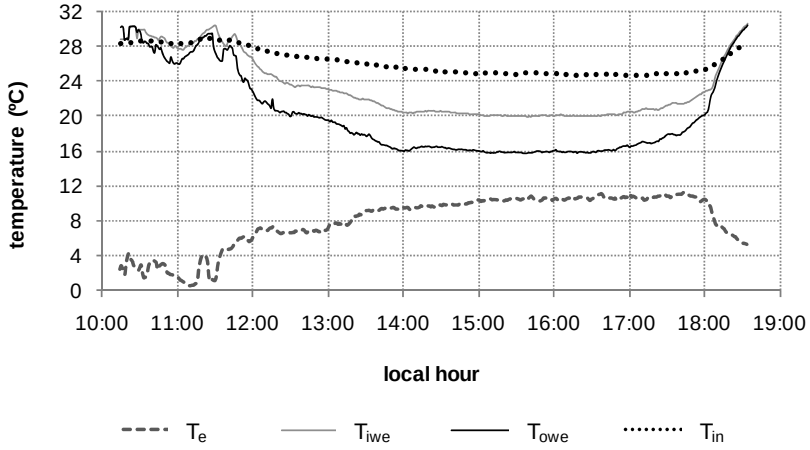

Figure 6.21 Temperatures in the evaporator and the air conditioned space (13/07/2010)

Once the solar radiation reached the aforementioned threshold value (about 600 W/m^2), the indoor temperature in the refrigerated space began to decrease continuously (Figure 6.21). It went from 29°C, at the beginning of the experiment, to 24.5°C at 17:00 h. Note that from 13:30 h to 18:30 h it was under 26°C, which is the highest comfortable temperature recommended by Spanish regulations (MICYT, 2007). Chilled water temperature reached its lowest value at 14:00 h, 15.8°C. For the following three hours, it was kept more or less constant around 16°C. Note that during this period of time, outdoor temperature varied from 34.5°C to 38°C. After 17:00 h, hot water temperature started to decrease and, consequently, the prototype's cooling effect became lower. Evaporation temperature was slightly higher as compared to that one of the previous experiment, mainly because of the higher outdoor temperatures.

Even though the hot water supply was cut off at 18:00 h, measurement system was not turned off at the same time with the purpose of studying the behavior of indoor temperature without any refrigeration equipment. As seen in Figure 6.21, T_{in} suffered a steep rise in just a few minutes. This fact reveals that an additional air conditioning system is needed to meet the cooling demand once the solar system is turned off. In order to overcome this inconvenient, which is regarded as one of the most important barriers to penetration of solar cooling systems in the air conditioning market, we suggest supplying the missing cooling power by firing the double-effect stage of a single–double-effect absorption chiller with any fuel (fossil or renewable).

Energy balances

Data represented in Figure 6.22 are cooling capacity and input power to the prototype's generator. Neglecting the fluctuations at the beginning of the experiment, it can be said that the heat power absorbed by the $LiBr/H_2O$ solution varied between 1 kW and 5.6 kW. Likewise, it can be seen as the prototype yielded a maximum cooling power of 3.6 kW at 14:00 h, when outdoor temperature was 35°C. For approximately the following three hours, the cooling capacity was nearly constant around 3.3 kW, while the ambient air temperature reached 38.5°C. From 17:00 h until the end of the experiment, cooling power went down because of the input power decrease. Like in the previous experience, the cooling effect was produced for a few minutes after cutting off the input energy due to the chiller's inertia.

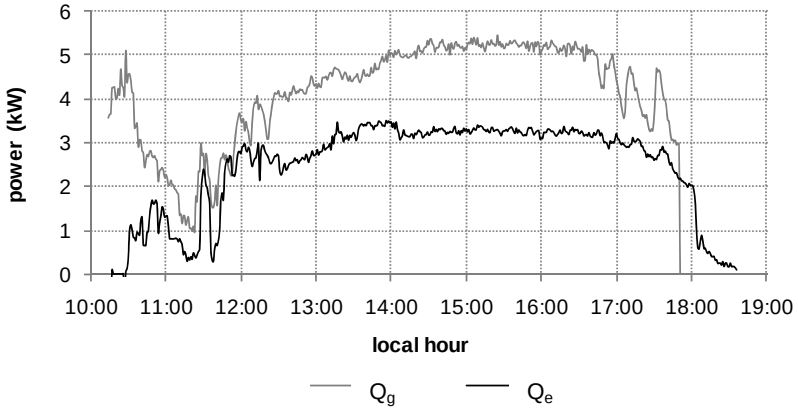

Figure 6.22 Heat power delivered in both the evaporator and the generator (13/07/2010)

Figure 6.23, which compares the thermal load of the air conditioned space with the cooling power delivered by the prototype, corroborates the need of an alternative system for covering the cooling demand once the solar radiation is not enough to power a single-effect absorption machine. According to Equation (6.14), solar fraction for this day was 78%.

As regards to the heat power removed by the air-cooling system, the results were so similar to those ones of the previous test that it was decided not to include them in a new figure. At the highest outdoor temperature, the heat rejected to the atmosphere was about 9 kW, while the absorption heat was 5.5 kW.

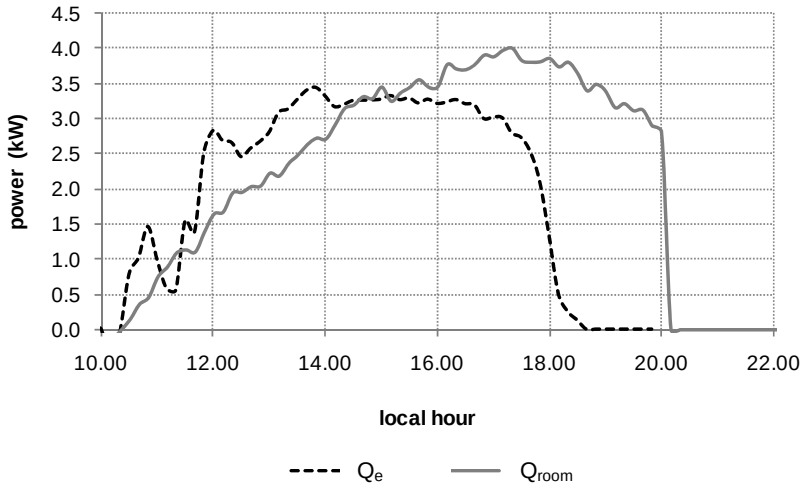

Figure 6.23 Cooling power versus thermal load of the air conditioned space (13/07/2010)

Performance

Figure 6.24 shows that, at steady conditions the COP was around 0.62. Taking no account of the fluctuations at the beginning and the end of the experiment, the highest value for the thermal COP was 0.75, obtained about 13:45 h. The reason of this peak in COP_{th} is that, as seen in Figure 6.22, at that time another peak had been registered in cooling capacity, while the input power kept on increasing constantly. The increase observed in the cooling power was due to manipulation of the expansion valve connecting the condenser and the evaporator. It is interesting to mention here that, in order to get a proper start-up, the expansion valve is normally maintained at its minimum opening. But when no more fluctuations are observed in the operation of the prototype, the expansion valve is turned to its nominal position. Then, the amount of refrigerant that could have been retained in the condenser during that period of time is yielded to the evaporator, consequently increasing the cooling capacity for a while. When all the accumulated coolant left the condenser, the prototype is considered to operate at steady conditions. Although less noticeable, this fact was also observed in the other exposed experiment (Figure 6.9 and Figure 6.12).

The daily COP for this day was 0.64. In turn, taking account of the electricity consumption (940 W as a mean), the daily primary energy ratio resulted to be 0.40. The solar cooling ratio, which was between 8% and 10% during most of the experiment, had a daily value of 7.3%.

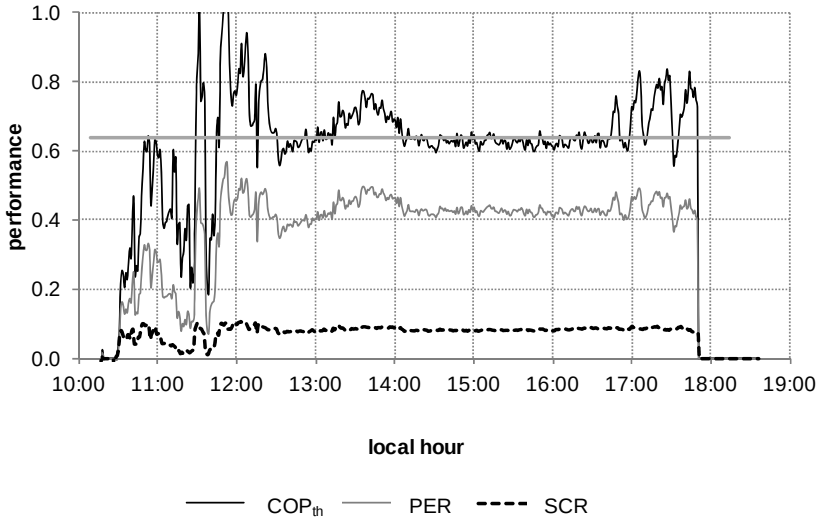

Figure 6.24 Coefficients of performance (13/07/2010)

Regarding the electrical COP, Figure 6.25 shows that it mostly presented values around 3.5, even with outdoor temperatures of 38°C. If comparing with results from the previous test, one can realize that the values obtained on 13 July are slightly lower, due to the higher ambient temperatures. However, when comparing daily COP_{el}, a greater difference appears: whereas on 5 August it was 2.99, in the present test it was 2.74. This is mainly because of the poor production of cold during the first two hours of the present test.

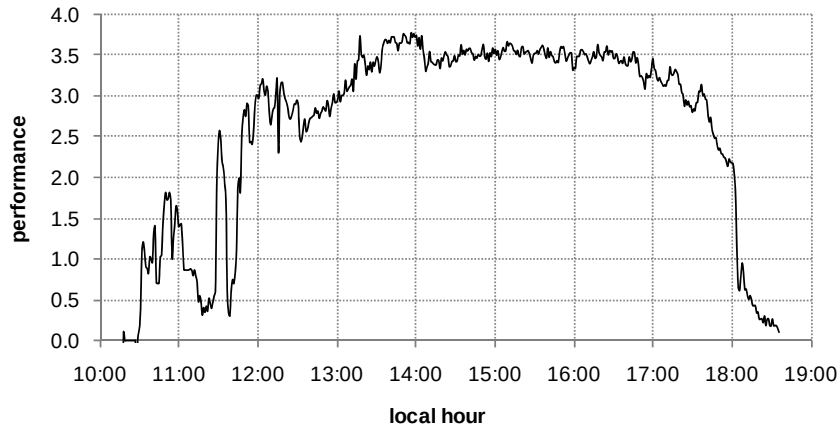

Figure 6.25 Electrical coefficient of performance (13/07/2010)

Solution cycle

Figure 6.26 shows the concentration of both the strong and the weak solution (X_g and X_a, respectively) once the operation of the prototype was more or less stabilized. As

seen, the results are quite similar to those ones obtained on 5 August: the strong solution did not reach 62% during the whole experiment and the difference between diluted and concentrated solution mostly ranged between 4% and 5%.

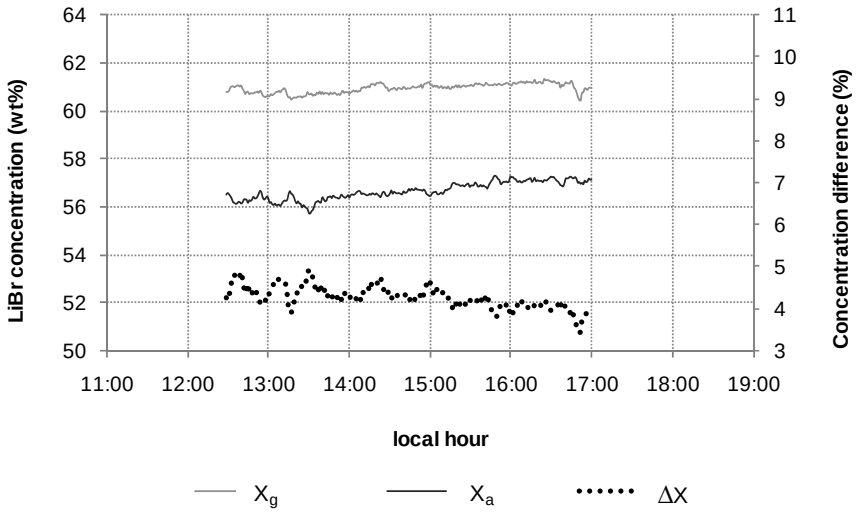

Figure 6.26 Concentration of $LiBr/H_2O$ solution (13/07/2010)

Regarding the thermodynamic cycle described by the solution, in Figure 6.27 three cycles corresponding to different moments in the experiment were plotted in a Dühring chart. Table 6.3 shows some of the thermodynamic properties associated with the represented cycles.

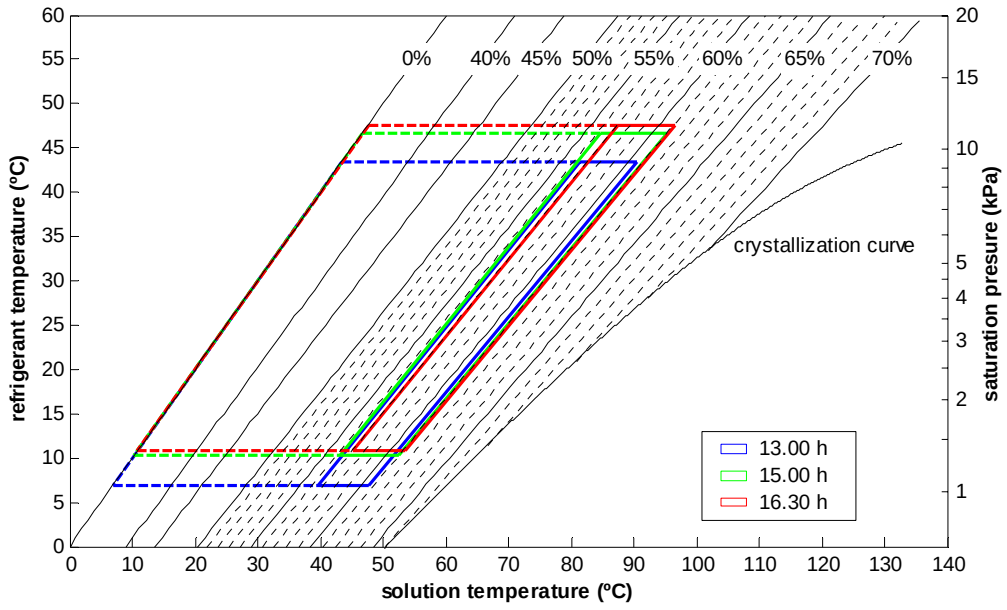

Figure 6.27 Absorption cycles in the Dühring diagram (13/07/2010)

Table 6.3 Properties of the represented absorption cycles (13/07/2010)

Hour	T_{out}	T_a	T_{cond}	T_e	ΔX
13:00	33.8	39.5	43.5	4.9	4.2
15:00	36.4	43.5	46.6	10.3	4.7
16:35	38.2	45.2	47.6	10.8	4.1

It is interesting to underline that, even though the working conditions were more adverse than in the previous test, the strong solution concentration was far from crystallization conditions as well. On account of this, it is believed that the absorption prototype can be operated under much more adverse conditions with no risk of crystallization.

6.8 Results for the overall experimental period: summary

During the experimental campaign carried out in summer 2010, which lasted from May to August, fourteen tests were performed in single-effect operation mode. It consisted of about 100 hours of operation under a wide range of working conditions.

As a summary of the main working parameters measured during the different tests, it can be said that the prototype was driven by hot water at temperatures between 85°C and 110°C; the condensation temperatures varied from 35°C to 50°C; the absorption temperatures were always lower than 46°C; the chilled water temperatures ranged from 12.8°C to 19°C, although they were mostly between 14°C and 16°C; the cooling capacity was between 2 kW and 3.8 kW, being normally about 3-3.5 kW. Furthermore, it is interesting to underline that no crystallization signs were observed during the whole campaign.

In Figure 6.28, the energy balance results and the daily thermal COP corresponding to each day in the experimental period are presented. As the counterpart of the figure, Table 6.4 shows a summary of the energy balance for the whole solar cooling system, including the solar facility and the prototype. In this table, one can find the following parameters for each test and for the entire experimental campaign: duration of the experiment, total amount of solar energy on the collectors field (E_c), energy transferred to the storage tank (E_t), energy delivered in both the generator (E_g) and the evaporator (E_e), daily thermal and electrical COP, primary energy ratio and solar fraction.

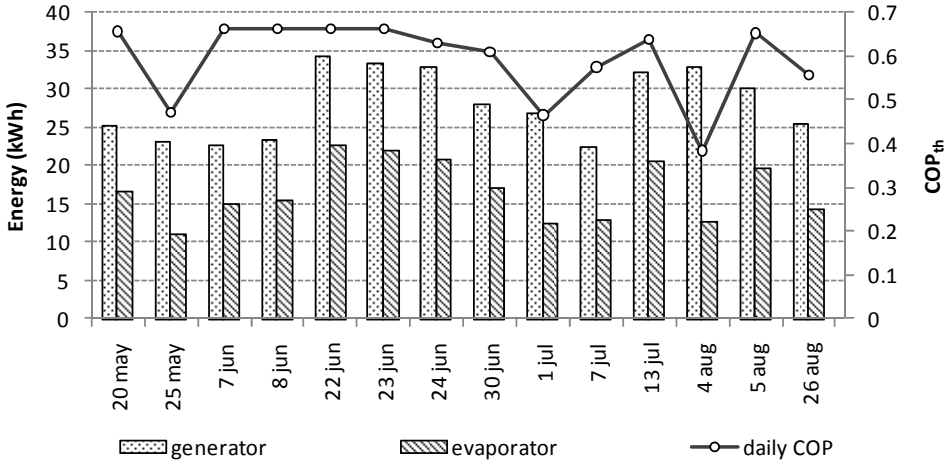

Figure 6.28 Energy balance and daily COP_{th} for the whole single-effect experimental campaign

Table 6.4 Summary of the energy balance for the solar cooling system

Day	Time (h)	E_c (kWh)	E_t (kWh)	E_g (kWh)	E_e (kWh)	COP_{th}	PER	COP_{el}	SF
20 May	6.0	297.29	39.06	25.06	16.42	0.66	0.41	2.94	0.80
25 May	7.0	256.97	30.89	23.07	10.83	0.47	0.27	1.66	0.91
7 June	8.0	268.12	55.85	22.38	14.80	0.66	0.35	1.99	0.64
8 June	7.0	241.99	37.64	23.15	15.29	0.66	0.38	2.35	1.00
22 June	8.0	276.59	54.27	34.12	22.56	0.66	0.42	3.03	0.63
23 June	8.0	275.22	54.47	33.05	21.88	0.66	0.42	2.94	0.72
24 June	8.0	264.69	52.45	32.68	20.55	0.63	0.39	2.76	0.65
30 June	7.0	270.16	50.62	27.72	16.90	0.61	0.38	2.60	0.59
1 July	6.5	252.64	46.45	26.65	12.37	0.46	0.29	2.05	0.49
7 July	8.0	262.63	48.87	22.31	12.80	0.57	0.31	1.72	0.35
13 July	8.0	277.62	51.40	32.02	20.39	0.64	0.40	2.74	0.78
4 August	6.5	276.88	50.60	32.73	12.53	0.38	0.26	2.07	0.53
5 August	7.0	286.49	54.15	29.87	19.47	0.65	0.41	2.99	1.00
26 Aug	7.0	270.42	41.18	25.32	14.06	0.56	0.33	2.16	0.40
Campaign	102.0	3 777.71	667.90	390.13	230.85	0.59	0.36	2.43	0.65

As seen in Table 6.4, there is a significant scatter in the daily results, mostly caused by the different conditions under which the prototype was operated. Notwithstanding, it

must be mentioned that the control system could also contribute to this scatter. In general, it has been observed that the prototype is very sensitive to flow regulation, therefore an investigation to implement a more accurate control is strongly recommended.

When making an energy balance for the whole experimental campaign, the seasonal thermal COP presented a value of 0.59, while the EPR was 0.36. In turn the electrical COP reached a value of 2.43. However, if neglecting the three experiments where the daily thermal COP was under 0.50, the seasonal performances are: COP_{th}= 0.63, EPR=0.38, COP_{el}=2.56.

6.9 Experimental uncertainties

Following information given in section 6.2 about the measurement system and according to (Kline & McClintock, 1953), an experimental uncertainty analysis was performed. An in-depth discussion of the method utilized can be found in Appendix A. The mean results for the main parameters used in this study are presented in Table 6.5.

Table 6.5 Experimental uncertainties in single-effect mode

Operation parameter	Uncertainty
Q_t	± 2.8 %
Q_a	± 5.3 %
Q_g	± 4.0 %
Q_e	± 5.1 %
COP_{th}	± 7.6 %
SCR	± 7.0 %

6.10 Comparison with predicted results

In this section, a comparison is made between the earlier exposed results and the corresponding values from the mathematical model described in Chapter 4.

Table 6.6 shows the predicted and measured values for the main working parameters of the absorption prototype. For each of the above analyzed experiments, it was selected the point with highest outdoor temperature, in the steady range of operation: 34.9°C for 5 August (16:45 h) and 38.3°C for 13 July (16:55 h). It is observed that, in general, experimental results agreed quite well with predicted values. Although the most ac-

curate predictions were made for the operation temperatures (T_e, T_a, T_{cond} and T_{iwg}), the COP_{th} measurements were also very close to the numerical values. Actually, the discrepancies obtained in this parameter were within or near to the mean uncertainty range.

Table 6.6 Comparison of experimental results with predicted values (single-effect)

Working Parameter	5 August (T_{out}=34.9°C)			13 July (T_{out}=38.3°C)		
	Tested	Predicted	Difference (%)	Tested	Predicted	Difference (%)
COP_{th}	0.65	0.72	-9.7	0.63	0.66	-4.5
Q_e (kW)	3.4	4.5	-24.4	3.2	4.0	-20.0
W_{aux} (W)	905	700	29.3	940	750	25.3
T_e (°C)	8.1	8.5	4.7	10.2	9.8	4.1
T_a (°C)	41.8	40.9	2.2	45.3	44.3	2.3
T_{cond} (°C)	46.7	45.9	1.7	47.7	49.3	-3.2
T_{iwg} (°C)	106.5	106.9	-0.4	107.2	113.5	-5.5
ε_{shx}	0.87	0.80	8.7	0.87	0.80	8.7

Conversely, the experimental cooling power was about 20% lower than expected for the selected conditions. This might be due to the fact that the coolant production was slightly lower than predicted, but also due to the underestimation of thermal and pressure loses. After all, as the effectiveness of the solution heat exchanger was higher than expected, the COP_{th} was not so affected by the lower cooling power. Regarding the electricity consumption of the ancillary equipment, it was observed to be between 25% and 30% higher than expected. In this vein, it is interesting to mention that, as the experiments were performed at constant flow, it is though that the electric consumption can be easily reduced to the predicted values by carrying out a flow rate optimization.

6.11 Conclusions

A solar facility with evacuated flat-plate collectors was used to test the single-effect operation mode of the single–double-effect absorption prototype. Fourteen tests were performed under a wide range of working conditions during the summer of 2010. From the experimental results, the following conclusions can be drawn:

The prototype has been working in a quite efficient way, with daily thermal COP values around 0.6 (0.38 if referred to primary energy). In turn, the electrical COP mostly ranged between 3.0 and 3.5. The cooling capacity varied from 2 kW to 3.8 kW, while the chilled water temperature reached a minimum of 12.8°C. Condensation and absorption temperatures were always lower than 50°C and 46°C, respectively, even with outdoor temperatures around 40°C. Driven water temperatures ranged between 85°C and 110°C.

The prototype needed around 92°C to have a successful start-up. Nevertheless, it was observed that when finishing experiments, the prototype could be operated at lower temperatures, normally up to 85°C, with cooling power between 1 kW and 2 kW. This fact seems to be caused by thermal inertia of the prototype, but more experiments are needed to obtain a final conclusion about this issue.

The high effectiveness reached in the solution heat exchanger, around 0.88, played a key role in the performance of the prototype.

After about a hundred hours of operation, no solution crystallization was noticed. This proves the feasibility of direct air-cooled single-effect $LiBr/H_2O$ absorption chillers for solar air conditioning applications, which was one of the main objectives of the present experimental campaign.

Even though the system was able to meet 100% of the daily cooling demand in a few days, 35% of the seasonal cooling demand was not covered. This means that an additional air conditioning system was needed to supply the missing cooling energy. This is a common drawback of solar cooling systems that has to be overcome so that they can compete with conventional refrigeration systems based on electricity. Our proposal is to put single- and double-effect operation modes together in the same absorption chiller. Thus, when solar supply is not enough to run the chiller, it can be operated as a double-effect unit powered by fossil or renewable fuels. In that way, high performances may be obtained.

In spite of the promising results achieved in this work, it is necessary to say that the prototype is not optimized yet. From a comparison between experimental and simulation results, it is drawn that better performances and a higher cooling capacities may be obtained, especially by implementing a more accurate regulation system. Besides, further work must be performed to reduce the electricity consumption of the ancillary equipment.

Chapter 7

Experimental evaluation of the prototype operating in double-effect mode

7.1 Introduction

In this chapter, experimental results of the prototype working as a double-effect absorption machine will be shown and discussed. Likewise, a brief description of the experimental setup will be given. The exposed results were obtained during an experimental campaign carried out in 2010. Firstly, operation parameters corresponding to one of the tests will be presented and analyzed in detail. Following, a summary of the whole experimental period will be given. Finally, experimental results will be compared with predictions from a numerical simulation of the prototype's double-effect stage.

7.2 Experimental setup

In Figure 7.1 one can see the block diagram corresponding to the double-effect stage of the prototype, which has a design cooling capacity of 7 kW (see Chapter 3 for further details on this configuration). Likewise, Figure 7.1 schematically shows all the process variables measured during the testing of the prototype's double-effect operation mode.

The measurement system implemented on the prototype essentially consists of resistance temperature detectors (RTD), flow meters and a vacuum meter, as detailed in Table 6.1. Further information about the measuring apparatus can be found in Appendix B.

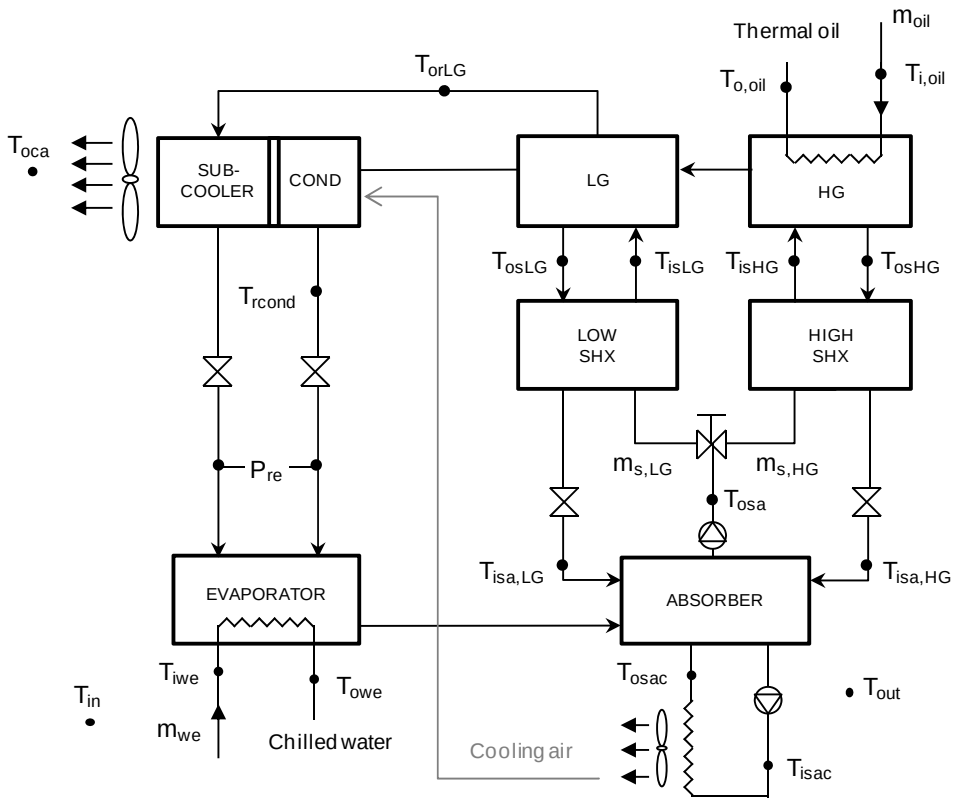

Figure 7.1 Schematic diagram of the double-effect configuration

Similarly to the single-effect configuration, RTDs were placed at the inlets and the outlets of the main components of the prototype. Thus, we have the following temperature measurements: $T_{i,oil}$ and $T_{o,oil}$ for the thermal oil at the inlet and the outlet of the high-pressure generator, respectively; T_{isHG}, T_{osHG}, $T_{isa,HG}$ and T_{osa} for the solution entering and leaving the high-solution heat exchanger; T_{isLG}, T_{osLG}, $T_{isa,\mathrm{LG}}$ and T_{osa} for the solution at the inlets and outlets of the low-solution heat exchanger (note that T_{osa} is the same for both SHXs since this is the solution temperature at the outlet of the absorber); T_{isac} and T_{osac} for the solution entering and leaving the air-cooler of the adiabatic absorber; T_{iwe} and T_{owe} for the chilled water at the inlet and the outlet of the evaporator; T_{rcond} for the refrigerant condensation temperature in the condenser; T_{oca} for the cooling air after passing through the absorber, the condenser and the subcooler; T_{orLG} for the refrigerant at the subcooler inlet; T_{out} for the air surrounding the prototype; T_{in} for the indoor temperature in the air conditioned space.

On the other hand, ultrasonic flow meters were used to register the following mass flows: thermal oil ($\dot{m}_{oil}$), chilled water ($\dot{m}_{we}$), diluted solution flowing through the high- and low-pressure generators ($\dot{m}_{s,HG}$ and $\dot{m}_{s,LG,}$ respectively) and air-cooled solution ($\dot{m}_{sac}$). Lastly, a vacuum meter was placed inside the evaporator-absorber assembly (P_{re}).

All the measurements were made every 10 seconds and averaged every minute. A computer attached to a data acquisition system was used to register and process all the experimental data. As justified for the single-effect tests, the utilized measurement interval is considered small enough to not miss relevant information during the prototype evaluation.

7.3 Experimental procedure

The double-effect stage of prototype was operated in such a way that the highest COP and cooling capacity could be obtained at every moment, obviously avoiding crystallization of LiBr/H_2O solution.

Depending on T_{out}, the temperature of the driving oil was adjusted by varying the input power to the thermal oil tank. Likewise, the solution mass flow through the generators was regulated as a function of the oil temperature with the aim of achieving the highest cooling capacity. Despite the fact that all the other fluid flows in the prototype could also have been regulated, in this experimental campaign it was decided to maintain them constant. In this regard, the nominal chilled water flow was 0.6 m^3/h; the nominal thermal oil flow rate was 2.5 m^3/h; the nominal air-cooled solution flow rate was 1.2 m^3/h; and the nominal cooling air flow rate was 5700 m^3/h. Note that the present investigation mainly focused on proving the feasibility of this new prototype, although an optimization process concerning the management of the fluid flows is expected to be performed in further works.

As regards to the initial concentration of the LiBr/H_2O solution, it was maintained at the same value as for the single-effect testing; that is 56% of LiBr.

7.4 Data reduction

In order to obtain some working parameters of the prototype such as heat transfer rates or performances, the following expressions were used. Note that only equations which are different from those utilized in the single-effect evaluation will be written.

To begin with, if heat losses to surroundings are neglected, the power delivered by thermal oil to LiBr/H_2O solution in the high-pressure generator can be obtained as

$$Q_{HG} = \dot{m}_{oil} \cdot c_{p,oil} \cdot (T_{i,oil} - T_{o,oil}) \tag{7.1}$$

The cooling power provided by the prototype (Q_e) is calculated from an energy balance in the evaporator as indicated for the single-effect stage, Equation (6.4).

Neglecting thermal losses to ambient, the following energy balance can be written for the chiller considered as a whole

$$Q_{ca} = Q_a + Q_{cond} = Q_e + Q_{HG} \tag{7.2}$$

where the heat transferred in the absorber cooler (Q_a) can be obtained from Equation (6.6). Notice that if knowing Q_{ca} and Q_a, the heat transferred in the condenser (Q_{cond}) may be assessed.

The cooling effectiveness of the solution heat exchangers is evaluated by means of the following simplified equations

$$\varepsilon_{Hshx} = \frac{T_{osHG} - T_{isa,HG}}{T_{osHG} - T_{osa}} \tag{7.3}$$

$$\varepsilon_{Lshx} = \frac{T_{osLG} - T_{isa,LG}}{T_{osLG} - T_{osa}} \tag{7.4}$$

The prototype's thermal coefficient of performance is defined as the following ratio

$$COP_{th} = \frac{Q_e}{Q_{HG}} \tag{7.5}$$

The electrical COP is given by the same expression as utilized for the single-effect operation mode. In the same way, for the formulae calculating the average performance of the absorption prototype during a day or a season, the reader is referred to Chapter 6.

The thermodynamic properties corresponding to all the working fluids were obtained according to (Pátek & Klomfar, 2006) and (ASHRAE, 2009).

7.5 Experimental results

Apart from a few preliminary trials, the double-effect experimental campaign consisted of three tests carried out in 2010. The two first experiments were performed at the end of August while the last one was in October. Note that most of the days in summer were devoted to test the single-effect operation stage making use of the available solar energy. This is the reason why only a few experiments concerning the double-effect stage were performed in summer.

In this section, a summary of results obtained during the whole experimental campaign will be shown. Likewise, the results corresponding to the test performed on 11 October 2010 will be presented and discussed in detail.

7.5.1 Results on 11 October 2010

First of all, it is interesting to say that 11 October 2010 was a normal autumn day in the region of Madrid. It was cloudy and the ambient temperatures did not exceed 18°C, Figure 7.2. Consequently, in order to carry out a valid experiment on absorption machines supplying air conditioning, both outdoor and indoor conditions had to be artificially modified. In this sense, the climatic chamber where the prototype is placed was adapted to obtain the ambient conditions corresponding to a typical summer day in Madrid. The obtained distribution of temperatures was plotted in Figure 7.3. As seen, the high artificial temperature was 36°C around 17:00 h, when natural temperature was some 18°C.

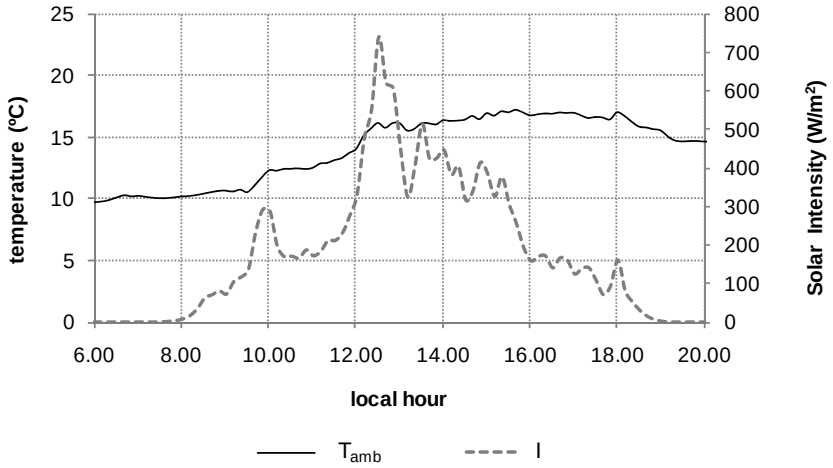

Figure 7.2 Meteorological conditions on 11/10/2010

On the other hand, with the aim of simulating summer thermal loads inside the air conditioned space, an 8 kW-electrical heater was used.

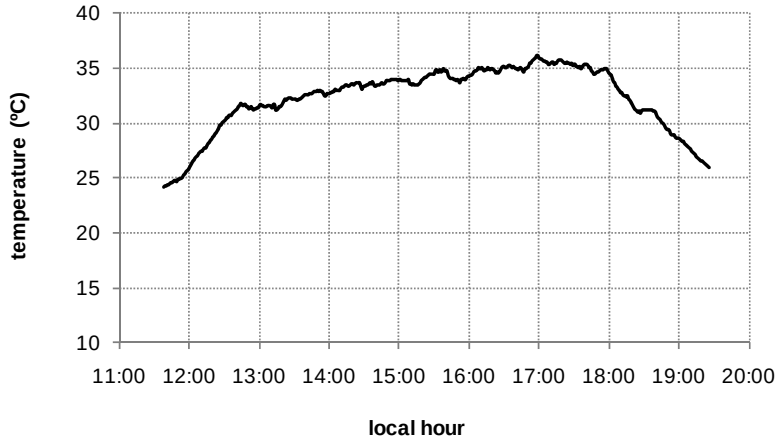

Figure 7.3 Artificial outdoor temperatures on 11/10/2010

Following, the working parameters obtained from the test carried out on 11 October 2010 will be presented and discussed. The experiment began at about 11:50 h and concluded at 19:20 h, which means 7.5 hours of operation.

High- and low-pressure generators

To begin with, temperatures corresponding to both sides of the high-pressure generator are plotted in Figure 7.4. It was observed that, after some fluctuations at the very beginning of the test, the thermal oil temperature kept continuously raising; it went from 130°C at 12:00 h to approximately 182°C at 17:30 h. After this point, the electrical resistances in the oil tank were gradually disconnected and, as a result, the driving temperature decreased rapidly. At 18:05 h the supply of thermal oil to the generator was cut off, which explains the sudden drop in the represented temperatures.

From Figure 7.4 it is also observed that the difference between $T_{i,oil}$ and $T_{o,oil}$ was gradually increasing during the experiment, especially during the first hour. This fact means that the input power tended to grow in the course of the test. Another interesting aspect from Figure 7.4 is that temperature differences between the oil and the solution at the outlet of the generator were relatively small, mostly about 2°C. This fact can be regarded as an evidence of the high heat transfer rates obtained in the plate heat exchanger.

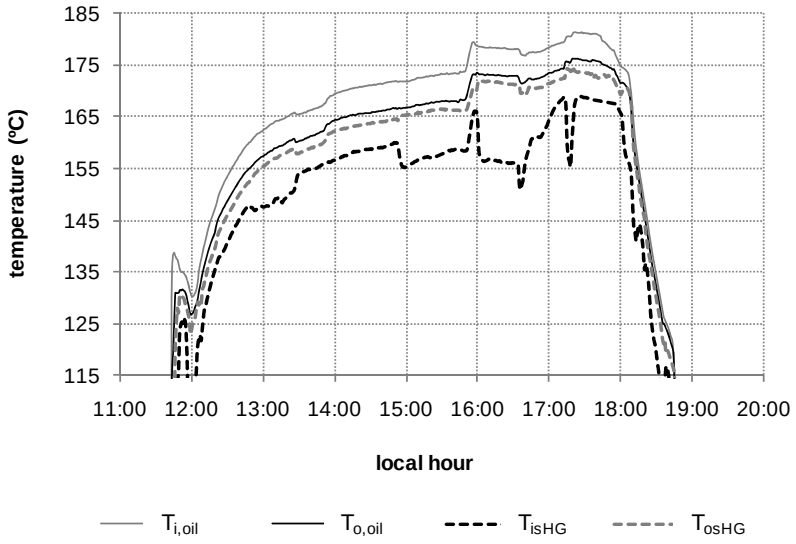

Figure 7.4 Temperatures in the high-pressure generator (11/10/2010)

On the other hand, Figure 7.5 depicts temperatures of the fluids flowing through both sides of the low-pressure generator. The inlet temperature of the refrigerant separated in the high-generator was not directly measured, but it can be approximated by the temperature of the solution at the outlet of the high-generator, (Izquierdo, 1996). Note that, since the coolant coming from the high-generator enters the low-generator as superheated vapor, it firstly delivers sensible heat until saturation conditions are reached and then it gets condensed. Assuming the subcooling at the outlet of the low-generator is negligible, condensation temperatures ($T_{or,LG}$) were between 85°C and 110°C. Thanks to the heat transferred from the refrigerant, LiBr/H_2O solution increased its temperature and, eventually, boiled at temperatures ranging from 80°C to 105°C.

Regarding the solution mass flow through the generators, Figure 7.6 shows the measured values for each device. The grey dotted line represents the solution mass flow rate circulating through the high-generator whereas the black dotted line corresponds to the solution flowing through the low-generator. The continuous line, in turn, is the total solution leaving the absorber. It is interesting to note that the total solution mass flow was regulated depending on the input oil temperature: higher driving temperatures implied higher solution mass flow rates. In this case, the total mass flow rate ranged from 0.13 kg/s at the beginning of the experiment to 0.18 kg/s around 17:00 h, when the outdoor temperature was in its high. Except for a few instants, the solution flowing through the high-generator was some 70% of the total rate during the whole experiment.

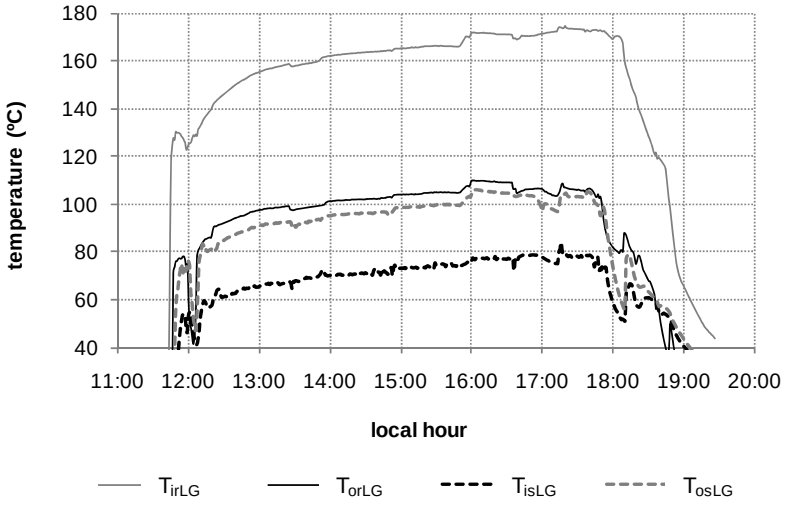

Figure 7.5 Temperatures in the low-pressure generator (11/10/2010)

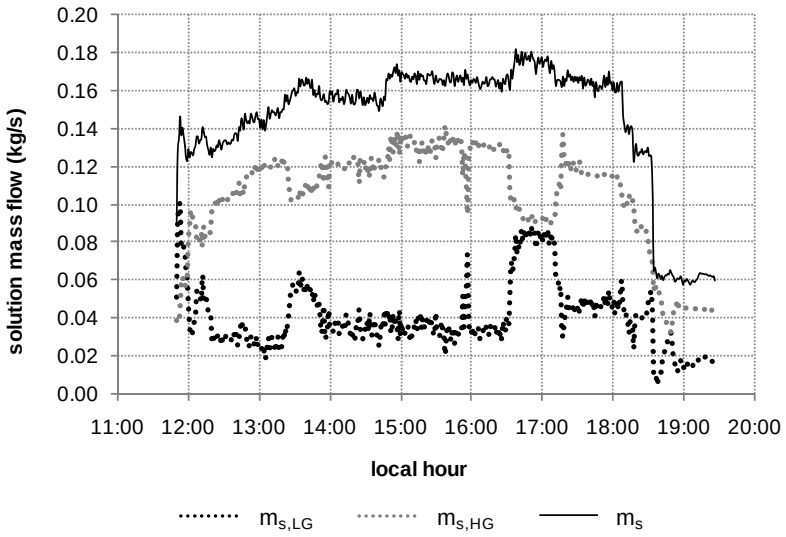

Figure 7.6 Solution mass flow rates (11/10/2010)

On the other hand, it is interesting to note that sudden variations in the solution mass flow caused peaks in the solution temperatures at the inlet of the generators, as regarded for instance around 13:30 h, 14:50 h or 16:00 h. In general, it was observed that steep increases in the solution mass flow rates yield abrupt decreases in the solution temperatures. This effect, which is much more noticeable for the high-generator circuit (Figure 7.4), is due to the fact that heat transfer process in the SHXs is strongly influenced by the mass flow rates circulating inside. It is though that an improved control system could mitigate the observed fluctuations.

Absorber

Figure 7.7 shows the characteristic temperatures in the absorber of the prototype; that is: temperatures of the solution entering the absorber from the solution heat exchangers ($T_{isa,HG}$, $T_{isa,LG}$); temperatures of the solution pumped to the generators (T_{osa}); solution temperature at the outlet of the absorber air-cooler (T_{osac}). Likewise, outdoor temperature (T_{out}) is also represented to establish comparisons. Note that temperatures T_{isac} and T_{osa} are exactly the same: they represent the temperature of the solution in the absorber's tank. Henceforward T_{osa} will be also referred as final absorption temperature.

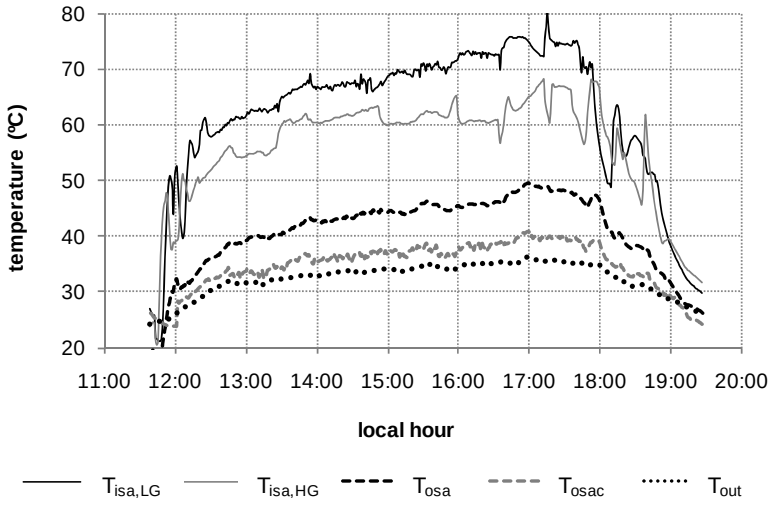

Figure 7.7 Temperatures in the absorber (11/10/2010)

In Figure 7.7, it is seen that the temperature of the solution coming back to the absorber from the solution heat exchangers raised as the experiment developed. In this way, $T_{isa,HG}$ and $T_{isa,LG}$ were from 45°C at the beginning of the experiment to 68°C and 75°C around 17:30 h, respectively. Besides, it is interesting to highlight the good performance of the solution air-cooler, which was able to reduce the solution temperature up to 10°C and, as a result, kept the final absorption temperature under 50°C at any instant. Solution temperature in the absorber's tank was maintained between 8°C and 13°C above the outdoor temperature during the whole experiment. However, it is interesting to mention that it was mostly around 10-11°C. Although this temperature difference was higher than observed in the single-effect mode, it can be still regarded as an important achievement for development of air-cooled double-effect absorption chillers based on LiBr/H_2O. Note that, to the best of our knowledge, no similar technology is currently present on the market. Nonetheless, it is important to mention that lower final absorption temperatures may be

obtained by improving the heat transfer in the solution air-cooler. A simple way to do that is to increase the mass flow rate of the air through the heat exchanger by installing a fan with higher capacity. Note that the air flow rate used in this experiment was considerably lower than the optimum value extracted from Chapter 5.

Solution Heat Exchangers

Regarding the operation of the high-solution heat exchanger, Figure 7.8 shows both the solution temperature reduction and the heat transfer effectiveness (ε_{Hshx}). As seen, this plate heat exchanger was able to reduce the temperature of the solution coming from the generator up to some 110°C. Besides, the effectiveness of the heat transfer process varied between 0.86 and 0.90 during the most of the experiment; 0.87 was the mean value for the whole test. As earlier mentioned, the fluctuations observed in the curves are mainly caused by variations in the solution mass flow through the heat exchangers.

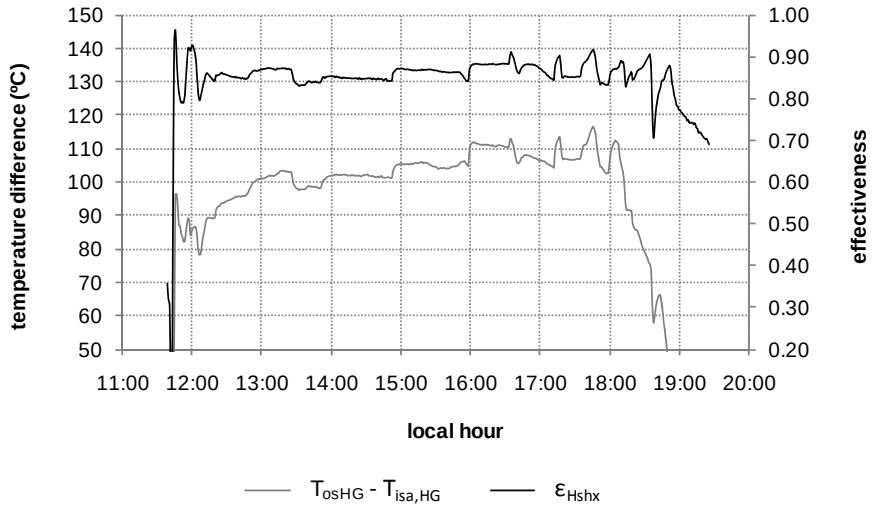

Figure 7.8 Working parameters of the high-solution heat exchanger (11/10/2010)

As far as the low-solution heat exchanger is concerned, Figure 7.9 shows that it permitted to reduce the temperature of the solution coming from the low-generator up to 34°C. As compared to the high-SHX, the effectiveness of the low-SHX was noticeably lower. The measured values for ε_{Hshx} mostly ranged between 0.53 and 0.59, while the mean effectiveness was 0.55. These performance results are poorer than expected, which means that this is a point to be improved in future prototypes. By installing a more efficient solution heat exchanger, the final absorption temperature could be lowered and, consequently, the risk of crystallization might be reduced.

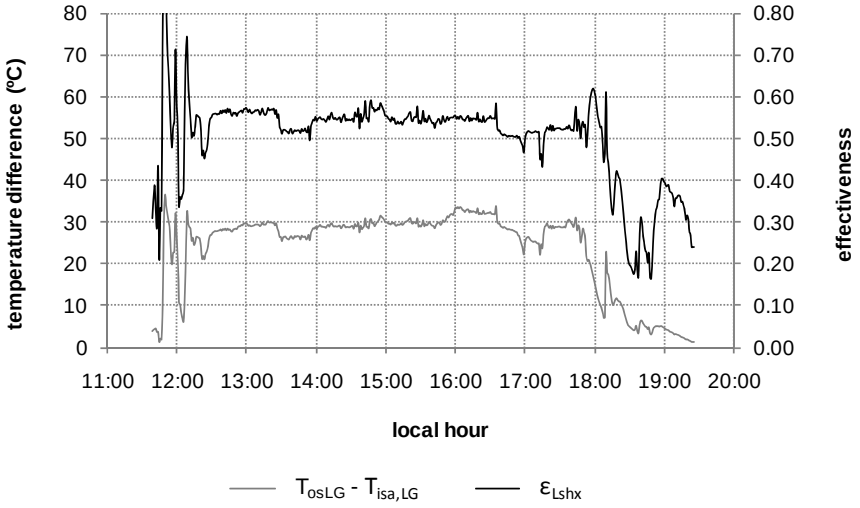

Figure 7.9 Working parameters of the low-solution heat exchanger (11/10/2010)

Condenser

The condensation temperature of the refrigerant separated in the low-generator (T_{rcond}) is represented in Figure 7.10. Besides, this plot shows the temperatures of the cooling air before and after passing through the prototype, (T_{out} and T_{oca}, respectively). It is worth mentioning that the condensation temperature was maintained between 40 and 48°C during the operation of the prototype. The difference between the condensation and the outdoor temperatures was about 12-14°C, which is similar to that found for the single-effect stage. This fact may be regarded as an evidence of the good design achieved for the condenser.

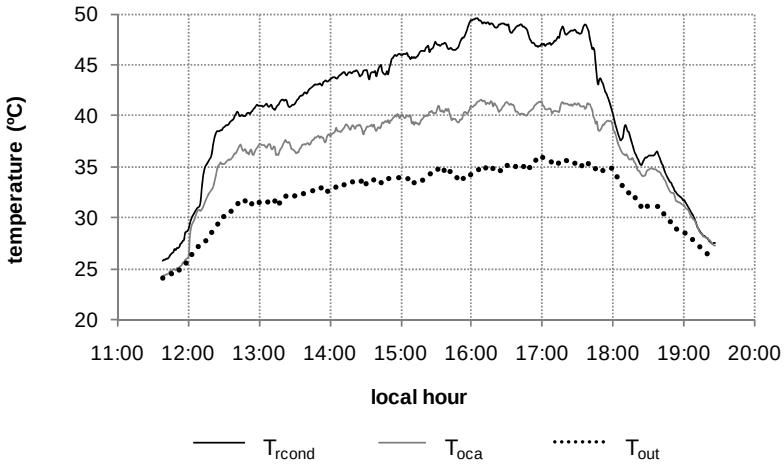

Figure 7.10 Temperatures in the condenser (11/10/2010)

On the other hand, it is interesting to mention that, after passing through the absorber heat exchanger, the condenser and the subcooler, the air increased its temperature between 5°C and 7°C.

Evaporator

In Figure 7.11 one can see the cooling effect of the prototype. The data shown are water temperatures at the inlet and the outlet of evaporator (T_{iwe}, T_{owe}), evaporation temperature (T_e) and indoor temperature in the air conditioned space (T_{in}). As earlier mentioned, an electrical heater was used with the purpose of simulating summer thermal loads in the air conditioned space. Actually, the peaks observed in the curve of indoor temperature are due to the start-up and shutdown of the heater. In spite of the not very accurate control system, the indoor temperature was successfully maintained between 23 and 26°C, which corresponds with the comfort temperatures recommended by current Spanish regulations, (MICYT, 2007).

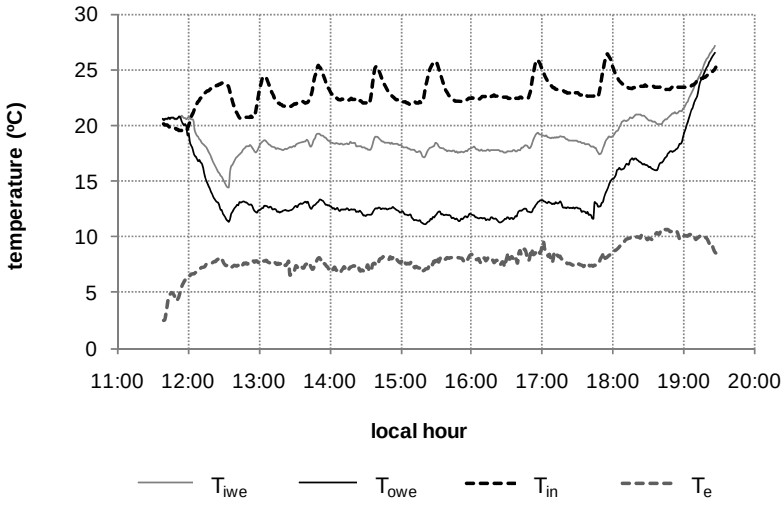

Figure 7.11 Temperatures in the evaporator and the air conditioned space (11/10/2010)

From Figure 7.11 it can be drawn that the prototype was able to cool down the chilled water from 20°C to 13°C in just one hour after the start-up. Then, the water temperature was maintained between 11.5°C and 13°C during approximately the following five hours; that is until the electrical resistances in the thermal oil tank begun to be disconnected. Note that during this period of time, the outdoor temperature increased from 31°C to 36°C. The lowest water temperature was 11.2°C, registered around 13:30 h, when

outdoor temperature was 34°C. Another aspect worth mentioning is that, at the maximum outdoor temperature, water temperature was decreased about 6°C in the evaporator.

Regarding the steep decrease observed in the water temperature just after the start-up, it is interesting to notice that it coincides with a marked growth in the indoor temperature. The reason of this unusual event must be found in an incidental disconnection of the fan moving the indoor air through the fancoil. Owing to this fact, the heat could not be properly transferred from the chilled water to the indoor air during a period of about 30 minutes. Once the error was detected and corrected, the temperature of the chilled water increased rapidly and the indoor temperature began to decrease.

Lastly, it is interesting to mention that, to a certain extent, the good results obtained for the evaporator are due to the very low pressures achieved in the evaporator-absorber assembly. The evaporation temperature hardly went over 10°C, which means that evaporation pressure did not exceed 1.2 kPa.

Energy balances

In Figure 7.12, the cooling capacity (Q_e) is plotted together with the input power to the high-generator (Q_{HG}). Heat power absorbed by LiBr/H_2O solution went from 3 kW at the start-up to about 4.6 kW, which was maintained during most of the experiment. The observed fluctuations were mainly caused by the aforementioned solution flow regulation.

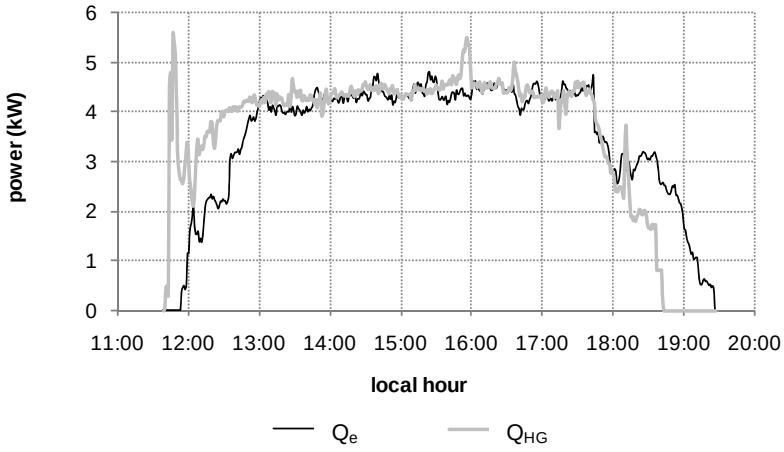

Figure 7.12 Heat power delivered in both the evaporator and the generator (11/10/2010)

With regards to the cooling power, the measured values ranged from 2 kW at start-up to a maximum of 4.7 kW, reached about 15:30 h. It is notable that the cooling power

was more or less constant around 4.5 kW during a long period of time, in which the outdoor temperature increased from 33°C to 36°C. Note that this cooling production is about 65% of the nominal capacity of the prototype's double-effect stage. Apart from other possible reasons, the underproduction of cooling effect is likely caused by the low heat power absorbed by the solution in the high-generator, whose design capacity was 6 kW.

Another aspect worth mentioning from Figure 7.12 is the rapid response of the prototype, which was able to deliver cooling power only 15 minutes after the start-up. Moreover, it is notable that refrigeration continued some minutes after cutting off the hot oil supply thanks to the inertia accumulated in the prototype. That is to say, the refrigerant remaining in the condenser was able to produce cooling effect for a few minutes after the shutdown of the thermal oil facility.

Figure 7.13 shows the total heat power removed from the prototype by the air-cooling system (Q_{ca}), as well as the heat rate transferred in the solution air cooler (Q_a). It is observed that the heat power rejected to the atmosphere experienced a marked raise until 13:00 h, but afterwards the increase in Q_{ca} was relatively small. Actually, it went from 9 kW at 13:00 h to some 10 kW at 17:30 h.

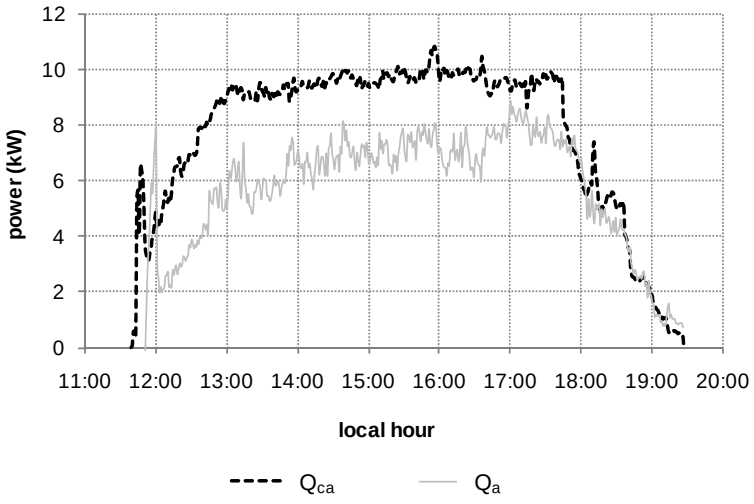

Figure 7.13 Heat power rejected to the atmosphere by the air-cooling system (11/10/2010)

On the other hand, the heat power removed from the absorber was observed to be gradually increasing until the disconnection of the electrical resistances in the oil tank. The value of Q_a was around 6 kW at 13:00 h, while it was close to 9 kW at 17:30 h. The steady growth of Q_a can be explained by the fact that, whereas both the solution and the air flow rates were kept constant during the whole experiment, the difference between T_{isac} and

T_{out} was continuously increasing, which enhanced the heat transfer from solution to ambient air.

Performance

The thermal coefficient of performance obtained during the present test is plotted in Figure 7.14. Taking no account of the start-up and shutdown processes, one can see that COP_{th} was around 1.0 for some five hours, that is, for the period of time working at approximately steady conditions. Similarly to the single-effect stage, in the final part of the experiment a rapid increase in COP_{th} was observed. This was due to the aforementioned effect of the inertia in the prototype: while the input heat power began to decrease sharply after the disconnection of the electrical resistances, the remaining refrigerant in the machine was still able to produce cooling effect and, as a result, the COP_{th} dramatically increased. The slight spikes observed during operation of the prototype are mostly due to the solution flow regulation. If considering the COP_{th} throughout the whole experiment, a ratio of 0.96 was obtained, which is in good agreement with values reported in the literature for air-cooled double-effect absorption machines.

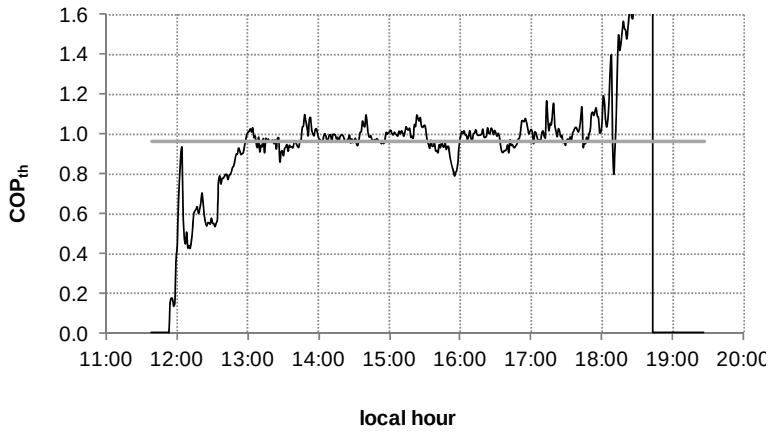

Figure 7.14 Thermal coefficient of performance (11/10/2010)

On the other hand, regarding the electricity consumed by the ancillary equipment of the prototype (solution pumps and fan), a mean value of 945 W was measured. This consumption can be considered as practically constant during the whole experiment because all the fluid flows in the prototype were kept invariable, except for the solution mass flow through the generators. In this sense, Figure 7.15 shows the electrical COP, which is the ratio between the cooling power delivered in the evaporator and the electrical consump-

tion of the prototype. As seen, it mostly ranged between 4.3 and 5.0, while the daily averaged value was 4.05.

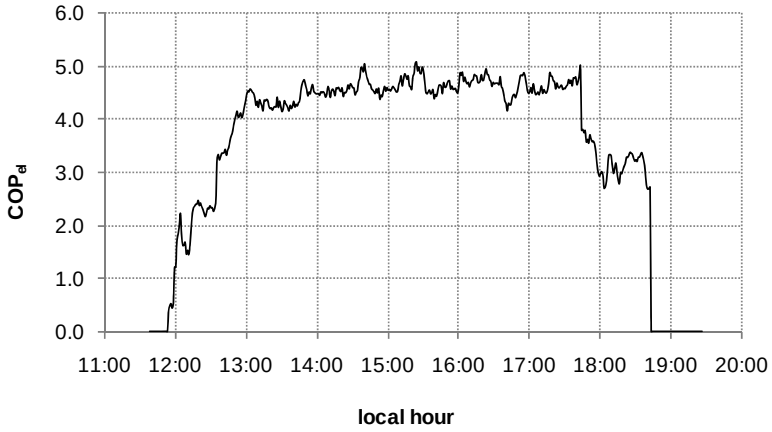

Figure 7.15 Electrical coefficient of performance (11/10/2010)

Interesting to mention is that, at outdoor temperatures of 35°C, the COP_{el} of the prototype was about 4.7. This result is regarded as an evidence of the excellent potential of air-cooled double-effect absorption machines to compete with conventional air-cooled vapor compression systems. Notwithstanding, we strongly believe that electrical consumption can be considerably cut down by carrying out an optimization of the prototype, especially if focusing on the regulation of the different flows in the machine.

Solution cycle

An interesting aspect to be analyzed in experimentation of LiBr/H_2O absorption machines is the cycle described by the solution. In this regard, the three following figures represent the concentration changes experienced by the solution throughout the current test. Note that, since equilibrium conditions were assumed in the calculation of the concentration values and the operation of the prototype was not completely steady, the results showed in those plots can not be regarded as final conclusions. However, they may be useful to approximately know the concentration ranges in which the prototype operated and, what is more, to know how far we were from crystallization conditions.

Figure 7.16 and Figure 7.17 show the concentration of LiBr/H_2O solution at the outlets of both the absorber (X_a) and the two generators (X_{HG} and X_{LG}). Likewise, the difference of concentrations between the weak and strong solutions is represented for each generator (ΔX_{HG} and ΔX_{LG}). From an observation of both figures, it can be drawn that solution left

the low-generator slightly more concentrated than the high-generator. Whereas the mean value for ΔX_{HG} was 2.43%, it was 3.12% for ΔX_{LG}. The main reason for such a difference may be found in the solution mass flow regulation. As seen in Figure 7.6, the solution flow rate through the high-generator was about 2.5 times greater than through the low-generator, which presumably caused a lower increment of the solution concentration in the high-generator. This effect is confirmed by the fact that ΔX is affected when varying the solution distribution through the generators. This is clearly observed, for instance, around 16:40 h, when the ratio between $m_{s,HG}$ and $m_{s,LG}$ was significantly modified. The solution rate circulating through the low-generator was considerably increased and, as a result, the solution concentration at its outlet decreased sharply. Conversely, the marked decrease in the solution flow rate through the high-generator triggered a sudden increase in the solution concentration at its outlet.

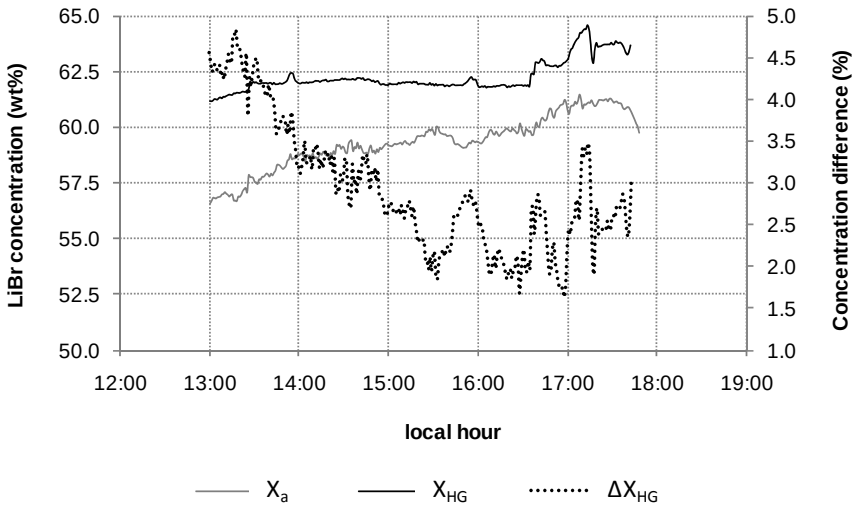

Figure 7.16 Solution concentrations at the inlet and outlet of the high-generator (11/10/2010)

On the other hand, from Figure 7.16 and Figure 7.17 it is interesting to draw that the concentration the $LiBr/H_2O$ solution was mostly between 62% and 63%. Only in a few moments associated with fluctuations in the solution mass flows, the concentration at the outlet of the generators reached values around 64%. Regulation of solution appears therefore as a key factor in operation of parallel flow double-effect absorption chillers.

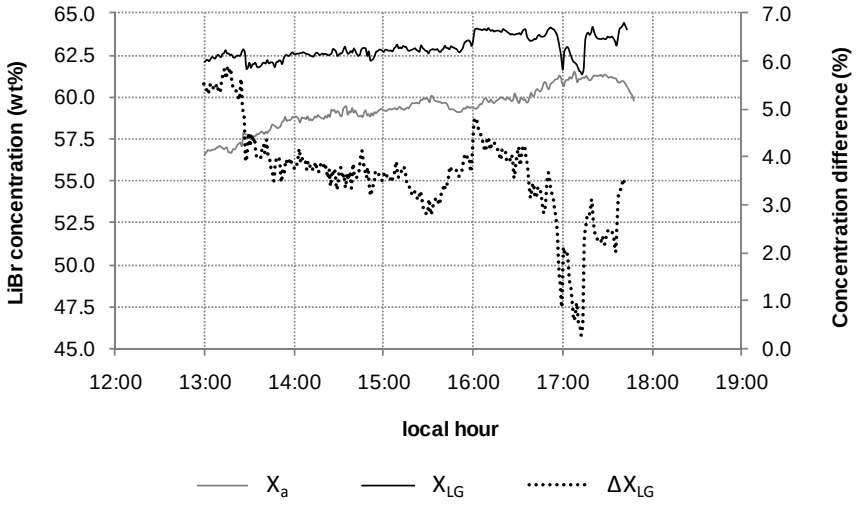

Figure 7.17 Solution concentrations at the inlet and outlet of the low-generator (11/10/2010)

In order to ascertain how far from crystallization limits we were, two absorption cycles at different moments of the experiment were represented in a Dühring chart, Figure 7.18. Additionally, some of the cycle properties are indicated in Table 7.1. In view of the results, it can be said that the prototype worked reasonably far from conditions triggering crystallization of $LiBr/H_2O$ solution. Besides, in that plot one can see that the increment of concentration in both generators was lower as the outdoor temperature increased.

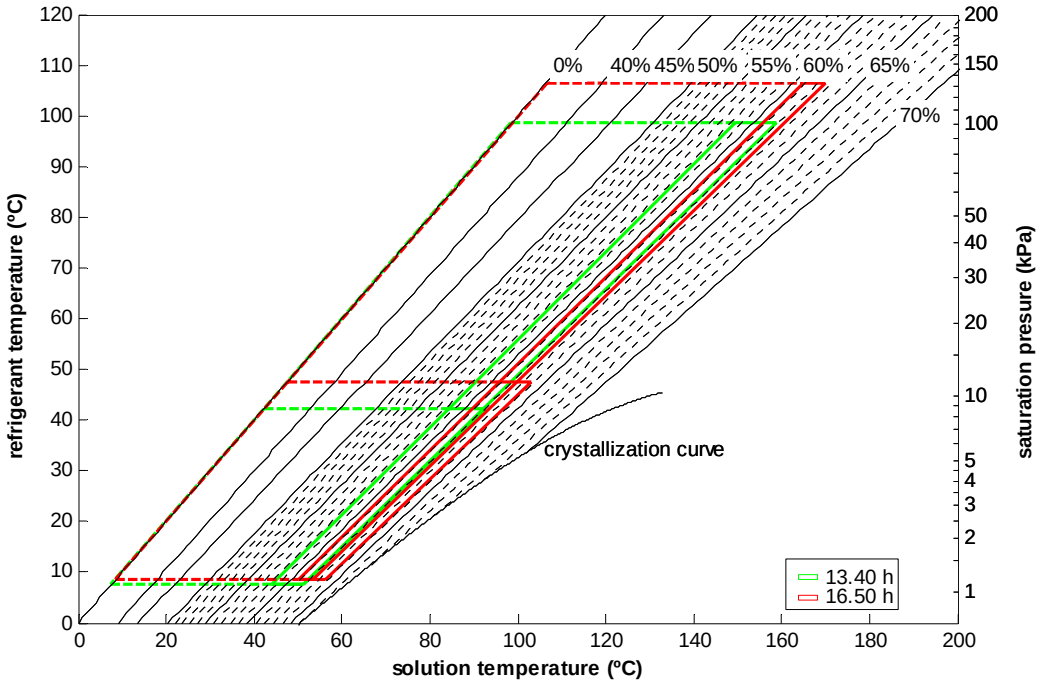

Figure 7.18 Absorption cycles in the Dühring diagram (11/10/2010)

Table 7.1 Properties of the represented absorption cycles (11/10/2010)

Hour	T_{out}	T_a	T_e	T_{rcond}	$T_{or,HG}$	ΔX_{HG}	ΔX_{LG}
13:40	32.5	44.0	7.52	42.3	98.5	3.5	3.62
16:50	35.0	50.6	8.62	47.6	106.5	1.7	2.99

In spite of the good results achieved in terms of solution crystallization, we think it is still possible to work with a higher safety margin by lowering the absorption temperature. In order to do this, the aforementioned actions may be carried out: improving the effectiveness of the low-solution heat exchanger and increasing the air flow rate through the absorber's cooler.

7.5.2 Results for the whole campaign: summary

As above mentioned, during the double-effect experimental campaign three tests were carried out. Two of them were performed at the end of August and the last one was in October. Figure 7.19 depicts the energy balance results and the daily thermal COP corresponding to each day in the experimental period. As the counterpart of the figure, Table 7.2 shows some additional results concerning each test and the whole campaign.

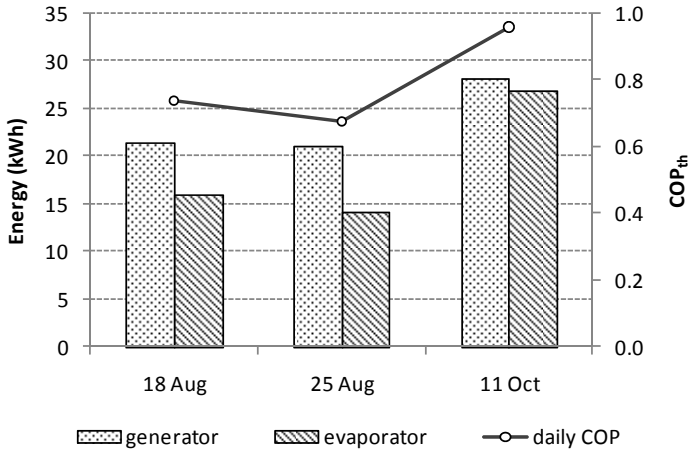

Figure 7.19 Energy balance and daily COP_{th} for the whole double-effect experimental campaign

Firstly, it is interesting to note the significant improvement achieved in the prototype's performance from the two first experiments to the last one. Whereas in the former tests the daily COP_{th} was not higher than 0.75, a value of 0.96 was reached in the experiment performed on 11 October. This notable enhancement was mainly due to several ad-

justments carried out in the regulation system. However, we are not completely satisfied with the obtained performance and, consequently, more modifications are planned for the near future.

Table 7.2 Summary of the energy balance for the double-effect stage

Day	Time (h)	E_{HG} (kWh)	E_e (kWh)	COP_{th}	COP_{el}
18 August	7.5	31.35	15.75	0.74	2.22
25 August	6.0	20.83	14.04	0.67	2.48
11 October	7.5	28.00	26.81	0.96	4.05
Campaign	22.0	70.19	56.60	0.81	2.92

On the other hand, a remarkable aspect of this experimental campaign is that no crystallization signs were noticed during about 22 hours of operation under double-effect operation mode. Moreover, neither significant corrosion signs nor important failures were detected during the whole campaign, which proves the robust design of the prototype.

7.6 Experimental uncertainties

Following procedure given in Appendix A, an experimental uncertainty analysis was performed for the double-effect operation mode. The mean results for the main parameters used in this chapter are presented in Table 7.3.

Table 7.3 Experimental uncertainties in double-effect mode

Operation parameter	Uncertainty
Q_a	± 4.3 %
Q_{HG}	± 4.2 %
Q_e	± 4.2 %
COP_{th}	± 5.0 %

7.7 Comparison with predicted results

In this section, a comparison is made between the above exposed results and the corresponding values from the numerical simulation described in Chapter 4. In this regard, Table 7.4 shows the values obtained for some of the main working parameters of the

prototype. Note that only results from the test carried out on 11 October were selected to do the comparison because, as above mentioned, this was the only experiment with acceptable performance outcomes. The results obtained for an outdoor temperature of 35°C under more or less steady conditions were used to ascertain how close the measurements and the predictions were.

Table 7.4 Comparison of experimental results with predicted values (double-effect)

Working Parameter	11 October (T_{out}=35°C)		
	Tested	Predicted	Difference (%)
COP_{th}	1.01	1.18	-14%
Q_e (kW)	4.5	7.0	-35.7%
Q_{HG} (kW)	4.5	6.0	-23.7%
W_{aux} (W)	945	760	+24.3%
T_e (°C)	7.9	7.7	+2.6%
T_a (°C)	45.7	43.0	+5.9%
T_{rcond} (°C)	49.1	47	+4.2%
ε_{Hshx}	0.90	0.80	+12.5%
ε_{Lshx}	0.57	0.80	-28.75%

From Table 7.4 it is seen that measurements of COP_{th} were in reasonably good concordance with predictions. However, the cooling power delivered by the prototype was substantially lower than expected. On these grounds, and taking into account that the real input power was also significantly lower than predicted, it can be stated that a higher cooling power could be achieved by enhancing the heat transfer in the high-generator.

Regarding the electricity consumption of ancillary equipment, it was observed to be between 25% and 30% higher than expected. In this vein, it is interesting to mention that, as the experiments were performed at constant flow, it is though that the electric consumption can be easily cut down by carrying out an optimization of the different flow rates.

On the other hand, the measured evaporation temperature was observed to be in an excellent agreement with predictions. On the contrary, absorption temperature was noticeably underpredicted. To a certain extent, this fact was due to the poor effectiveness of

the low-solution heat exchanger, as earlier stated. Note that, whereas the effectiveness of the high-solution heat exchanger was greater than expected, the values obtained for ε_{Lshx} were notably lower than predicted. As above pointed out, another cause of the high absorption temperatures is likely the capacity of the fan. Circulating a higher air flow rate through the prototype could contribute to reduce the discrepancies between predictions and measurements not only for T_a, but also for T_{rcond}, which, as seen in Table 7.4, was higher than expected.

7.8 Conclusions

An experimental campaign consisting of three tests was carried out in 2010 to evaluate the behavior of the prototype working as an indirectly fired double-effect absorption machine. A summary of the main obtained results is as follows.

The double-effect stage of the prototype was able to work with thermal COP around 1.0 and electrical COP about 4.0, when outdoor temperatures were about 35°C. Under these conditions, a cooling power of 4.5 kW was delivered by supplying the high-generator of the prototype with thermal oil at approximately 180°C. The corresponding absorption and condensation temperatures were mostly around 10-11°C and 12-14°C higher than ambient temperatures, respectively. The effectiveness of the high- and low-solution heat exchangers resulted to be around 0.90 and 0.57, respectively. Regarding the crystallization problem, the solution was observed to work reasonably far from the critical conditions. In fact, after about 22 hours of operation, no crystallization signs were detected.

The results obtained during the present experimental campaign are considered to be very good and promising, specially taking into account that there is not any air-cooled double-effect $LiBr/H_2O$ absorption machine currently in the market. However, it is believed that better results can be still achieved. In this sense, the following measures were proposed to improve the performance of the prototype: firstly, implementing a more accurate regulation system to avoid fluctuations during operation; secondly, increasing the capacity of the fan to lower the absorption temperatures and, consequently, reduce the crystallization risk; for the same purpose, it will be also interesting to enhance the effectiveness of the low-solution heat exchanger; another aspect to be improved is the heat transfer capacity of the high-generator, which limited the cooling power of the prototype; lastly, an optimization process must be carried out to reduce the electrical consumption of ancillary equipment.

Chapter 8

Experimental evaluation of the air-cooled adiabatic absorber: validation of the model

8.1 Introduction

In this chapter, specific experimental results of the absorber operation will be shown. Likewise, a comparison of those data with the corresponding results yielded by the mathematical model developed in Chapter 5 will be performed. In other words, the objective of this chapter is to present an experimental validation for the modeling of the air-cooled adiabatic absorber installed in the single–double-effect prototype.

8.2 Fundamentals of the model validation

In order to establish a comparison between experimental and theoretical results that allows for a validation of the absorber modelization, it was decided to run the mathematical model with experimentally measured parameters as input variables. Those variables are: pressure in the absorber chamber, outdoor temperature, mass flow rates in the solution air-cooler and solution conditions at the return of each generator (temperature and mass fraction).

The objective of the comparison is to contrast the experimentally measured values with the simulation results for the same input variables. In this vein, the following parameters were selected for validation of the model: heat transfer rate in the absorber air-cooler, solution temperatures at the beginning and the end of the flat-fan sheets, temperature of the solution in the absorber reservoir and cooling capacity of the machine.

Data used for comparison come from the trials carried out during the experimental evaluation of the single–double-effect prototype. Thus, the prototype itself can be regarded as the testing facility of the adiabatic absorber. Although details on the experimental setup can be found in Chapter 6 and Chapter 7, it is interesting to mention here that a thermocouple was installed inside the absorption chamber with the aim of measuring the solution temperature at the end of the liquid sheets. It was put at a distance of 200 mm from the nozzle injectors exit (see Chapter 5).

Below, one can firstly find a comparison between predictions and measurements corresponding to the trial performed on 5 August 2010, taken as an example to illustrate the behavior of the absorber during a real day. Subsequently, a comparison for data collected during the whole experimental campaign is given.

8.3 Results for a specific trial: 5 August 2010

First of all, one should realize that on 5 August 2010 the absorption prototype was operated in single-effect mode (see Chapter 6).

Figure 8.1 shows the comparison made for the heat exchanged rate in the absorber air-cooler. The black line represents the predicted values whereas the grey one represents the experimentally obtained results. As seen, the agreement is very good, especially in the central part of the experiment, when working conditions were closer to steady state conditions. It was found that about 85% of the measured data match the simulation results with an error lower than ±10%. Interesting to note is that the experimental uncertainty found for this parameter was around ±5% (see Chapter 6).

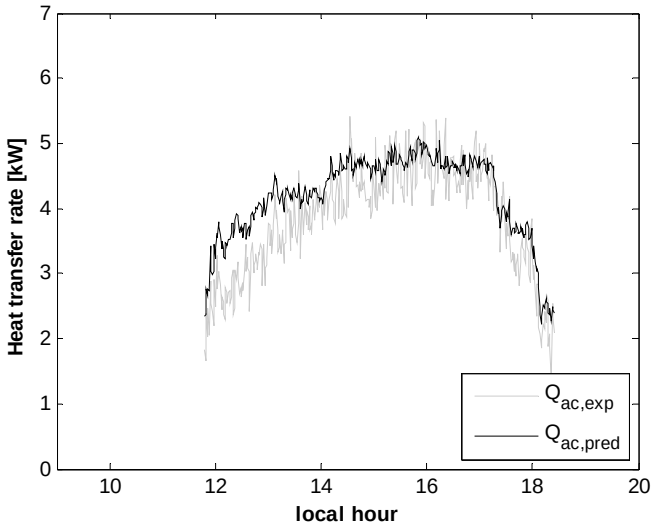

Figure 8.1 Heat transfer rates in the solution air-cooler of the absorber (05/08/2010)

The next parameter of the absorber to be analyzed is the solution temperature at the outlet of the absorber air-cooler, T_7 in Figure 5.1. As earlier mentioned, this is assumed to be the solution temperature at the beginning of the flat-fan sheets comprising the bank of sprayers. Figure 8.2 shows an excellent agreement between predictions and measurements, being the difference lower than 4% for all the data. As in the previous comparison, it was observed that the concordance is quite better in the central part of the experiment.

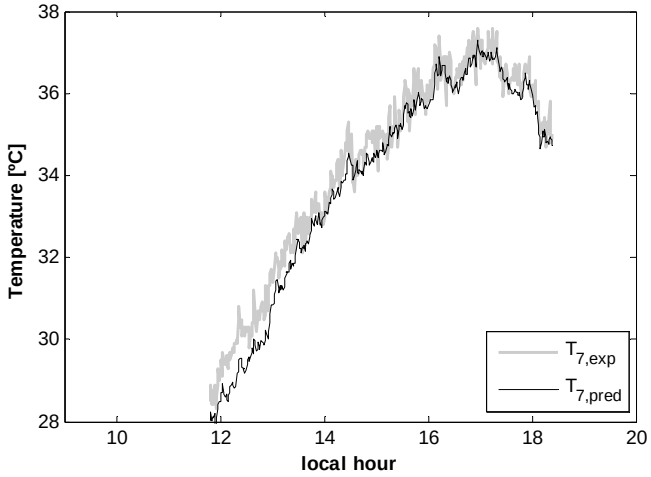

Figure 8.2 Temperatures at the beginning of the solution sheets (05/08/2010)

In Figure 8.3, the measured temperature at the end of the solution sheets is compared against the corresponding results from the simulation. In this case, it was observed that the absorber model tends to slightly underpredict the results. However, the mismatch was found to be within the 5% for almost all the measurements. On the other hand, if re-

garding data in Figure 8.2, it can be noticed that the solution temperature increased about 4-5°C as the sheet developed.

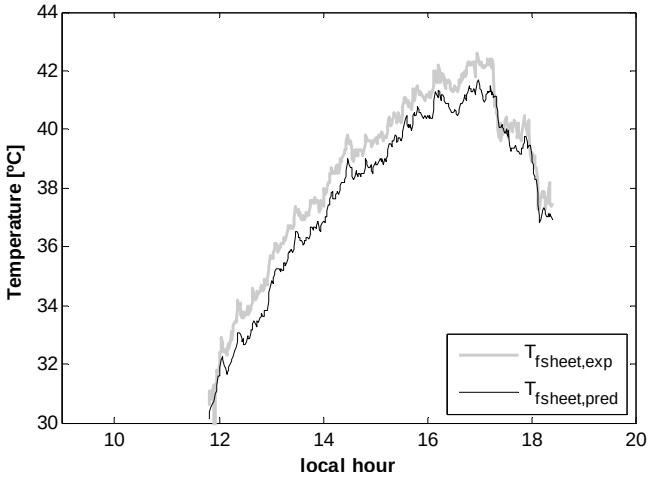

Figure 8.3 Temperatures at the end of the solution sheets (05/08/2010)

Figure 8.4 shows the temperature differences between the outdoor air and the solution in the absorber reservoir, T_1. As seen, a good agreement was found between experimental results and numerical values, being the experimentally measured temperatures around 7% lower than predicted.

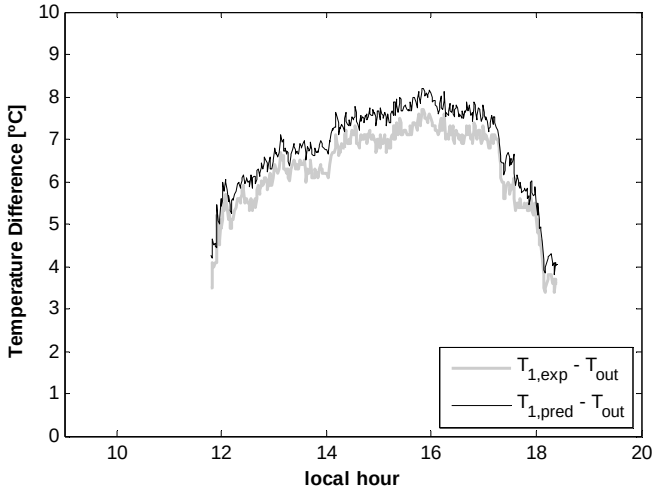

Figure 8.4 Temperature differences between the solution in the absorber and the outdoor air (05/08/2010)

Another noteworthy aspect drawn from Figure 8.4 is that the absorber cooler was able to maintain the solution temperature just between 5°C and 7°C above the ambient temperature in any case. This can be regarded as a relevant feature of the present ab-

sorber design since, owing to the low solution temperatures achieved, the machine was able to work far from crystallization limits. Moreover, it is interesting to underline that, as far as we know, there is not any direct air-cooled absorber for $LiBr/H_2O$ solutions with similar characteristics in the market.

Last but not least, Figure 8.5 compares the actual cooling power of the prototype with the potential cooling capacity drawn from the absorber simulation. It is interesting to note that, while the grey line represents the effective cooling power obtained from measurements in the chilled water circuit, the black line indicates the maximum cooling capacity that could be reached with the absorption power of the sheets (taking into account that the vapor produced in the expansion valve does not produce cooling effect). In this case, it can be seen that the cooling power delivered in the evaporator was about 20% lower than the total capacity of the absorber. However, in the central part of the experiment the difference was reduced to 10-15%.

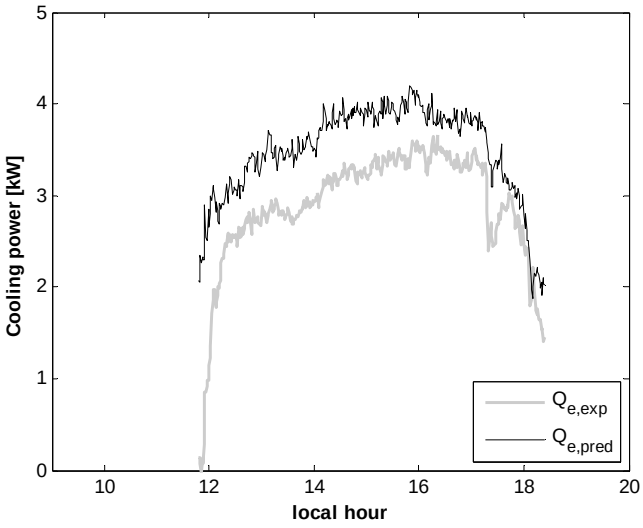

Figure 8.5 Comparison between measured and maximum cooling power (05/08/2010)

The difference noticed between $Q_{e,exp}$ and $Q_{e,pred}$ is supposed to be partially due to thermal losses in the evaporator. Nonetheless it is worth mentioning that, in order to reach the maximum capacity offered by the absorber, the prototype should produce a certain amount of refrigerant that, likely, was not being generated owing to several factors concerning the operation of the whole prototype. On the other hand, a thermal lag effect may be noticed when regarding Figure 8.5. It is seen that simulation model assumes a faster startup than obtained in experiments, which also contributes to disagreement between measurements and predictions.

8.4 Results for the overall experimental period

In the following figures, the main working parameters of the absorber obtained during the whole experimental campaign are plotted against the corresponding values from simulations. Data collected during the start-up and shutdown processes were not taken into account because of the fluctuations and irreversibilities taking place.

As regards to the heat power rate in the solution air-cooler, Figure 8.6 shows a quite good agreement between experimental and simulation results. In fact, around 80% of data were within ±10%. However, a slight tendency to underprediction was observed, which is more noticeable at higher ambient temperatures. The rather wide band of mismatch observed for Q_{ac} is probably due to the fluctuations in the air flow rate. Whereas the nominal flow rate given by the fan was used to obtain the predicted points, in the experiences the air flow rate was observed to be slightly variable. This fact likely introduced an additional error in the comparison.

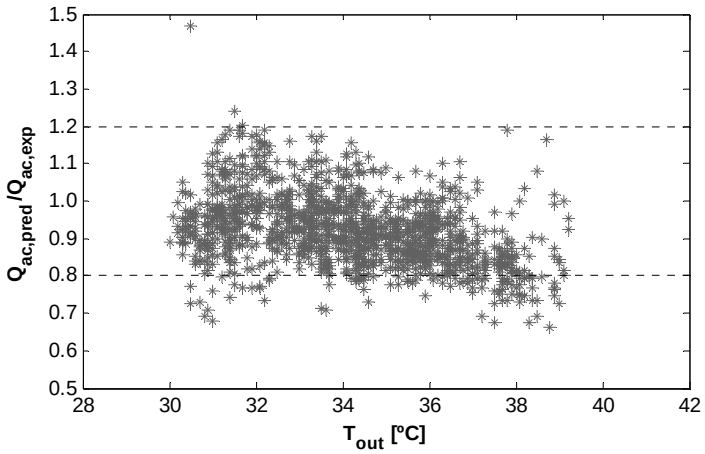

Figure 8.6 Comparison of experimental and predicted absorber parameters: Q_{ac}

Figure 8.7 and Figure 8.8 compare the experimental and the predicted values for the solution temperatures at the beginning and the end of the sheets, respectively. In both cases, it can be said that the mathematical model fits very well the measurements as the discrepancies were lower than 5% in any case. Especially interesting is to underline the excellent prediction for the final temperature of the solution sheets, which can be regarded as an evidence of the goodness of the absorption process modelization. A slightly greater discrepancy was found for the temperature at the initial position of the sheet, which is likely due to the aforementioned underprediction of the heat transfer rate in the air-cooler.

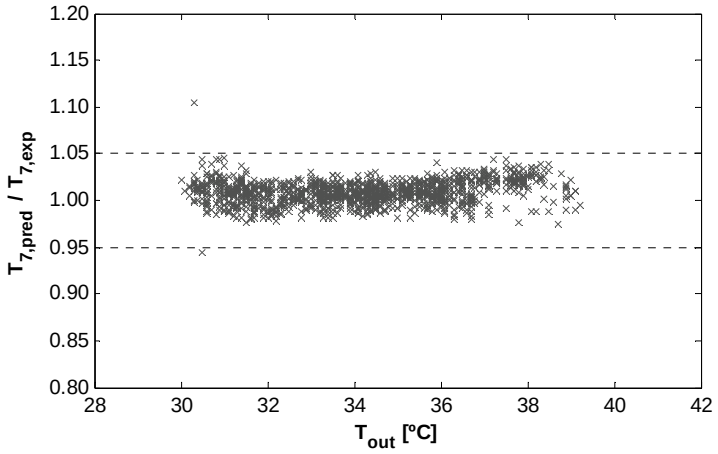

Figure 8.7 Comparison of experimental and predicted absorber parameters: T_7

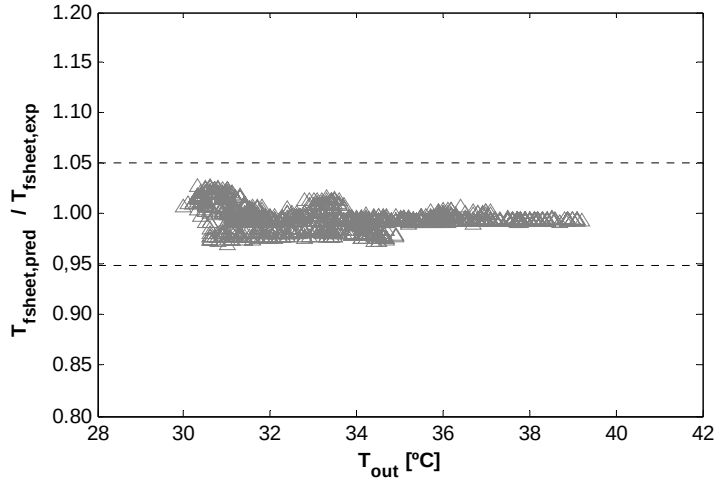

Figure 8.8 Comparison of experimental and predicted absorber parameters: $T_{f,sheet}$

Regarding the temperature in the solution reservoir, the agreement between measurements and predictions was satisfactory, as shown by Figure 8.9. In this graph, comparison was made by using the difference of temperatures between the solution in the absorber and the outdoor air, which is considered as a decisive parameter in absorbers design. It is seen that the measured temperatures were about 7% lower than predicted. This is a fact presumably related to the underprediction of the heat transfer rate in the solution air-cooler.

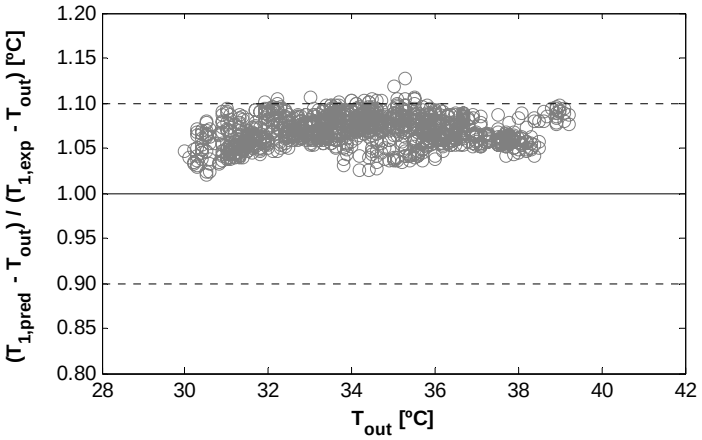

Figure 8.9 Comparison of experimental and predicted absorber parameters: T_1

In Figure 8.10, the measured cooling power values of the prototype are compared with the rates that could be reached if considering only the absorption process. As seen, in most of the cases the agreement was quite good, being most of the points within the ±20% error band. A general tendency to overprediction was found, however. As above pointed out, the fact of obtaining higher rates in simulation than in experiments seems to be due to thermal losses taking place in the evaporator and other components of the prototype. These losses cause that a lower refrigerant rate is evaporated on the tubes of the evaporator and, as a result, a lower cooling power is obtained. Moreover, one should note that the refrigerant production in the prototype was lower than expected, as shown in Chapter 6 and Chapter 7. Though a clear pattern was not found in plotting the comparison results versus the outdoor temperature, the model tends to better approximate the experimental and numerical values as the outdoor temperature rises. Actually, the best results were found for ambient temperatures around 35°C, which is the design point of the prototype.

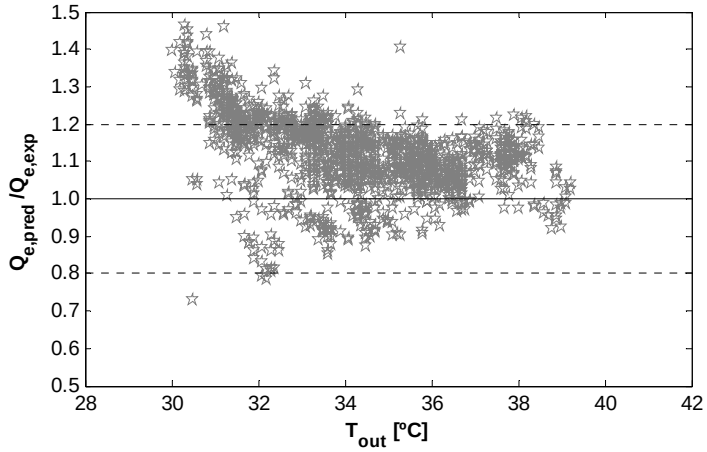

Figure 8.10 Comparison of experimental and predicted absorber parameters: *Qe*

8.5 Conclusions

In this chapter, the numerical results obtained from the absorber modelization were compared with experimental data and a very good agreement was found. Actually, for all the characteristic temperatures in the absorber, the mismatch between measurements and predictions was under 10%, being around 4-5% in most cases. However, when considering the heat transfer rate in the solution-air cooler, the discrepancies increased up to ±20%. By and a large, this seemed to be caused by underestimating the fluctuations in the air flow through the heat exchangers.

On account of the good agreement observed between experimental results and predictions, it can be stated that the model is valid to perform numerical simulations of air-cooled absorbers with LiBr/H_2O flat-fan sheets. Nevertheless, improvements in the mathematical model are still needed to achieve better predictions of the absorber performance.

On the other hand, the comparison carried out in this chapter yielded that the real cooling power delivered in the evaporator of the prototype is around 20% lower than the maximum cooling capacity of the absorber. The main reason is that the prototype produced less water vapor than could be absorbed by the solution sheets in the absorber. Thermal losses in the prototype's evaporator appeared as another possible cause for the lower cooling power. As a result, further investigation on reducing thermal losses and enhancing the refrigerant production of the prototype is recommended to make the most of the absorber capacity.

Chapter 9

Conclusions and recommendations

9.1 Introduction

This chapter summarizes the main conclusions derived from the work performed in this thesis. The achievement of the initially stated objectives will be as well justified. Besides, aspects meriting further investigation will be detailed.

9.2 Achievement of the initial goals

As stated in Chapter 1, the main goal of this thesis was to characterize and test a new air-cooled LiBr/H_2O absorption prototype which can perform as a single-effect unit or as a double-effect one. In this sense, a detailed description of the prototype and its testing facilities was given in Chapter 3. Besides, a numerical simulation was carried out in Chapter 4 with the purpose of complementing the characterization of the prototype.

The experimental procedure to evaluate the single-effect operation mode of the prototype was presented in Chapter 6. Likewise, this chapter showed and discussed the experimental results obtained by powering the single-effect stage with a solar energy facility existing in the laboratory of the *Energy Saving and Emissions Reduction in Buildings* research group (Madrid). With regards to the double-effect tests, Chapter 7 presented the experimental procedure and discussed the obtained results.

On the other hand, characterization, modelization and optimization of the flat-fan sheets adiabatic absorber installed in the prototype were as well objectives to be met. In this regard, Chapter 5 included an in-depth description of the air-cooled absorber and presented a numerical model to simulate its performance. The proposed model was validated with experimental results in Chapter 8.

Finally, the positive results derived from this work are regarded as an important contribution to development of air-cooled $LiBr/H_2O$ absorption technology. What is more, the presented prototype may be considered as a promising solution to improve the performance of small scale solar cooling systems, which was as well one of the initial goals of the present study. Based on this prototype, it is thought that a machine could be developed and commercialized to directly compete with electrical air conditioning systems.

9.3 Main conclusions of the study

The major conclusions drawn from this thesis are the following.

From a state-of-the-art review, it was concluded that air-cooled single-effect absorption technology based on $LiBr/H_2O$ is one of most suitable options to efficiently supply air conditioning to residential and commercial buildings. However, it is not possible to find any commercial chiller with such characteristics in the current market. The likely crystallization of $LiBr/H_2O$ solution is regarded as the main obstacle to develop this kind of machines.

On the other hand, it was seen that solar systems are not generally able to meet 100% of seasonal cooling demand mainly because of the intermittency of solar energy and the elevated installation costs. Therefore, it was noticed that an innovative solution is needed to efficiently and economically cover the whole cooling demand of a building.

An air-cooled single–double-effect $LiBr/H_2O$ prototype was proposed as an alternative system to solve the above problems. This absorption machine was though to be powered by solar heat in its single-effect mode or by firing a fuel in its double-effect stage. The fact of being an air-cooled unit makes it a suitable option for hot and arid climates, where water is a scant source. Besides, the compact design of the machine permits the installation in buildings where available space is reduced.

Another important feature of the presented prototype is the incorporation of a direct air–cooled adiabatic absorber with flat-fan sheets distribution. In this sense, the present thesis includes a detailed description of that absorber and develops a mathematical model to perform simulations of its behavior. This model, which has been experimentally validated, was utilized to carry out an optimization of the absorber design. In this regard, the absorption capacity of the absorber was analyzed taking into account the energy consumption of its auxiliary equipment (solution pump and fan). It was concluded that a configuration consisting of 18 sprayers in the absorption chamber and an air flow rate of 1.6-2.2 kg/s through the absorber air-cooler is within the optimum range to provide a cooling capacity of 4.5 kW in single-effect operation mode and of 7 kW in double-effect. Besides, from the analysis of the absorber design, it was drawn that the prototype can work at high outdoor temperatures without risk of crystallization.

A solar facility with evacuated flat-plate collectors was used to test the single-effect operation mode of the absorption prototype. Fourteen tests were performed under a wide range of working conditions during the summer of 2010. The most relevant findings from that experimental campaign are the following:

- Values around 0.6 were obtained for the daily thermal COP, whereas the electrical COP mostly ranged between 3.0 and 3.5. The cooling capacity varied from 2 kW to 3.8 kW, being normally about 3-3.5 kW. The chilled water temperature ranged from 12.8°C to 19°C, although it was mostly between 14°C and 16°C. Condensation and absorption temperatures were always lower than 50°C and 46°C, respectively, even with outdoor temperatures around 40°C. Driven water temperatures ranged between 85°C and 110°C.
- The effectiveness of the solution heat exchanger was very high, around 0.88. This fact played a key role in the performance of the prototype, especially by contributing to achieve low absorption temperatures.
- No signs of solution crystallization were noticed after about one hundred hours of operation, which proves the feasibility of direct air-cooled single-effect $LiBr/H_2O$ absorption chillers for solar air conditioning applications.
- Even though the system was able to meet 100% of the daily cooling demand in a few days, 35% of the seasonal cooling demand was not covered. This

evidenced the need of a complementary system to supply the missing cooling energy.

- When comparing experimental and predicted results at nominal conditions, it was found that: cooling power was some 20% lower than expected; thermal COP was about 10% lower; effectiveness of the solution heat exchanger was around 10% higher; evaporation, absorption and condensation temperatures matched really well with predictions; electrical consumption of ancillary equipment was 30% underpredicted.
- Improvements in the regulation system were found to be needed to achieve a better performance and higher cooling capacities. Besides, reducing the electrical consumption of the ancillary equipment is also recommended.

The experimental campaign to test the prototype performing as an indirectly fired double-effect machine consisted of three tests carried out in August and October 2010. A facility supplying thermal oil at the required temperatures was utilized to feed the high-pressure generator. Besides, in the test performed in October, a climatic chamber was used to create summer conditions around the prototype. The most significant findings from this experimental campaign are the following:

- The prototype was able to work with thermal COP around 1.0, being the electrical COP about 4.0. The cooling power reached values of 4.5 kW. The prototype worked with thermal oil temperatures between 150°C and 180°C. Absorption and condensation temperatures were mostly about 10-11°C and 12-14°C higher than ambient temperatures, respectively.
- The effectiveness of the high- and low-solution heat exchangers resulted to be 0.90 and 0.57, respectively.
- The solution was observed to work reasonably far from the critical conditions. In fact, after about 22 hours of operation, no crystallization signs were detected.
- Comparison with simulation results yielded that: thermal COP was some 15% overpredicted; cooling power was 35% lower than expected; heat power transferred in the high-pressure generator was about 25% lower than predicted; effectiveness of the high-solution heat exchanger was 12% greater than expected; in turn, effectiveness of the low-solution heat ex-

changer was about 30% lower than expected; absorption temperature was 6% higher than predicted; evaporation and condensation temperatures were predicted with error less than 5%; electricity consumption was 25% higher than expected.

- The following actuations were noticed to be needed to enhance the performance of the prototype: improving the regulation system, increasing the fan capacity, enhancing the effectiveness of the low-solution heat exchanger; increasing the heat transfer capacity of the high-generator; reducing the electrical consumption of the ancillary equipment.

As a final conclusion, it can be stated that the proposed system represents a feasible alternative to overcome some of the major difficulties related to solar-air conditioning. Although the presented prototype still requires to be optimized, the promising results obtained lead to an optimistic thought about the replacement of conventional air conditioners by more environmentally friendly systems.

9.4 Recommendations for further research

From the present thesis, a series of future works arises. Apart from the aforementioned modifications to enhance the performance of the prototype and reduce its electrical consumption, it is recommended to carry out the following investigations:

- The simultaneous operation of both the single- and the double-effect stages must be theoretically and experimentally studied.
- A few tests must be performed at extreme outdoor temperatures; that is, at ambient temperatures from 40°C to 50°C.
- Development of an air-cooled prototype combining single- and triple-effect absorption cycles is regarded as the next step in development of efficient and environmentally friendly systems for the replacement of vapor compression systems.

References

Acosta-Iborra, A., García, N. & Santana, D., 2009. Modelling non-isothermal absorption of vapour into expanding liquid sheets. *International Journal of Heat and Mass Transfer*, 52:3042-54.

Agyenim, F., Knight, I. & Rhodes, M., 2010. Design and experimental testing of the performance of an outdoor LiBr/H_2O solar thermal absorption cooling system with a cold store. *Solar Energy*, 84:735-44.

Arora, A. & Kaushik, S.C., 2009. Theoretical analysis of LiBr/H_2O absorption refrigeration systems. *International Journal of Energy Research*, 33:1321-40.

Arun, M.B., Maiya, M.P. & Murthy, S.S., 2000. Equilibrium low pressure generator temperatures for double effect series flow absorption refrigeration systems. *Applied Thermal Engineering*, 20:227-42.

Arun, M.B., Maiya, M.P. & Murthy, S.S., 2001. Performance comparison of double-effect parallel-flow and series-flow water-lithium bromide absorption systems. *Applied Thermal Engineering*, 21:1273-79.

Arzoz, D., Rodriguez, P. & Izquierdo, M., 2005. Experimental study on the adiabatic absorption of water vapor into LiBr-H_2O solutions. *Applied Thermal Engineering*, 25:797-811.

Asdrubali, F., Baldinelli, G. & Presciutti, A., 2008. Solar cooling with small-size absorption chillers: different solutions for summer air conditioning. *From web source: http://www.crbnet.it/File/Pubblicazioni/pdf/1439.pdf*.

Asdrubali, F. & Grignaffini, S., 2005. Experimental evaluation of the performances of a H_2O-LiBr absorption refrigerator under different service conditions. *International Journal of Refrigeration*, 25:489-97.

ASHRAE, 2009. *ASHRAE Handbook - Fundamentals (SI)*.

Balaras, C.A. et al., 2007. Solar air conditioning in Europe-an overview. *Renewable and Sustainable Energy Reviews*, 11:299-314.

Bales, C., Bolin, G., Nordlander, S. & Settenwall, F., 2005. Solar driven chemical heat pump with integral storage - the thermo-chemical accumulator. In *Proceedings of the 1st International Conference Solar Air-Conditioning*. Bad Staffelstein, Germany. pp.63-67.

Banasiak, K. & Koziol, J., 2009. Mathematical modelling of a LiBr-H_2O absorption chiller including two-dimensional distributions of temperature and concentration fields for heat and mass exchangers. *International Journal of Thermal Sciences*, 48:1755-64.

Bourouis, M., Vallès, M., Medrano, M. & Coronas, A., 2005. Absorption of water vapour in the falling film of water-(LiBr+LiI+$LiNO_3$+LiCl) in a vertical tube at air-cooling thermal conditions. *International Journal of Thermal Sciences*, 44:491-98.

BSRIA, 2005. *European Market for air conditioning*.

Carrier, 2011. *www.carrier.es*.

Castro, J., Oliva, A., Perez-Segarra, C.D. & Oliet, C., 2008. Modelling of the heat exchangers of a small capacity, hot water driven, air-cooled H_2O-LiBr absorption cooling machine. *International Journal of Refrigeration*, 31:75-86.

Christians, M., 2010. *Heat transfer and visualization of falling film evaporation on a tube bundle*. École Polytechnique Fédéral de Lausanne (EPFL). PhD thesis.

de Vega, M., Almendros-Ibañez, J.A. & Ruiz, G., 2006. Performance of a LiBr-water absorption chiller operating with plate heat exchangers. *Energy Conversion and Management*, 47:3393-407.

ECOHEATCOOL, 2007. *The European Cold Market*.

ESTIF, 2006. *Key Issues for Renewable Heat in Europe - Solar Assisted Cooling*.

Fan, Y., Luo, L. & Souyri, B., 2007. Review of solar sorption refrigeration technologies: Development and applications. *Renewable and Sustainable Energy Reviews*, 11:1758-75.

Fong, K.F. et al., 2010. Comparative study of different solar cooling systems for buildings in subtropical city. *Solar Energy*, 84:227-44.

Gebreslassie, B.H., Medrano, M. & Boer, D., 2010. Exergy analysis of multi-effect-LiBr absorption systems: From half to triple effect. *Renewable Energy*, 35:1773-82.

Gilchrist, K., Lorton, R. & Green, R.J., 2002. Process intensification applied to an aqueous LiBr rotating absorption chiller with dry heat rejection. *Applied Thermal Engineering*, 22:847-54.

Gluesenkamp, K., Radermacher, R. & Hwang, Y., 2011. Trends in absorption machines. In *Proceedings of the International Sorption Heat Pump Conference (ISHPC11)*. Padua, Italy. pp.13-22.

Gnielinski, V., 1976. Equations for heat and mass transfer in turbulent pipe and channel flow. *International Chemical Engineering*, 16:359-68.

Gomri, R., 2010. Investigation of the potential of application of single effect and multiple effect absorption cooling systems. *Energy Conversion and Management*, 51:1629-36.

Gomri, R. & Hakimi, R., 2008. Second law analysis of double effect vapour absorption cooler system. *Energy Conversion and Management*, 49:3343-48.

González-Gil, A., Izquierdo, M., Marcos, J.D. & Palacios, E., 2011. Experimental evaluation of a direct air-cooled lithium bromide–water absorption prototype for solar air conditioning. *Applied Thermal Engineering*, 31:3358-68.

Gutiérrez-Urueta, G. et al., 2011. Experimental performances of a Libr-water absorption facility equipped with adiabatic absorber. *International Journal of Refrigeration*, In Press doi: 10.1016/j.ijrefrig.2011.07.014.

Häberle, A. et al., 2007. A linear concentrating Fresnel collector driving a NH_3-H_2O absorption chiller. In *Proceedings of the 2nd International Conference Solar Air-Conditioning*. Tarragona, Spain. pp.662-67.

Henning, H.M., 2007. Solar assisted air conditioning of buildings-an overview. *Applied Thermal Engineering*, 27:1734-49.

Herold, K.E., Radermacher, R. & Klein, S.A., 1996. *Absorption Chillers and Heat Pumps*. CRC Press.

IEA, 2007. *Renewables for Heating and Cooling*.

IIR, 2003. *International Institute of Refrigeration newsletter, No 13*.

Incropera, F.K. & De Witt, D.P., 1999. *Fundamentos de Transferencia de Calor*. 4th ed. México: PRENTICE HALL.

Izquierdo, M., 1996. *Apuntes de Tecnología frigorífica de absorción*. Universidad Carlos III de Madrid.

Izquierdo, M., de Vega, M., Lecuona, A. & Rodríguez, P., 2002. Compressors driven by thermal solar energy: entropy generated, exergy destroyed and exergetic efficiency. *Solar Energy*, 72:363-75.

Izquierdo, M., González-Gil, A., Marcos, J.D. & Palacios, E., 2011b. Direct air-cooled single effect LiBr/H_2O absorption prototype using a flat-fan sheets adiabatic absorber: experimental results. In *Proceedings of the International Sorption Heat Pump Conference (ISHPC11)*. Padua, Italy. pp.85-94.

Izquierdo, M., Lizarte, R., Marcos, J.D. & Gutiérrez, G., 2008. Air conditioning using an air-cooled single effect lithium bromide absorption chiller: Results of a trial conducted in Madrid in August 2005. *Applied Thermal Engineering*, 28:1074-81.

Izquierdo, M., Marcos, J.D., Palacios, E. & González-Gil, A., 2011c. Experimental evaluation of a low power direct air-cooled double-effect LiBr-H_2O absorption prototype. *Energy*, in review process.

Izquierdo, M., Martín, E. & Palacios, E., 2010. Absorber and absorber-evaporator assembly for absorption machines and lithium bromide-water absorption machines that integrate said absorber and absorber-evaporator assembly. *Patent PCT WO2010/000571A2 and European Patent EP2133636A1 (extended to USA, Japan, China, Canada, Brazil, Argentina, Venezuela)*.

Izquierdo, M., Moreno-Rodríguez, A., González-Gil, A. & García-Hernando, N., 2011a. Air conditioning in the region of Madrid, Spain: An approach to electricity consumption, economics and CO_2 emissions. *Energy*, 36:1630-36.

Izquierdo, M., Venegas, M., García, N. & Palacios, E., 2005. Exergetic analysis of a double stage LiBr-H_2O thermal compressor cooled by air/water and driven by low grade heat. *Energy Conversion and Management* , 46:1029-42.

Izquierdo, M., Venegas, M., Rodríguez, P. & Lecuona, A., 2004. Crystallization as a limit to develop solar air-cooled LiBr-H_2O absorption systems using low-grade heat. *Solar Energy Materials & Solar Cells*, 81:205-16.

Jakob, U. & Pink, W., 2007. Development and investigation of an ammonia/water absorption chiller - chillii® PSC - for a solar cooling system. In *Proceedings of the 2nd International Conference Solar Air-Conditioning*. Tarragona, Spain. pp.440-45.

Jian, S., Lin, F. & Shigang, Z., 2010. Performance calculation of single effect absorption heat pump using LiBr + $LiNO_3$ + H_2O as working fluid,. *Applied Thermal Engineering*, 30:2680-84.

Joudi, K.A. & Lafta, A.H., 2001. Simulation of a simple absorption refrigeration system. *Energy Conversion & Management*, 42:1575-605.

Kaita, Y., 2002. Simulation results of triple-effect absorption cycles. *International Journal of Refrigeration*, 25:999-1007.

Kays, W.M. & London, A.L., 1984. *Compact Heat Exchangers*. 3rd ed. New York: McGraw-Hill.

Kim, D.S., 2007. *Solar absorption cooling*. Technische Universiteit Delft. PhD thesis.

Kim, K.J., Berman, N.S., Chau, D.S.C. & Wood, B.D., 1995. Absorption of water vapour into falling films of aqueous lithium bromide. *International Journal of Refrigeration*, 18:486-94.

Kim, D.S. & Infante-Ferreira, C.A., 2008a. Analytic modelling of steady state single-effect absorption cycles. *International Journal of Refrigeration*, 31:1012-20.

Kim, D.S. & Infante-Ferreira, C.A., 2008b. Solar refrigeration options-a state-of-the-art review. *International Journal of Refrigeration*, 31:3-15.

Kim, D.S. & Infante-Ferreira, C.A., 2009. Air-cooled LiBr-water absorption chillers for solar air conditioning in extremely hot weathers. *Energy Conversion & Management*, 50:1018-25.

Kim, J.S., Park, Y. & Lee, H., 1999. Performance evaluation of absorption chiller using LiBr+$H_2N(CH_2)_2OH$+H_2O, LiBr+$HO(CH_2)_3OH$+H_2O, and LiBr+$(HOCH_2CH_2)_2NH$+H_2O as working fluids. *Applied Thermal Engineering*, 19:217-25.

Kim, J.S., Ziegler, F. & Lee, H., 2002. Simulation of the compressor-assisted triple-effect H_2O/Libr absorption cooling cycles. *Applied Thermal Engineering*, 22:295-308.

Kline, S.J. & McClintock, F.A., 1953. Describing uncertainties in single-sample experiments. *Mechanical Engineering*, 75:3-8.

Kohlenbach, P. & Ziegler, F., 2008. A dynamic simulation model for transient absorption chiller performance. Part I: The model. *International Journal of Refrigeration*, 31:217-25.

Lee, H. et al., 2000. Thermodynamic design data and performance evaluation of the water + lithium bromide + lithium iodide + lithium nitrate + lithium chloride system for absorption chiller. *Applied Thermal Engineering*, 20:707-20.

Liao, X. & Radermacher, R., 2007. Absorption chiller crystallization control strategies for integrated cooling heating and power systems. *International Journal of Refrigeration*, 30:904-11.

Lizarte, R., 2010. *Evaluación experimental de máquinas de absorción de simple efecto de LiBr-H_2O de pequeña potencia condensadas por aire: sistema re-cooling frente a sistema directo*. Universidad Carlos III de Madrid. PhD thesis.

Marcos, J.D., 2008. *Prototipo de máquina de frigorífica de absorción de LiBr/H_2O de doble efecto condensada por aire*. Universidad Carlos III de Madrid. PhD thesis.

Marcos, J.D. et al., 2009. Experimental boiling heat transfer coefficients in the high temperature generator of a double effect absorption machine for the lithium bromide/water mixture. *International Journal of Refrigeration*, 32:627-37.

Marcos, J.D., Izquierdo, M. & Palacios, E., 2011a. New method for COP optimization in water- and air-cooled single and double effect LiBr/water absorption machines. *International Journal of Refrigeration*, 34:1348-59.

Marcos, J.D., Izquierdo, M. & Parra, D., 2011b. Solar space heating and cooling for Spanish housing: Potential energy savings and emissions reduction. *Solar Energy*, In Press doi:10.1016/j.solener.2011.08.006.

Medrano, M., Bourouis, M. & Coronas, A., 2002. Absorption of water vapour in the falling film of water-lithium bromide inside a vertical tube at air-cooling thermal conditions. *International Journal of Thermal Sciences*, 41:891-98.

Mendes, J.F., 2007. Solar collectors for solar cooling - Market status and new developments. In *IEA SHC Workshop*. Aix-les-Bains. Oral communication.

MICYT, 2007. *Reglamento de Instalaciones Térmicas en Edificios (RITE)*. Ministerio de Industria, Comercio y Turismo.

MICYT, 2010. *La Energía en España 2009*. Ministerio de Industria, Comercio y Turismo.

Monné, C., Alonso, S., Palacín, F. & Serra, L., 2011. Monitoring and simulation of an existing solar powered absorption cooling system in Zaragoza (Spain). *Applied Thermal Engineering*, 31:28-35.

Mori, A. et al., 1984. Absorption type refrigeration system. *United States Patent 4,439,999*.

Palacios, E., Izquierdo, M., Lizarte, R. & Marcos, J.D., 2009a. Lithium bromide absorption machines: Pressure drop and mass transfer in solutions conical sheets. *Energy Conversion and Management*, 50:1802-09.

Palacios, E., Izquierdo, M., Marcos, J.D. & Lizarte, R., 2009b. Evaluation of mass absorption in LiBr flat-fan sheets. *Applied Energy*, 86:2574-82.

Pátek, J. & Klomfar, J., 2006. A computationally effective formulation of the thermodynamic properties of LiBr-H_2O solutions from 273 to 500 K over full composition range. *International Journal of Refrigeration*, 29:566-78.

Petukhov, B.S., 1970. Heat transfer and friction in turbulent pipe with variable physical properties. *Advances in Heat Transfer*, 6:503-64.

Poniewski, M.E. & Thome, J.R., 2008. *Nucleate Boiling on Micro-Structured Surfaces*. Warsaw (Poland) and Lausanne (Switzerland): Heat Transfer Research, Inc., (HTRI).

Riepl, M., Gurtner, R. & Schweigler, C., 2011. Solar assisted cooling with a multi-stage absorption chiller. In *Proceedings of the International Sorption Heat Pump Conference (ISHPC11)*. Padua, Italy. pp.923-30.

Ryan, W.A., 1993. Water absorption in an adiabatic spray of aqueous lithium bromide solution. In *Proceedings of the International Absorption Heat Pump Conference*. ASME. pp.155-62.

SACE, 2003. *Solar Air conditioning in Europe: Final Report*. EC project NNE5/2001/25.

Schneider, M.C. et al., 2011. Ionic Liquids: new high-performance working fluids for absorption chillers and heat pumps. In *Proceedings of the International Sorption Heat Pump Conference (ISHPC11)*. Padua, Italy. pp.95-106.

Sumathy, K., Huang, Z.C. & Li, Z.F., 2002. Solar absorption cooling with low grade heat source-a strategy of development in South China. *Solar Energy*, 42:155-65.

Syed, A. et al., 2005. A novel experimental investigation of a solar cooling system in Madrid. *International Journal of Refrigeration*, 28:859-71.

Thévenot, R., 1978. *Essai pour une histoire du froid artificiel dans le monde*. Paris: IIF-IIR.

Thome, J.R., 2004. *Wolverine Engineering Databook III*. Available online at http://www.wlv.com/products/databook/db3/DataBookIII.pdf.

Tongu, S., Makino, Y., Ohnishi, K. & Nakatsugawa, S., 1993. Practical operating of small-sized air-cooled double-effect absorption chiller-heater by using lithium bromide and aqueous. *International Absorption Heat Pump Conference, ASME*, 31.

Wang, K., Abdelaziz, O., Kisari, P. & Vineyard, E.A., 2011. State-of-the-art review on crystallization control technologies for water/LiBr absorption heat pumps. *International Journal of Refrigeration*:1-13.

Wang, L., Chen, G.M., Wang, Q. & Zhong, M., 2007. Thermodynamic performance analysis of gas-fired air-cooled adiabatic absorption refrigeration systems. *Applied Thermal Engineering*, 27:1642-52.

Wang, R.Z. et al., 2009. Solar sorption cooling systems for residential applications: Options and guidelines. *International Journal of Refrigeration*, 32:638-60.

Wang, L., You, S., Zhang, H. & Li, X., 2010. Simulation of gas-fired triple-effect LiBr/water absorption cooling system with exhaust heat recovery generator. *Transactions of Tiunjin University*, 16(3), pp.187-93.

Wang, J. & Zheng, D., 2009. Performance of one and a half-effect absorption cooling cycle of H_2O/LiBr system. *Energy Conversion and Management*, 50:3087-95.

Warnakulasuriya, F.S.K. & Worekx, M.M., 2008. Drop formation of swirl-jet nozzles with high viscous solution in vacuum-new absorbent in spray absorption refrigeration. *International Journal of Heat and Mass Transfer*, 51:3362-68.

Xie, G., Sheng, G., Bansal, P.K. & Li, G., 2008. Absorber performance of a water/lithium-bromide absorption chiller. *Applied Thermal Engineering*, 28:1557-62.

Yari, M., Zarin, A. & Mahmoudi, S.M.S., 2011. Energy and exergy analyses of GAX and GAX hybrid absorption refrigeration cycles. *Renewable Energy*, 36:2011-20.

Yazaki Corporation, 2000. Absorbing Solution for Absorption Refrigerating Machine and Absorption Refrigerating Machine. *Japanese Patent 2000-319646*.

Ziegler, F., 2002. State of the art in sorption heat pumping and cooling technologies. *International Journal of Refrigeration*, 25:450-59.

Appendix A

Experimental uncertainty analysis

A.1. Introduction

In this Appendix, the method utilized to ascertain the uncertainty of the main experimental results exposed in the present study will be described.

A.2. Uncertainty and experimental errors

According to (Kline & McClintock, 1953), the term *uncertainty* refers to a possible value that an error may have. Both *uncertainty* and *uncertainty interval* refer to the interval around a measured value where the true value is expected to lie.

The total uncertainty associated with a measurement is basically made up of two components: the *bias error (B)* and *precision error (P)*. The bias error, also called systematic error or simply bias, is due to faults in the measuring instruments or in the techniques used in the experiment. This is therefore a fixed value.

The precision error, also known as random error or repeatability error, is associated with unpredictable variations in the experimental conditions. It can be as well due to a deficiency in defining the quantity being measured. Owing to their random nature, precision errors generally follow a specific statistical distribution.

If an experiment has low bias error, it is said to be *accurate.* In turn, if an experiment has low precision error, it is said to be *precise*.

If considering the measurement of a variable X_1, the associated uncertainty is represented as δX_1. Its value is calculated as the Euclidean norm of its two components, the bias (B_1) and the precision error (P_1); that is

$$\delta X_1 = \sqrt{(B_1)^2 + (P_1)^2} \tag{A.1}$$

There are two common ways to state the uncertainty of a result: by directly expressing the uncertainty value associated with the measurement $X_1 \pm \delta X_1$; or by given it in terms of percentage $X_1 \pm U_1(\%)$, with $U_1(\%) = \delta X_1 / X_1$.

Some researchers deal with bias and precision errors separately whereas others deal with the uncertainty directly. In the present study, only the uncertainty will be considered.

A.3 Propagation of uncertainty

The method of assessing the uncertainty in a result which depends upon several variables, each with its own uncertainty, is known as *propagation of uncertainty*.

Let us take a result Y which is a function of n variables, X_1 to X_n, each with uncertainty δX_i

$$Y = f(X_1, X_2, \dots, X_n) \tag{A.2}$$

Then, the effect of the uncertainty of a single variable X_i on quantity Y is calculated as the partial derivative of Y with respect to that single variable, multiplied by that variable's uncertainty δX_i. The maximum uncertainty is given by the addition of the uncertainties of Y in terms of its variables. However, since it is very unlikely to achieve that value, it is preferable to use the Euclidean norm of the individual uncertainties; that is

$$\delta Y = \left[\sum_{i=1}^{n} \left(\delta X_i \frac{\partial Y}{\partial X_i} \right)^2 \right]^{\frac{1}{2}} \tag{A.3}$$

This expression is valid when the uncertainties of the different variables are small compared to the values of the quantities and on the requirement that the uncertainties are independent one of another.

As above mentioned, it is common to normalize δY with respect to the full value of Y, with percentage units. However, this is not valid for temperatures, due to the fact that different temperature scales will have different percentages. Besides, special cases as 0°C make it impossible to express the uncertainty as a percentage value.

Appendix B

Measurement instrumentation

B.1 Introduction

In this Appendix, technical details on the measurement equipment utilized in the present study will be shown.

B.2 Meteorological variables

The following automatic weather station was utilized to measure the meteorological conditions during experiments: *METEODATA-3008CM*, Figure B.1. It consists of a remote automatic data acquisition and transmission unit, teleprogrammable and compact mounted in a heavy duty metallic housing. It includes 8 analog input channels, 2 micro-relay digital inputs, 2 micro-relay digital outputs, 4 digital counters for pluviometers, anemometers and other similar sensors with impulse/frequency output, and 4 programmable serial ports RS232/422/485.

The following detectors were connected to the weather station:

- Black and white pyranometer - model 8-48, whose main specifications are:
  - sensitivity: 10 $\mu V/Wm^{-2}$.
  - impedance: 350 Ω.

  - temperature dependency: ±1.5% constancy from -20°C to 40°C.
  - linearity: ±1% for 0 to 1400 Wm^{-2}.

- Anemometer model 0510 with output of 4-20 mA. It permits to measure:
  - velocities from 0 to 100 m/s ; the accuracy is ± 3 m/s for velocities between 1 and 60 m/s or ± 1 m/s for velocities of 60-100 m/s.
  - direction from 0° to 360° with accuracy of ±3°.

- Combined sensor for temperature and relative humidity:
  - temperature range from -30°C to 70°C; accuracy 0.1°C.
  - humidity range from 0 to 100%; accuracy ±3% for 0-90% and ±3% for 90-100%.

Figure B.1 Weather data acquisition system: *Meteodata-3008CM*

B.3 Process variables

B.3.1 Flow measurements

In order to register liquid flow rates, the following ultrasonic flow meter was utilized: *Flexim-Fluxus AMD 6725,* Figure B.2. One of its major advantages is that transducers are not in direct contact with the fluid, therefore no pressure loss occurs and there is no risk of leakages. Besides, corrosion is avoided.

The main characteristics of the selected flow meter are:

  - Measuring principle: transit time difference correlation principle.
  - Flow velocity range: 0.01 to 25 m/s.

- Resolution: 0.025 cm/s.
- Repeatability: 0.15% of reading ±0.01 m/s.
- Accuracy: for fully developed, rotationally symmetrical flow profile.
    - volume flow: ±1% to 3% of reading depending on application.
    - path velocity: ±0.5% of reading.
- Measurable fluids: all acoustically conductive with < 10% gaseous or solid content in volume.
- Data capacity: 100 000 measured values.
- Communication RS232.
- Inputs: two channels for fluid flow and other two for temperature (with Pt-100 four wire circuit).

Figure B.2 Ultrasonic flow meter *Flexim-Fluxus AMD 6725*

Two kinds of clap-on transducers were used to measure the fluid flows:

- *Type Q3N*: diameter range from 25 to 400 mm; operating temperature from -30°C to 130°C, for short periods up to 300°C.
- *Type Q3E* : diameter range from 25 to 400 mm; operating temperature from -30°C to 200°C, for short periods up to 300°C.

B.3.2 Temperature measurements

Pt-100 thermoresistances were used as temperature detectors with the following specifications:

- Temperature range: from -200°C to 200°C.

- Accuracy: 0.1°C.
- Sense current: 0.2 mA.
- Resolution: 0.05°C.
- They can be used in any 2, 3 or 4-wire applications.

A dry block calibrator *ISOTECH Venus Plus 2140* was utilized to calibrate all the RTDs, Figure B.3.

Figure B.3 Calibrator *ISOTECH Venus Plus 2140* for temperature detectors

B.3.3 Vacuum meter

In the absorber-evaporator assembly, the pressure is measured by the following vacuum meter: *Membranovac DM12*, Figure B.4. Its main specifications are:

- Display range: -750 to +15000 mbar.
- Interface: RS232-C.
- Accuracy: 0.2% of transducer full scale.

The pressure transducer connected to that device is a *DI 200* type from *Leybold*. The absolute pressure range is from 0.1 to 200 mbar.

The data measured by this digital vacuum meter are directly transferred to a computer. However, an analogical vacuum meter was additionally installed in the absorber-evaporator assembly. The reason of this double measurement system is the great importance of keeping the vacuum controlled in every moment.

Figure B.4 Vacuum meter *Membranovac DM12*

B.3.4 Data acquisition system

In order to display and save all the measurements from Pt-100 RTDs, a *Yokogawa DC100* acquisition unit was used, Figure B.5. It is equipped with four 10-channels measurement cards, which means that 40 input channels are available in each unit. Yokogawa's original software *DARWING-DAQ32* was used to process all the measured data.

Figure B.5 Yokogawa DC100 acquisition system